

AD-A099 795

NAVAL SURFACE WEAPONS CENTER DAHLGREN VA F/G 1/1  
AERODYNAMICS OF TACTICAL WEAPONS TO MACH NUMBER 8 AND ANGLE OF --ETC(U)  
OCT 80 L DEVAN  
NSWC/TR-80-346-PT-1 NL

**F/G 1/1**

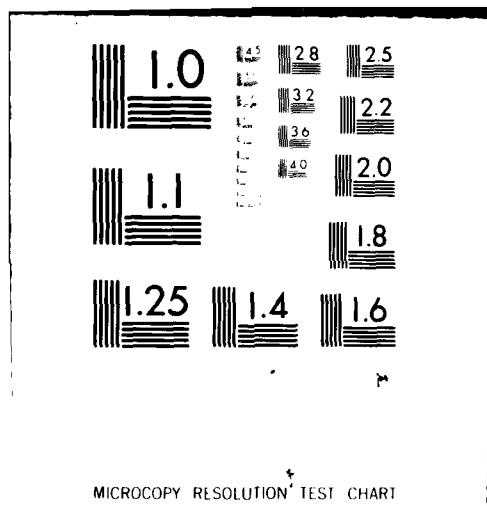
UNCLASSIFIED

NSWC/TR-80-346-PT-1

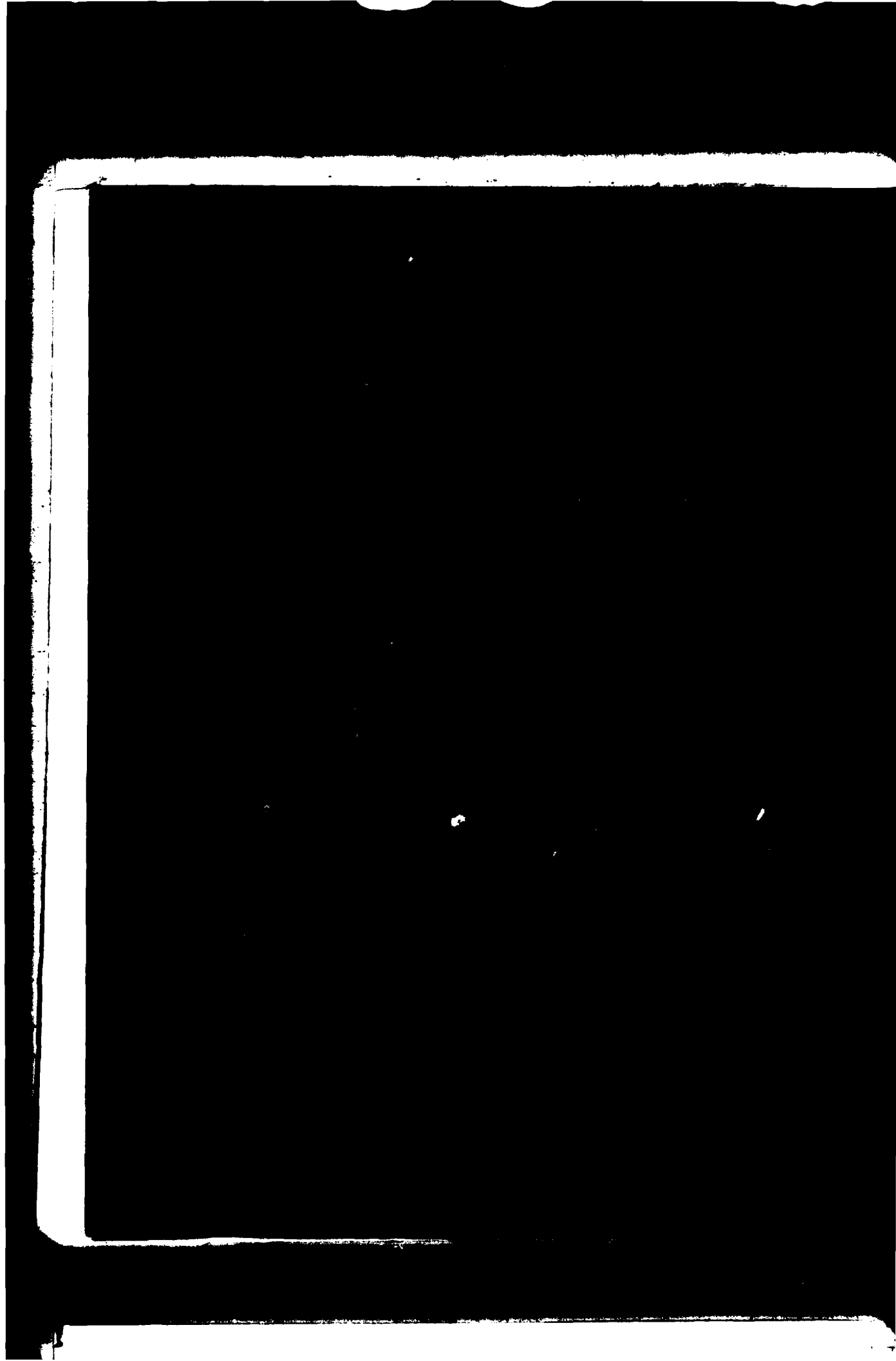
NL

1.  $\frac{1}{2} \times \frac{1}{2} = \frac{1}{4}$

END  
DATE  
FILMED  
6-8-81  
DTIC



AD A099795



UNCLASSIFIED

(12) 93

SECURITY CLASSIFICATION OF THIS PAGE (When Data Entered)

REPORT DOCUMENTATION PAGE		READ INSTRUCTIONS BEFORE COMPLETING FORM
1. REPORT NUMBER (14) NSWC/TR-80-346-PT-1	2. GOVT ACCESSION NO. AD A099795	3. RECIPIENT'S CATALOG NUMBER
4. TITLE (and Subtitle) (6) AERODYNAMICS OF TACTICAL WEAPONS TO MACH NUMBER 8 AND ANGLE OF ATTACK 180°. PART I, THEORY AND APPLICATION	5. TYPE OF REPORT & PERIOD COVERED (9) Final rept.	6. PERFORMING ORG. REPORT NUMBER
7. AUTHOR(s) (10) Leroy/Devan	8. CONTRACT OR GRANT NUMBER(s)	
9. PERFORMING ORGANIZATION NAME AND ADDRESS Naval Surface Weapons Center (K21) Dahlgren, VA 22448	10. PROGRAM ELEMENT, PROJECT, TASK AREA & WORK UNIT NUMBERS (17) 61153N: R02302; SR02302001	
11. CONTROLLING OFFICE NAME AND ADDRESS Naval Sea Systems Command Washington, DC 20362	12. REPORT DATE (11) October 1980	13. NUMBER OF PAGES 94
14. MONITORING AGENCY NAME & ADDRESS (if different from Controlling Office)	15. SECURITY CLASS. (of this report) UNCLASSIFIED	15a. DECLASSIFICATION/DOWNGRADING SCHEDULE
16. DISTRIBUTION STATEMENT (of this Report) Approved for public release; distribution unlimited (16) SR02302, 1L162303A214		
17. DISTRIBUTION STATEMENT (of the abstract entered in Block 20, if different from Report)		
18. SUPPLEMENTARY NOTES		
19. KEY WORDS (Continue on reverse side if necessary and identify by block number) deg.		
20. ABSTRACT (Continue on reverse side if necessary and identify by block number) An existing methodology for predicting static and dynamic aerodynamic coefficients was extended to higher angles of attack and Mach numbers. Improvements in existing computational methods were also made. The theory is applicable to bodies of revolution with one or two, piecewise similar-cross section lifting surfaces (2 or 4 in number). The original methodology was applicable to a Mach number of 3 and to an angle of attack of 15°. The capability for dynamic derivative predictions for small angles of attack was extended and improved to Mach numbers of the order 6, above which real (Continued)		

DD FORM 1 JAN 73 1473

EDITION OF 1 NOV 65 IS OBSOLETE  
S/N 0102-014-6601

UNCLASSIFIED

SECURITY CLASSIFICATION OF THIS PAGE (When Data Entered)

411567

UNCLASSIFIED

SECURITY CLASSIFICATION OF THIS PAGE (When Data Entered)

20. Abstract (Continued)

gas effects and much stronger viscous coupling are important. Static aerodynamic prediction capability at small angles of attack was extended and improved to  $M_\infty = 6$ , and an empirical code developed for the Army by G. Aiello of the Martin-Marietta Corp. (Orlando) was adapted for prediction of static aerodynamics at higher angles of attack for a limited configurational envelope. The Martin-Marietta code predicts body-tail aerodynamics for arbitrary roll orientation and angles of attack to  $45^\circ$  for  $0.8 < M_\infty < 3$ . Body-alone and wing-alone (in the presence of the body) components can be computed to  $\alpha = 180^\circ$  and for  $0.8 < M_\infty < 3$ . New individual computational methods are evaluated by comparison with other computational methods and experimental data. The resulting extended computer program was segmented in order to conserve storage locations. Computational times depending on Mach number, configuration, and program option range from under a second to a minute per Mach number on the CDC 6700 computer.

$\alpha$  lpha

deg

deg

M sub infinity

UNCLASSIFIED

SECURITY CLASSIFICATION OF THIS PAGE (When Data Entered)

## FOREWORD

This work has been conducted to expand upon previous work and to provide a design tool for use in estimating the aerodynamics of today's high performance tactical weapons. The resulting computer program, into which this work has been incorporated, allows one to predict performance and to conduct a static and dynamic stability analysis in the preliminary and intermediate design stages without costly and time-consuming wind tunnel tests.

Support for the work was provided by the following sponsors:

The Naval Sea Systems Command under the Surface-Launched Weapons Aerodynamics and Structures Block Program

The Naval Air Systems Command under the Strike Warfare Weaponry/Aerodynamic/Structures Technology Block

The U.S. Army Missile Command under Project No. 1L162303A214

The Office of Naval Research under Project No. F41411

Major procurement contracts from the above funds were let to North Carolina State University, Nielsen Engineering and Research, and Lockheed Missiles and Space Co. Minor contracts were let to General Electric, Armament System Dept., Burlington, Vermont and COMPRO of Fredericksburg, Va.

This report was reviewed and approved by Dr. F. Moore (K21) and Mr. C. A. Fisher (K20).

Accession For	
NTIS GRA&I	<input checked="" type="checkbox"/>
DTIC TAB	<input type="checkbox"/>
Unannounced	<input type="checkbox"/>
Justification	
By	
Distribution/	
Availability Codes	
Avail and/or	
Dist	Special
A	

Released by:

*R. T. Ryland, Jr.*

R. T. RYLAND, Head  
Strategic Systems Department

## ACKNOWLEDGMENT

As indicated in the Foreword and the main report body, the majority of the work presented here was performed under contract. Much of the initial basic approach and selection of contractors was motivated by Dr. F. G. Moore.

A majority of the contract requirement statement and program management work was performed by Dr. J. Sun, who is currently employed by Hughes Aircraft (Canoga Park). Dr. Sun also initiated the integration of the LMSC pitch damping derivative prediction, Martin-Orlando high-angle-of-attack and high Mach number static load prediction coding into the original aerodynamic prediction code.

Other individuals have contributed significantly to the final form of the computer code. Acknowledgment of their contribution will be made in the user's guide, the second portion of this report to be published later.

Contributors to the computations and illustrations in the report were D. Young, V. Morgan, G. O'Connell, K. Buchberger, and G. Haynes of the Aeromechanics Branch.

The contributions of Compo-So-List of Silver Spring, Maryland and the personnel of the Project Publications Branch (E41) in completing this technical report are greatly appreciated.



## CONTENTS

	Page
INTRODUCTION .....	1
ANALYSIS .....	1
CONFIGURATIONAL GEOMETRY .....	1
REVIEW OF PREVIOUS METHODS .....	2
Body-Alone Static Aerodynamics .....	2
Wing and Interference Static Aerodynamics .....	2
Dynamic Derivative Computational Methods .....	4
HIGH MACH NUMBER STATIC AERODYNAMICS .....	4
Body-Alone Inviscid Aerodynamics .....	4
Wing-Alone and Interference Aerodynamics .....	11
HIGH-ANGLE-OF-ATTACK AERODYNAMICS .....	18
IMPROVED DYNAMIC DERIVATIVE PREDICTION .....	21
LMSC Body Pitch Damping .....	21
LMSC Wing-Body Pitch Damping .....	22
Supplemental Dynamic Derivative Prediction .....	24
IMPROVED TRANSONIC NOSE WAVE DRAG PREDICTION .....	26
Background .....	26
Wave Drag Prediction for a Family of Blunted Tangent Ogives .....	27
Wave Drag Prediction for a Family of Blunted Cones .....	29
Method of Analysis for a General Nose Shape .....	31
IMPROVED TRANSONIC NORMAL FORCE PREDICTION .....	32
Background .....	32
Analysis Method .....	32
Evaluation of Current and Old $C_{N\alpha}$ and $C_{m\alpha}$ Predictions .....	37
Modified Functional Form Fit .....	43
SUMMARY OF NEW ANALYSIS METHODS .....	43
INDIVIDUAL METHODS EVALUATION .....	43
HIGH MACH NUMBER STATIC AERODYNAMICS .....	46
Body-Alone Inviscid Aerodynamics .....	46
Wing-Alone Inviscid Aerodynamics .....	46
Complete Configuration Aerodynamics .....	58
HIGH ANGLE-OF-ATTACK AERODYNAMICS .....	58
DYNAMIC DERIVATIVE PREDICTION .....	58
TRANSONIC NOSE WAVE DRAG .....	64
TRANSONIC NORMAL FORCE PREDICTION .....	64
CONCLUDING REMARKS .....	66
REFERENCES .....	73
LIST OF SYMBOLS .....	78
DISTRIBUTION .....	

## ILLUSTRATIONS

Figure		Page
1	General Configurational Geometry . . . . .	2
2	Methods Used to Compute Body-Alone Aerodynamics. . . . .	3
3	Methods Used to Compute Static-Wing-Alone and Interference Aerodynamics. . . . .	3
4	Methods Used to Compute Dynamic Derivatives. . . . .	4
5	Tangent Body Geometry. . . . .	5
6	Wing with Modified Double Wedge Airfoil Section . . . . .	11
7	Wing with Biconvex Airfoil Section . . . . .	12
8	Wing Pressure Distribution . . . . .	13
9	Wing-Body Interference . . . . .	14
10	Geometry of Wing Panel . . . . .	15
11	Geometry for Biconvex Airfoil . . . . .	17
12	Roll Angle and Fin Load Definitions . . . . .	20
13	Pointed Tangent Ogive Wave Drag Coefficients ( $\alpha = 0$ ) . . . . .	29
14	Transonic Pressure Drag for Pointed Cone-Cylinders. . . . .	30
15	Separation Pressure Drag on a Cone-Cylinder . . . . .	31
16	Typical Missile Configuration (Base Configuration). . . . .	33
17	Computational Mesh Configuration for Subsonic Mach Numbers . . . . .	33
18	Quadratic Interpolation Formula for Normal-Force-Curve Slope. . . . .	34
19	Load Distribution for Case 7 . . . . .	38
20	Comparison of Cone-Cylinder and Cone-Alone Data for a Pointed Conical Nose . . . . .	42
21	New Methods for Computing Static Body-Alone Aerodynamics. . . . .	44
22	New Methods for Computing Wing-Alone and Interference Aerodynamics. . . . .	44
23	New Methods for Computing Dynamic Derivatives. . . . .	45
24	NASA Flared-Body Data Comparison . . . . .	47
25	Blunted Cone Aerodynamics. . . . .	48
26	Blunted Tangent Ogive-Forebody Axial Force . . . . .	50
27	Blunted Tangent Ogive-Cylinder, $C_{N\alpha}$ . . . . .	52
28	Blunted Tangent Ogive-Cylinders, $x_{cp}$ . . . . .	54
29	$C_{N\alpha}$ Comparison for a Wing . . . . .	56
30	$C_{Dw}$ Comparison for a Wing . . . . .	57
31	Comparison of Static Aerodynamics for Finned Body at High Mach Numbers ( $\alpha = 0^\circ$ ) . . . . .	59
32	Aerodynamics for TMX-187 ( $M_\infty = 4.65$ , $\alpha = 0^\circ$ ) . . . . .	59
33	$C_N$ Comparison for Air Slew Demonstrator . . . . .	60
34	$x_{cp}$ Comparison for Air Slew Demonstrator Forward of Body Midpoint. . . . .	61
35	$C_q$ Comparison for Air Slew Demonstrator. . . . .	61
36	Modified Basic Finner Aerodynamic Comparison . . . . .	62
37	Army-Navy Spinner Pitch Damping Comparison. . . . .	63
38	Basic Finner Pitch Damping Comparison . . . . .	65
39	$C_{qp}$ Comparison for Army-Navy Basic Finner. . . . .	65
40	M-117 Bomb Nose Wave Drag Comparison . . . . .	66
41	$C_{Af}$ Comparison for Blunted Tangent Ogive-Cylinders . . . . .	67
42	$C_{N\alpha}$ and $x_{cp}$ Comparison for Blunted Tangent Ogive-Cylinders . . . . .	69

## ILLUSTRATIONS (Continued)

Figure		Page
43	Comparison of Theory and Test Data for Improved 5"/54 Projectile . . . . .	70
44	Comparison of Theory and Test Data for 175 mm XM437 Projectile . . . . .	71
45	Comparison of Theory and Test Data for 155 mm Projectile . . . . .	72

## TABLES

Table		Page
1	$C_D = f(R_N, L_N, M_\infty)$ for Blunted Tangent Ogives . . . . .	28
2	Fit Parameters . . . . .	30
3	Cases Calculated for $M_\infty = 0.75$ and $L_B = 1$ . . . . .	35
4	Cases Calculated for $M_\infty = 0.90$ and $L_B = 1$ . . . . .	35
5	Cases Calculated for $M_\infty = 0.95$ and $L_B = 1$ . . . . .	36
6	Cases Calculated for $M_\infty = 1.2$ and $L_B = 1$ . . . . .	36
7	Nose Geometries . . . . .	39
8	$C_{N\alpha}$ and $C_{m\alpha}$ Values for Nose-Alone Cases 2, 6', and A8 . . . . .	39
9	$C_{N\alpha}$ and $C_{m\alpha}$ Values for Nose-Alone Cases, 1, 9, 13, A5, and A10 . . . . .	40
10	$C_{N\alpha}$ and $C_{m\alpha}$ Values for Nose-Alone Cases 4 and A3 . . . . .	40

## INTRODUCTION

This report presents the theoretical basis for the fourth increment in the development of a computer code for the rapid prediction of aerodynamics of tactical weapons in the region  $0 \leq M_\infty \leq 8$  and  $0 \leq \alpha \leq 180^\circ$ .

The general approach has been to combine existing and newly developed approximate computational methods into a single computer program to compute aerodynamics. Computational times, required for the estimate of static and dynamic aerodynamic coefficients for a body-tail-canard configuration for one freestream condition, are in CPU seconds on the CDC 6700 as opposed to minutes or hours required for more detailed physical and numerical models. The accuracy obtained, however, is compatible with that required for preliminary or intermediate design estimates.

The first increment<sup>1</sup> led to the development of a code for the prediction of static aerodynamic coefficients to Mach number 3 and angles of attack to  $15^\circ$  for body-alone configurations.

A second increment<sup>2</sup> supplemented the earlier work and resulted in a code for the prediction of static aerodynamic coefficients for body alone, body-tail, and body-tail-canard configurations for the same range of freestream conditions.

A third increment<sup>3</sup> supplemented the work of the first two increments and extended the computational capability to include the prediction of dynamic derivatives, again for the same range of freestream conditions.

The prime objective of the current work effort is to extend the capability of the aeroprediction code to the higher Mach number and higher angle-of-attack region of advanced designs ( $M_\infty \rightarrow 8$ ,  $\alpha \rightarrow 180^\circ$ ). A secondary objective is to improve the estimate of static derivatives in the transonic Mach number regime and to improve the dynamic derivative prediction capability at all Mach numbers.

## ANALYSIS

### CONFIGURATIONAL GEOMETRY

The basic configurational geometry remains the same as for References 2 and 3. For various Mach number and angle-of-attack regions there are geometric restrictions. These will be elaborated upon in later sections.

Intended applications are for spin-stabilized projectiles, bombs, and rockets (after burn-out) in the unguided class and guided missiles/projectiles. Inlet and plume effects for various weapons are not considered. The code, however, has on occasion been used for some nontactical configurations.

The degree of the configurational complexity that can be considered is illustrated in Figure 1. This most complex body-of-revolution consists of a spherical nose cap, two piecewise-continuous nose sections, a straight afterbody, and a boattail. The wing or canard has a trapezoidal planform with a biconvex or modified double wedge cross section and sharp or spherically blunted leading or trailing edges. Tip edges are assumed parallel to the freestream. Twist or airfoil distortion is neglected and piecewise similar airfoil shape variation with span is assumed.

## REVIEW OF PREVIOUS METHODS

### Body-Alone Static Aerodynamics

A summary of the various methods for computing body-alone aerodynamics appears in Figure 2. The majority of the methods used were adapted from those available in the standard literature.<sup>4-9</sup> The empirical and semiempirical schemes used for the transonic lift and wave drag are presented in some detail in Reference 1. The combined Newtonian-perturbation theory, also presented in Reference 1, was developed so that reasonable results for static aerodynamics could be obtained at low supersonic Mach numbers for blunt-nosed configurations. Mach numbers 0.8 and 1.2 are normal division points for the three Mach number regions.

### Wing and Interference Static Aerodynamics

The methods used to compute lifting surface alone and interference aerodynamics are shown in Figure 3. Methods adapted from the standard literature were taken from References 10 through 16. The remaining methods for wing-body interference, trailing edge separation drag, body base pressure caused by tail fins, and wing drag numerical techniques are detailed in Reference 2.

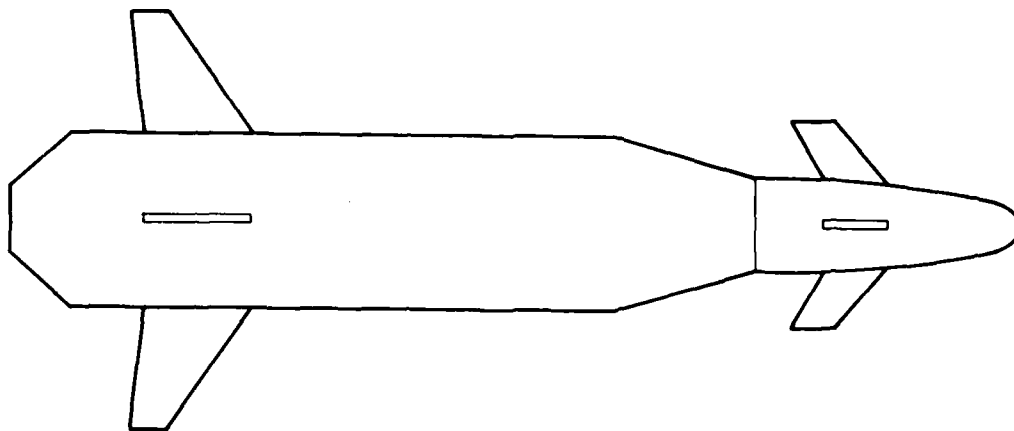


Figure 1. General Configurational Geometry

COMPONENT \ MACH NUMBER REGION	SUBSONIC	TRANSONIC	SUPERSONIC
NOSE WAVE DRAG	—	WU AND AOYOMA PLUS EMPIRICAL	SECOND-ORDER VAN DYKE PLUS MODIFIED NEWTONIAN
BOATTAIL WAVE DRAG	—	WU AND AOYOMA	SECOND-ORDER VAN DYKE
SKIN FRICTION DRAG	VAN DRIEST II		
BASE DRAG	EMPIRICAL		
INVISCID LIFT AND PITCHING MOMENT	EMPIRICAL	WU AND AOYOMA PLUS EMPIRICAL	TSIEN FIRST-ORDER CROSSFLOW
VISCOUS LIFT AND PITCHING MOMENT	ALLEN AND PERKINS CROSSFLOW		

Figure 2. Methods Used to Compute Body-Alone Aerodynamics

COMPONENT \ MACH NUMBER REGION	SUBSONIC	TRANSONIC	SUPERSONIC
INVISCID LIFT AND PITCHING MOMENT	LIFTING SURFACE THEORY	EMPIRICAL	LINEAR THEORY
WING-BODY INTERFERENCE	SLENDER BODY THEORY AND EMPIRICAL		LINEAR THEORY, SLENDER BODY THEORY, AND EMPIRICAL
WING-TAIL INTERFERENCE	LINE VORTEX THEORY		
WAVE DRAG	—	EMPIRICAL	LINEAR THEORY + MODIFIED NEWTONIAN
SKIN FRICTION DRAG	VAN DRIEST		
TRAILING EDGE SEPARATION DRAG	EMPIRICAL		
BODY BASE PRESSURE DRAG CAUSED BY TAIL FINS	EMPIRICAL		

Figure 3. Methods Used to Compute Static-Wing-Alone and Interference Aerodynamics

### Dynamic Derivative Computational Methods

Methods for computing the dynamic derivatives are listed in Figure 4. Applicable references taken from Reference 3 are 10 through 12 and 15 through 26.

### **HIGH MACH NUMBER STATIC AERODYNAMICS**

This work was performed under contract by F. De Jarnette of North Carolina State University during FY 77-FY 80.

No real gas effects are considered, although some real gas effects become important above  $M_\infty = 5$ . Strong viscid-inviscid interactions are neglected. Lifting surface-body interference is neglected. The body base pressure, wing base pressure, body and wing friction routines are the same as those reported in References 1 and 2.

One consideration is the Mach number range of validity of the high Mach number prediction method. This will be discussed in more detail in the methods evaluation section. A Mach number,  $M = M_q$ , will be the dividing Mach number at the lower range limit and is a code input.

### Body-Alone Inviscid Aerodynamics

The method used for pointed bodies with attached shock waves is based on a modification of the method given in Reference 27. For blunt bodies, a modified Newtonian pressure distribution is matched to the second-order shock-expansion pressure distribution. This method is a modification of that used in Reference 28.

COMPONENT \ MACH NUMBER REGION	SUBSONIC	TRANSONIC	SUPERSONIC
BODY-ALONE ROLL DAMPING MOMENT	EMPIRICAL		
WING AND INTERFERENCE ROLL DAMPING	LIFTING SURFACE THEORY	EMPIRICAL	LINEAR THEORY
BODY-ALONE MAGNUS MOMENT	EMPIRICAL		
WING AND INTERFERENCE MAGNUS MOMENT	ASSUMED ZERO		
BODY-ALONE PITCH DAMPING MOMENT	EMPIRICAL		
WING AND INTERFERENCE PITCH DAMPING MOMENT	LIFTING SURFACE THEORY	EMPIRICAL	LINEAR THEORY

Figure 4. Methods Used to Compute Dynamic Derivatives

The perturbation theory of Reference 4 breaks down when the local slope is greater than the Mach angle. For more slender bodies, other nonlinear terms, which are neglected by perturbation theory, become significant at higher Mach numbers even though the local slopes are smaller than the Mach angle. Modified linear theory of the type presented in Reference 29 uses the local  $\beta$  in an iterative solution and avoids the slope-Mach angle limitation. The approach of Reference 4 is probably not applicable at Mach numbers above 4. The current approach is given in Reference 30.

For a body at small angles of attack, the deviation of free streamlines from meridian lines is small and hence is neglected.

From the method of characteristics, for a body of revolution on a free streamline

$$\frac{\partial p}{\partial s} - \frac{2\gamma p}{\sin 2\mu} \frac{\partial \delta}{\partial s} = \frac{1}{\cos \mu} \frac{\partial p}{\partial C_1} \quad (1)$$

$$\frac{\partial p}{\partial C_1} = -\frac{2\gamma p}{\sin 2\mu} \left( \frac{\partial \delta}{\partial C_1} + \frac{\sin \mu \sin \delta}{r} \right) \quad (2)$$

$C_1$  refers to the left running or outgoing characteristic. Incoming characteristics are neglected (i.e., reflection from a bow shock). The angle,  $\delta$ , is the angle of the local streamline tangent;  $s$  is the distance along a streamline. The original body is replaced by a tangent body as shown in Figure 5.

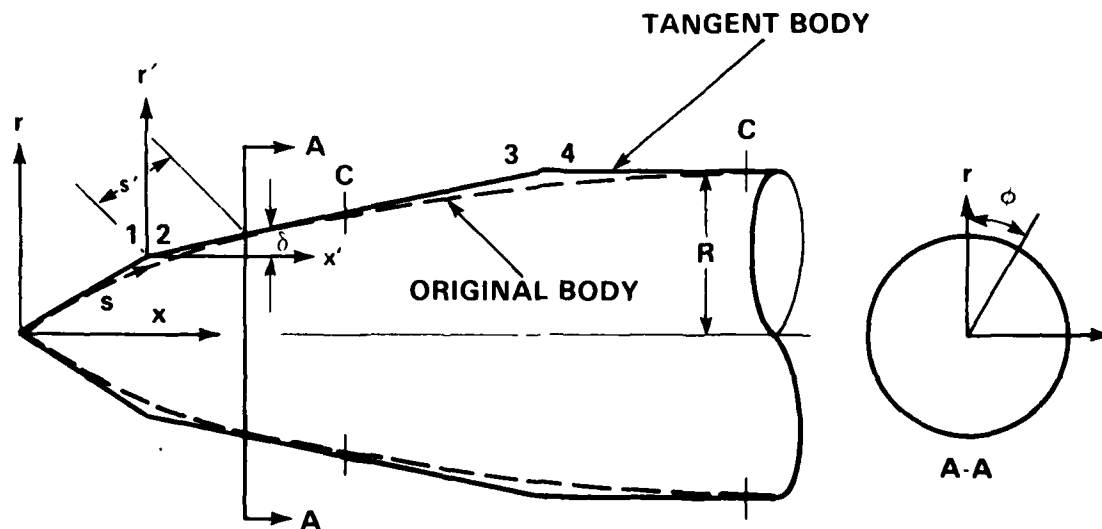


Figure 5. Tangent Body Geometry



The solution starts as a cone solution or as a solution that matches the Newtonian pressure distribution. The match-point procedure will be discussed in detail in a later section.

At a corner such as 1-2, the terms on the right-hand side of Equation 1 are neglected compared with the left-hand side. Thus, at the corner, the well known Prandtl-Meyer relationship holds.

On the straight section 2-3,  $\partial\delta/\partial s = 0$ . If one considers a free streamline close to the surface 2-3, and assumes that the pressure is constant on that streamline, that the  $C_1$  characteristics are straight, that the surface Mach number is a constant, and that  $\Delta C_1$  is a constant, then one can derive approximately (at  $\alpha = 0$  meridian and streamlines coincide)

$$p = k_1 + k_2 e^{k_3 s'} \quad (3)$$

Here,  $s' = x'/\cos \delta$  is the distance from the corner 1-2,  $x'$  is the corresponding horizontal distance from the corner, and  $k_1 = p_a$  is the asymptote for the pressure distribution. For  $\delta \geq 0$  on Section 2-3 and  $s'$  very long,  $p_a$  equals the cone pressure at the freestream Mach number. For  $\delta < 0$ , the assumption is made that  $p_a = p_\infty$  or the freestream pressure. This last assumption can be relatively poor. For  $\delta < 0$ , a pressure distribution approximating the recompression on an conical boattail is needed. In general, Equation 3 must be considered heuristic. The remaining constants can be determined from a knowledge of the pressure,  $p_2$ , and the pressure gradient,  $(\partial p/\partial s)_2$ .

The pressure distribution is then given by

$$p = p_a + (p_2 - p_a) e^{-\eta} \quad (4)$$

$$\eta = \frac{-\left(\frac{\partial p}{\partial s}\right)_2 s'}{(p_2 - p_a)} \quad (5)$$

where  $p_2$  is obtained from the Prandtl-Meyer relationship for an isentropic expansion. Also,

$$\nu_2 - \nu_1 = -(\delta_2 - \delta_1) \quad (6)$$

and

$$\nu = -\int \frac{dp}{\lambda} = \sqrt{\frac{\gamma+1}{\gamma-1}} \tan^{-1} \sqrt{\frac{\gamma-1}{\gamma+1}} (M^2 - 1) - \tan^{-1} \sqrt{M^2 - 1} \quad (7)$$

where

$$\lambda = \frac{2\gamma p}{\sin 2\mu} \quad (8)$$

$$\mu = \sin^{-1} \frac{1}{M} \quad (9)$$

$$\frac{p_0}{p} = \left( 1 + \frac{\gamma - 1}{2} M^2 \right)^{\frac{\gamma}{\gamma - 1}} \quad (10)$$

and  $p_0$  is the stagnation pressure behind a bow shock.

For a compression corner, the isentropic relationship is used. If an isentropic solution for  $p_2$  is not obtainable,  $p = p_a$  is assumed for the straight section. The term  $(\partial p / \partial s)_2$  is obtained from the approximate isentropic relationship from Reference 27. Thus

$$\left( \frac{\partial p}{\partial s} \right)_2 = \frac{B_2}{R} \left( \frac{\Omega_1}{\Omega_2} \sin \delta_1 - \sin \delta_2 \right) + \frac{B_2}{B_1} \frac{\Omega_1}{\Omega_2} \left[ \left( \frac{\partial p}{\partial s} \right)_1 - \lambda_1 \left( \frac{\partial \delta}{\partial s} \right)_1 \right] + \lambda_2 \left( \frac{\partial \delta}{\partial s} \right)_2 \quad (11)$$

where

$$B = \frac{\gamma p M^2}{2(M^2 - 1)} \quad (12)$$

and

$$\Omega = \frac{1}{M} \left[ \frac{1 + \frac{\gamma - 1}{2} M^2}{\frac{\gamma + 1}{2}} \right]^{\frac{\gamma + 1}{2(\gamma - 1)}} \quad (13)$$

The same relationship is used for compression corners.

The pressure relationship breaks down when  $\eta < 0$  and an asymptote cannot be reached. When  $\eta < 0$ ,  $p = p_a$  for an expansion corner and  $p = p_2$  for a compression corner are chosen.

The pressure, which is used for load integration, is evaluated at the tangency points (C) in Figure 5.

Equation 4 provides a solution along a meridian plane surface streamline. For small angles of attack, a pressure coefficient expansion is assumed of the form

$$\begin{aligned}
C_p &= (C_p)_{\alpha=0} - \Lambda \sin 2\alpha \cos \phi + (\Gamma \cos^2 \phi + \Delta \sin^2 \phi) \sin^2 \alpha / 2 \\
&= C_{pa} + (C_{p2} - C_{pa}) e^{-\eta}
\end{aligned} \tag{14}$$

where  $\phi$  is the azimuth angle measured from the leeward plane

$$\Lambda(x) = -\frac{1}{2} \left( \frac{\partial C_p}{\partial \alpha} \right)_{\alpha=0, \phi=0} \tag{15}$$

$$\Gamma(x) = \left( \frac{\partial^2 C_p}{\partial \alpha^2} \right)_{\alpha=0, \phi=0} \tag{16}$$

and

$$\Delta(x) = \left( \frac{\partial^2 C_p}{\partial \alpha^2} \right)_{\alpha=0, \phi=\pi/2} \tag{17}$$

The streamlines make an angle,  $\epsilon$ , with the meridian lines of the order  $\epsilon \sim \sin \phi \sin \alpha$ .  $s'$  is along a surface streamline. Furthermore,  $p_2$  and its  $\alpha$  derivatives are independent of  $\phi$  since  $\epsilon$  is small;  $p_a$ , however is dependent on  $\phi$ .

It may be readily shown that the loading functions  $(C_p)_{\alpha=0}$ ,  $\Lambda$ ,  $\Gamma$ , and  $\Delta$  have the same functional form as Equation 4; i.e.

$$(C_p)_{\alpha=0} = (C_{pa})_{\alpha=0} + (C_{p2} - C_{pa})_{\alpha=0} e^{-\eta} \tag{18}$$

$$\Lambda = \Lambda_a + (\Lambda_2 - \Lambda_a) e^{-\eta} \tag{19}$$

$$\Gamma = \Gamma_a + (\Gamma_2 - \Gamma_a) e^{-\eta} \tag{20}$$

$$\Delta = \Delta_a + (\Delta_2 - \Delta_a) e^{-\eta} \tag{21}$$

$C_{p2}$  is given in terms of  $C_{p1}$  from the Prandtl-Meyer relationships. Differentiation of the Prandtl-Meyer relations with respect to  $\alpha$  once and then twice leads to the following relationships:

$$\Lambda_2 = \frac{\lambda_2}{\lambda_1} \Lambda_1 \tag{22}$$

$$\Delta_2 = \frac{\lambda_2}{\lambda_1} \Delta_1 \tag{23}$$

$$\Gamma_2 = \frac{\lambda_2}{\lambda_1} \left\{ \Gamma_1 + \frac{2\gamma M_\infty^2 \Lambda_1^2}{\lambda_1^*} [G(M_2) - G(M_1)] \right\} \tag{24}$$

where

$$G(M) = \frac{\left[ \frac{\gamma + 1}{2} M^4 - 2M^2 + 2 \right]}{(M^2 - 1)^{3/2}} \quad (25)$$

and

$$\lambda_1^* = \frac{\lambda_1}{p_\infty} = \left[ \frac{\gamma \left( \frac{p}{p_\infty} \right) \left( \frac{p_0}{p_\infty} \right) M^2}{\sqrt{M^2 - 1}} \right]_1 \quad (26)$$

The expressions for  $(C_{pa})_{\alpha=0}$ ,  $\Lambda_a$ ,  $\Gamma_a$ , and  $\Delta_a$  are obtained from an approximation for the asymptotic pressure coefficient; i.e.,

$$C_{pa} = (C_{pa})_{\alpha=0} + \Delta C_p \quad (27)$$

where  $(C_{pa})_{\alpha=0}$  is zero for  $\delta < 0$  and for  $\delta > 0$  is obtained from an approximate relation for the cone solution taken from Reference 31 where

$$(C_{pa})_{\alpha=0} = \sin^2 \delta \left\{ 1 + \frac{(\gamma + 1)K^2 + 2}{(\gamma - 1)K^2 + 2} \ln \left[ \frac{\gamma + 1}{2} + \frac{1}{K^2} \right] \right\} \quad (28)$$

where

$$K^2 = (M_\infty^2 - 1) \sin^2 \delta \quad (29)$$

Equation 28 is accurate except upon approaching the detachment Mach number.

Next,  $\Delta C_p$ , the angle-of-attack dependence of  $C_{pa}$ , is given by a blend of slender body and Newtonian approximations; i.e.

$$\Delta C_p = -\sin 2\alpha \sin 2\delta \cos \phi + \sin^2 \alpha \cos^2 \delta \left[ \left( 2 - \frac{1}{\beta} \right) (1 - \tan^2 \delta) - \left( 2 + \frac{2}{\beta} \right) \sin^2 \phi \right] \quad (30)$$

From Equations 15 through 17 and 30 one can obtain

$$\Lambda_a = \sin 2\delta \quad (31)$$

$$\Gamma_a = 2 \cos^2 \delta \left[ \left( 2 - \frac{1}{\beta} \right) (1 - \tan^2 \delta) \right] \quad (32)$$

and

$$\Delta_a = 2 \cos^2 \delta \left[ \left( 2 - \frac{1}{\beta} \right) (1 - \tan^2 \delta) - \left( 2 + \frac{2}{\beta} \right) \right] \quad (33)$$

In order to start the solution,  $C_{p1}$ ,  $\Lambda_1$ ,  $\Delta_1$ , and  $\Gamma_1$  must be specified as initial values. For a pointed or truncated body, these relations are given by Equations 28, 29, and 31 through 33. For a blunt body (not necessarily spherical), the modified Newtonian pressure distribution may be matched to Equation 14 at some match point. The match point is taken as  $M = 1.1$ , as determined from the isentropic pressure relationship combined with the modified Newtonian pressure relationship evaluated at  $\alpha = 0$ .

The modified Newtonian pressure distribution is given as

$$C_p = C_{p0} (\cos \alpha \sin \delta - \sin \alpha \cos \delta \cos \phi)^2 \quad (34)$$

Comparing Equations 14 and 34 yields

$$C_{p1} = C_{p0} \sin^2 \delta \quad (35)$$

$$\Lambda_1 = C_{p0} \sin \delta \cos \delta \quad (36)$$

$$\Gamma_1 = 2C_{p0} \cos 2\delta \quad (37)$$

and

$$\Delta_1 = -2C_{p0} \sin^2 \delta \quad (38)$$

Evaluation of the loading function Equations 18 through 21 at the end of an interval (point 3 in Figure 5) continues the solution.

Integration of the pressure distribution yields the loading aerodynamic coefficients as

$$C_A = 8 \int_0^{\ell} RR' \left[ (C_p)_{\alpha=0} + \frac{\Gamma + \Delta}{4} \sin^2 \alpha \right] dx \quad (39)$$

$$C_N = 4 \sin 2\alpha \int_0^{\ell} R\Lambda dx \quad (40)$$

and

$$C_{m(\text{about nose})} = -4 \sin 2\alpha \int_0^{\ell} R\Lambda(x + RR') dx \quad (41)$$

All dimensions above are in calibers. The reference area coincides with the maximum nose radius. The second term in Equation 41 is neglected.

## Wing-Alone and Interference Aerodynamics

The geometry used for the wing is the same as that used by Moore.<sup>2</sup> Two basic airfoil shapes are used—the double wedge and the biconvex. Each of these airfoil shapes may have a sharp or blunt leading or trailing edge. Figure 6 shows the planform and airfoil sections for the double wedge, and Figure 7 shows them for the biconvex case. No twist or airfoil distortion is allowed. Piecewise similar airfoil shape variation with span is assumed.

The theory used to determine the pressure distribution is based on two-dimensional supersonic flow properties. At a given point on the surface, the slope of the surface relative to the undisturbed freestream is determined first. If this angle makes a compression surface, the pressure is calculated from tangent wedge theory. In this theory, the angle between the surface and the freestream is the wedge angle used to calculate the pressure. If the angle indicates an expansion surface, the pressure is calculated from Prandtl-Meyer theory for an expansion from freestream properties through this angle. These angles are illustrated in Figure 8, and the two theories are referred to as the tangent-wedge and Prandtl-Meyer theories. For blunted leading edges, modified Newtonian theory is used.

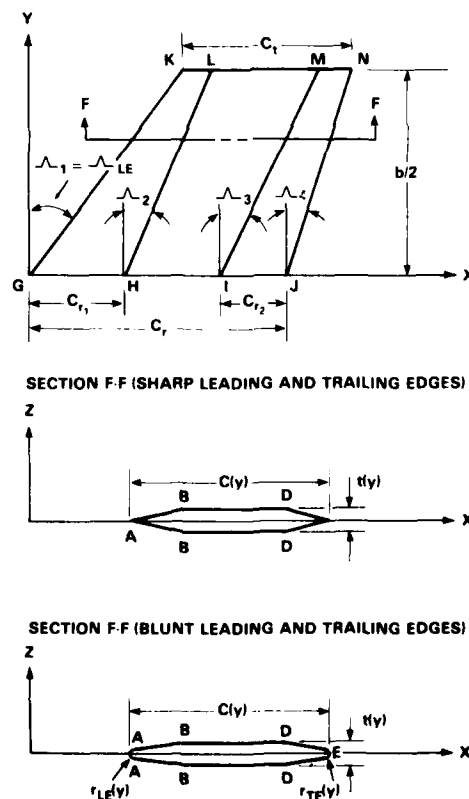
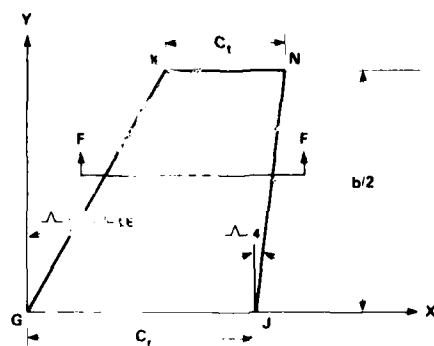
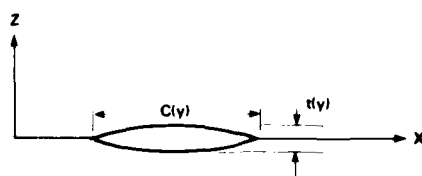


Figure 6. Wing with Modified Double Wedge Airfoil Section



SECTION F-F (SHARP LEADING AND TRAILING EDGES)



SECTION F-F (BLUNT LEADING AND TRAILING EDGES)

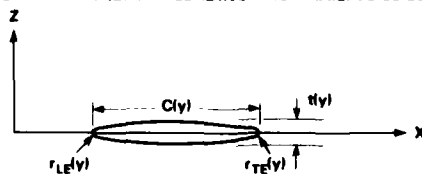


Figure 7. Wing with Biconvex Airfoil Section

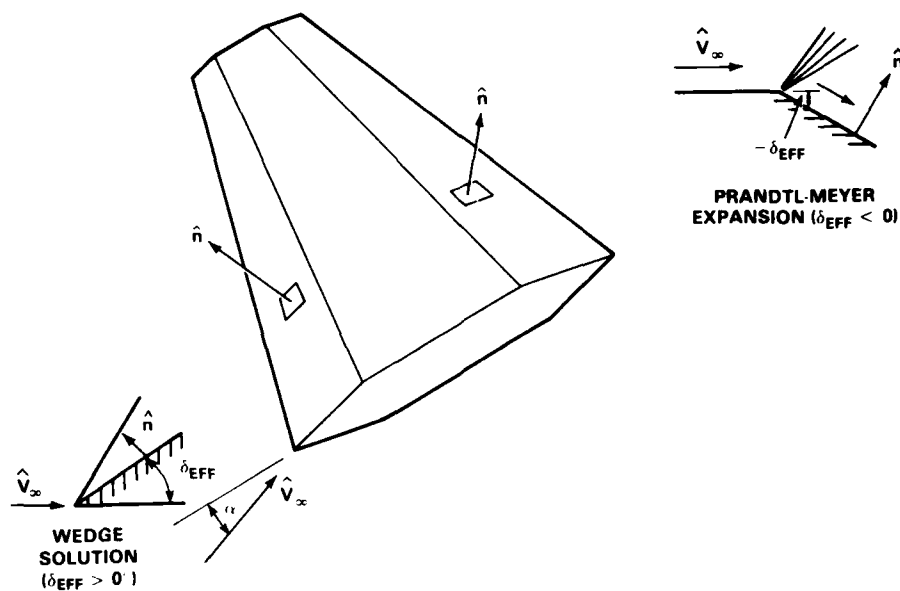


Figure 8. Wing Pressure Distribution

Here

$\hat{n}$  = unit vector normal to the surface

$\hat{V}_\infty$  = unit freestream vector and

$\delta_{\text{eff}}$  = effective deflection angle =  $\sin^{-1}(-\hat{n} \cdot \hat{V}_\infty)$

For a wing connected to a body, the two-dimensional theories described above are in error near the body and the tip of the wing. However, Hilton<sup>32</sup> showed that for a rectangular wing these errors cancel each other (see Figure 9). For wings other than rectangular ones, the errors do not exactly cancel, but the predicted forces and moments have been found to be reasonably accurate.<sup>33</sup>

If the wing pressure is calculated by two-dimensional theory (shock-expansion):

1. The pressure near the body is too low because of wing-body interference
2. The pressure in the tip region is too high because of tip losses

These effects cancel each other and the two-dimensional theory gives the correct force on a rectangular wing.

The body ahead of the most forward wing-body junction point affects the wing loading as does the body close to the root chord junction line. The wing affects the body loading downstream from the forward wing-body junction point. Slender wing-body interference approximations used in Reference 2 are valid only for the low Mach number flow regime.



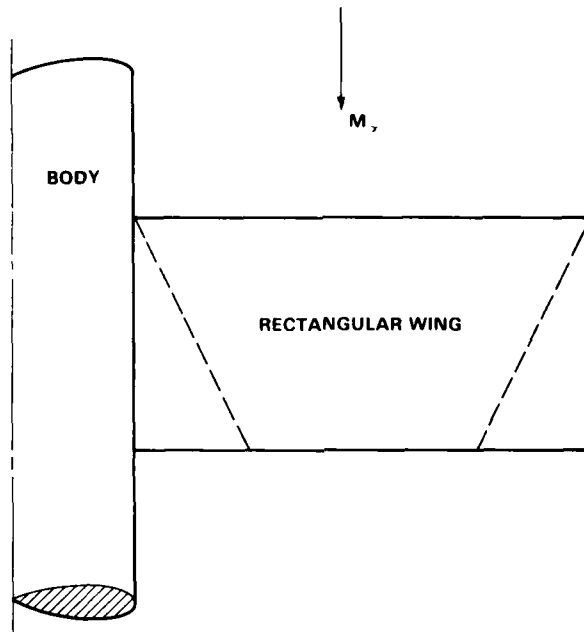


Figure 9. Wing-Body Interference

The double-wedge wing shown in Figure 6 has three flat panels on the top and three flat panels on the bottom. The pressure on each panel is determined by the tangent wedge or Prandtl-Meyer theory, and the pressure is constant over each panel. If the leading edge is blunted, modified Newtonian theory is used to calculate the pressure over the blunted portion in the same manner used by Moore.<sup>2</sup> If the trailing edge is blunted, the empirical two-dimensional base pressures given by Moore<sup>2</sup> are used and then extrapolated for the higher Mach numbers.

Each flat panel is represented by the  $x$ ,  $y$ , and  $z$  coordinates of the four corner points of the trapezoidal surface as shown in Figure 10.

Referring to Figure 10,  $\vec{V}_{1-4}$  is the vector connecting points 1 to 4 and  $\vec{V}_{2-3}$  connects 2 to 3. Then

$$\vec{V}_{1-4} = \Delta x_4 \hat{i} + \Delta y_4 \hat{j} + \Delta z_4 \hat{k} \quad (42)$$

where  $\hat{i}$ ,  $\hat{j}$ , and  $\hat{k}$  are the unit vectors in the  $x$ ,  $y$ , and  $z$  directions, respectively, and

$$\begin{aligned} \Delta x_4 &= x_4 - x_1 \\ \Delta y_4 &= y_4 - y_1 = b/2 \\ \Delta z_4 &= z_4 - z_1 \end{aligned} \quad (43)$$

and

$$\vec{V}_{2-3} = \Delta x_3 \hat{i} + \Delta y_3 \hat{j} + \Delta z_3 \hat{k} \quad (44)$$

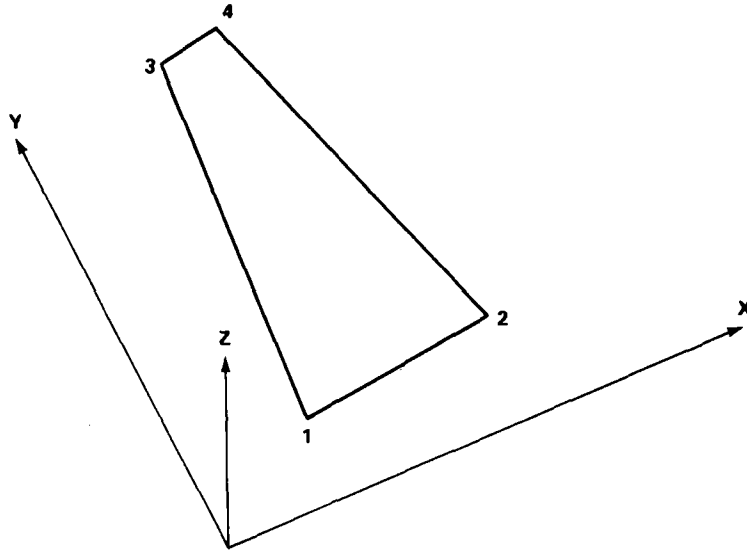


Figure 10. Geometry of Wing Panel

where

$$\begin{aligned}\Delta x_3 &= x_3 - x_2 \\ \Delta y_3 &= y_3 - y_2 = b/2 \\ \Delta z_3 &= z_3 - z_2\end{aligned}\tag{45}$$

The unit vector normal (outer) to the panel is then

$$\hat{n} = \frac{\vec{V}_{1-4} \times \vec{V}_{2-3}}{|\vec{V}_{1-4} \times \vec{V}_{2-3}|}\tag{46}$$

Relative to the wing coordinate system, the unit vector parallel to the freestream velocity vector is

$$\hat{V}_\infty = \cos(\alpha + \delta)\hat{i} + \sin(\alpha + \delta)\hat{j}\tag{47}$$

where  $\alpha$  is the angle of attack and  $\delta$  is the deflection angle of the wing. The effective angle between  $\hat{V}_\infty$  and  $\hat{n}$  is called  $\delta_{\text{eff}}$

where

$$\sin \delta_{\text{eff}} = -\hat{n} \cdot \hat{V}_\infty\tag{48}$$

Performing the indicated vector operations with the equations above, one obtains

$$\sin \delta_{\text{eff}} = \frac{[\cos(\alpha + \delta)(\Delta z_4 - \Delta z_3) + \sin(\alpha + \delta)(\Delta x_3 - \Delta x_4)] b/2}{D}\tag{49}$$

where

$$D = \left\{ [b/2(\Delta z_3 - \Delta z_4)]^2 + [\Delta x_3 \Delta z_4 - \Delta x_4 \Delta z_3]^2 + [b/2(\Delta x_4 - \Delta x_3)]^2 \right\}^{1/2} \quad (50)$$

If  $\delta_{\text{eff}} > 0$ , the tangent wedge theory is used with a wedge angle of  $\delta_{\text{eff}}$ . The explicit wedge solution given by Reference 34 is used here. If  $\delta_{\text{eff}} < 0$ , the Prandtl-Meyer expansion is used with  $|\delta_{\text{eff}}|$  as the expansion angle from freestream conditions.

Once the pressure on each panel is calculated, the axial force, normal force, and pitching moment can be calculated. The effective area for the axial force on a panel is

$$S_A = [z_2 - z_1 + z_4 - z_3]b/4 \quad (51)$$

and therefore the axial force is

$$A = pS_A \quad (52)$$

where  $p$  is the pressure on the panel. Note that  $S_A$  may be positive or negative. The effective area for the normal force on a panel is

$$S_N = [x_2 - x_1 + x_4 - x_3]b/4 \quad (53)$$

and the normal force is

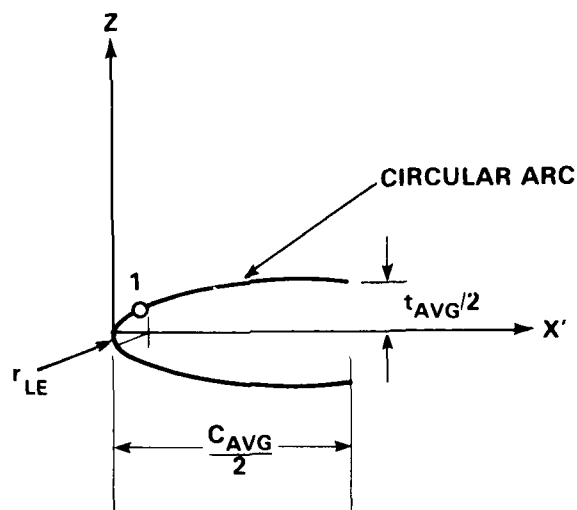
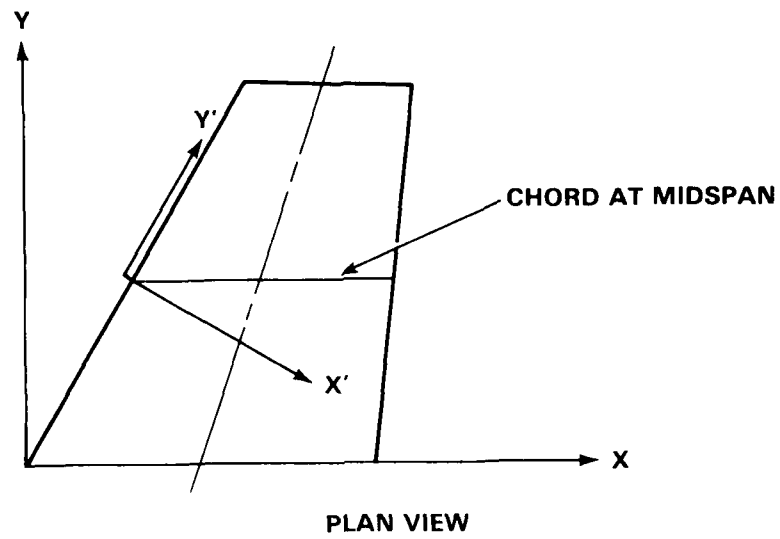
$$N = \pm pS_N \quad (54)$$

where the  $+$  sign is used for panels on the lower surface and the  $-$  sign for panels on the upper surface of the wing.

For biconvex airfoils, it is convenient to divide the wing into a front half for  $x \leq C/2$  and a rear half for  $x \geq C/2$ . The chordwise pressure distribution is calculated for the chord at midspan. The geometry of the wing is shown in Figure 11.

The airfoil section for the front half of the wing is considered first as a cross section perpendicular to the leading edge. In this cross section the airfoil is represented by a circular arc from the midchord position forward to the nose. If the leading edge is sharp, this circular arc extends to the leading edge itself. However, if the leading edge is blunted, the circular arc blends into the cylindrical leading edge. From the geometry of similar triangles, the slope of the circular arc at its most forward position is given by

$$\sin \delta_1 = \frac{-2(\cos \Lambda_{LE} C_{avg}/2 - r_{LE}) \left( r_{LE} - \frac{t_{avg}}{2} \right)}{(\cos \Lambda_{LE} C_{avg}/2 - r_{LE})^2 + \left( r_{LE} - \frac{t_{avg}}{2} \right)^2} \quad (55)$$



AIRFOIL OF FRONT HALF AT MIDSPAN  
( $X'$ ,  $Y'$ ,  $Z$  COORDINATES)

Figure 11. Geometry for a Biconvex Airfoil

and the coordinates of this point are

$$\begin{aligned}x_1 &= r_{LE} (1 - \sin \delta_1) / \cos \Lambda_{LE} \\z_1 &= r_{LE} \cos \delta_1\end{aligned}\tag{56}$$

Now consider the airfoil section in a plane perpendicular to the y-axis. In this plane the circular arc described above is approximated by the parabola

$$z = \frac{\tan \delta_1 \cos \Lambda_{LE}}{\left(x_1 - \frac{C_{avg}}{2}\right)} \left(x - \frac{C_{avg}}{2}\right)^2 + \frac{t_{avg}}{2}\tag{57}$$

This expression can be used to determine the effective angle for the tangent wedge or Prandtl-Meyer theories as

$$\sin \delta_{eff} = \frac{\frac{\tan \delta_1 \cos \Lambda_{LE} \left(x - \frac{C_{avg}}{2}\right) \cos (\alpha + \delta)}{\left(x_1 - \frac{C_{avg}}{2}\right)} \pm \sin (\alpha + \delta)}{\left[1 + \left(\frac{t_R - t_t}{b}\right)^2\right]^{1/2}}\tag{58}$$

where the + sign corresponds to the lower surface and the - sign to the upper surface. For the front half of the wing

$$x_1 \leq x \leq \frac{C_{avg}}{2}\tag{59}$$

The pressure is calculated at 10 positions along this arc and integrated by Simpson's rule to obtain the axial force, normal force, and pitching moment.

The rear half of the wing is handled in the same fashion as the front half.

For configurations with wings and canards, the analysis described above is used to treat each configuration like a separate wing. The contributions for each component are then combined to determine the overall forces and moment.

## HIGH ANGLE-OF-ATTACK AERODYNAMICS

Two basic approaches have been used to predict high angle-of-attack aerodynamics.

The first of these is an empirical approach.<sup>35</sup> Body-alone, fin-alone, fin-in-the-presence-of-a-body, and interference aerodynamic coefficient components are obtained from empirical functional

form fits for a family of body-tails for a given range of angles of attack, Mach numbers, and roll angles. No control deflections are considered.

The second approach is much more elaborate.<sup>36</sup> It uses the semiempirical or heuristic cross-flow analogy with wing-alone loading and other data for body vortex parameters. Vortices from the nose, body, and lifting surfaces are tracked in a stepwise manner with distance along the body centerline. Control deflections are considered. Roll moment and side moment coefficients are predicted as well as longitudinal aerodynamic coefficients. Body-canard-tail configurations as well as body-tail configurations are considered.

Currently, the aeroprediction code contains the coding from References 35 and 37. The method is restricted to body-tail configurations. However, it requires about one-tenth of the storage required for the code in Reference 36, and computational times are much faster. For the currently used method, the range of input parameters for a cruciform configuration are

1. Mach number: 0.8 to 3.0
2. Angle of attack: 0° to 180° for isolated components (roll angle = 0°) and 0° to 45° for body-tail combinations at arbitrary roll angles from 0° to 180°
3. Tail: Trapezoidal planform, edges parallel to body centerline
  - a. Leading edge sweep angle: 0° to 70°
  - b. Taper ratio: 0 to 1
  - c. Aspect ratio (two fins): 0.5 to 2.0
4. Nose length (pointed tangent ogive): 1.5 to 3.0 calibers
5. Cylindrical afterbody: 6 to 18 calibers length and with the end of the body parallel to the tail trailing edge
6. Total span-to-diameter ratio (two fins): 1 to 3-1/3.

Roll angle definition and positive fin load orientation is shown in Figure 12. Note that  $\phi$  is measured 180° from the definition in the aeroprediction code (i.e., the windward side instead of the leeward side).

The axial force coefficient is assumed to be contributed entirely by the body.

The total normal force coefficient is given by

$$(C_N)_{TOT} = C_{NB} + \{ [C_{NT1} + C_{NT3}] \sin \phi + [C_{NT2} + C_{NT4}] \cos \phi \} S_T / S_{ref} + I_{BT} \quad (60)$$

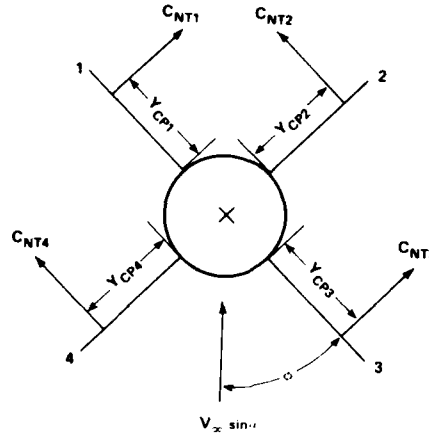


Figure 12. Roll Angle and Fin Load Definitions  
(Looking Forward)

where  $S_T$  is the fin planform area,  $S_{ref}$  is the body reference area,  $C_{NB}$  is the body-alone normal force, Coefficients,  $C_{NTi}$ , are the individual fin loads in the presence of the body and other fins, and  $I_{BT}$  is the tail-to-body carryover normal force coefficient.

The longitudinal center of pressure (from the nose) for the entire configuration is given by

$$\begin{aligned} (x_{cp})_{TOT} = & \{ x_{cpB} C_{NB} + [\sin \phi [(x_{cp})_{T1} C_{NT1} + (x_{cp})_{T3} C_{NT3}] \\ & + \cos \phi [(x_{cp})_{T2} C_{NT2} + (x_{cp})_{T4} C_{NT4}] \} S_T / S_{ref} \\ & + I_{BT} x_{cpl} \} / (C_N)_{TOT} \end{aligned} \quad (61)$$

All  $x_{cp}$  values are given in calibers:  $x_{cpB}$  is the body-alone  $x_{cp}$ ,  $(x_{cp})_{Ti}$  are the individual tail  $x_{cp}$  values in the presence of the body, and  $x_{cpl}$  is the center of pressure for the carryover load.

If one neglects the small body frictional roll coefficient and the tail carryover onto the body, one can estimate the roll coefficient as

$$C_l = \frac{1}{2} S_T / S_{ref} \sum_{i=1}^4 C_{NTi} \sin \left[ (i^2 - i + 1) \frac{\pi}{2} \right] \left[ 1 + \frac{b}{D} \left( Y_{cpi} / \frac{b}{2} \right) \right] \quad (62)$$

Tail carryover data were unavailable for side force and side moment coefficient computations. Details of the individual component functional forms are available in Reference 35 and will not be presented here.

## IMPROVED DYNAMIC DERIVATIVE PREDICTION

A portion of this work was performed under contract by L. Ericsson of Lockheed Missile and Space Co. (LMSC).<sup>38-40</sup> Only  $C_{mq} + C_{m\dot{\alpha}}$  prediction is considered. In fact, the  $C_{m\ddot{\alpha}}$  or contribution term of constant vertical acceleration is not considered. Restrictions on the LMSC code are

1. Body or body-tail configurations
2. Aspect ratio,  $A_w$ , of the wing-alone limited to less than 2.3
3. Initial cylindrical radius for a spherically blunted or truncated body limited to less than 0.25 calibers
4. Contribution of afterbody and boattail or flare are neglected at  $M_\infty \geq \bar{M}^*$  (see Equation 64)
5. Dynamic derivative evaluated in the neighborhood of  $\alpha = 0$ .

At low Mach numbers, one has the option of using the older method. At higher Mach numbers, the contribution of the lifting surfaces needs to be supplemented in regions where the LMSC routine is invalid or not used.

### LMSC Body Pitch Damping

In subsonic flow  $C_{mq} + C_{m\dot{\alpha}}$  is given by a relation based on slender body theory

$$(C_{mq} + C_{m\dot{\alpha}})_B = -4(0.77 + 0.23 M_\infty^2)(\ell \sqrt{0.77 + 0.23 M_\infty^2} - x_{cg})^2 \quad (63)$$

Here  $\ell$  is the body length in calibers and  $x_{cg}$  is the moment and rotation reference point from the nose in calibers. The range of validity is  $M_\infty \leq 1$ .

Hypersonic flow approximations are applied above a certain Mach number,  $M_\infty = \bar{M}^*$ , associated with an effective hypersonic similarity parameter of 0.4 such that

$$\bar{M}^* = 0.4 \csc \bar{\theta}^* \quad (64)$$

$$\bar{\theta}^* = \tan^{-1} \left[ \frac{1}{2L_N} \right] \quad (65)$$

where  $L_N$  is the length of the nose in calibers. If  $\bar{M}^* < 1.5$ , then  $\bar{M}^* = 1.5$  is chosen. For  $M_\infty \geq \bar{M}^*$ , an embedded Newtonian approximation is used. For  $1 < M_\infty < \bar{M}^*$  a linear interpolation is used where

$$\begin{aligned} (C_{mq} + C_{m\dot{\alpha}})_B &= \frac{\bar{M}^* - M_\infty}{\bar{M}^* - 1} (C_{mq} + C_{m\dot{\alpha}})_{B(M_\infty=1)} \\ &+ \left( \frac{M_\infty - 1}{\bar{M}^* - 1} \right) (C_{mq} + C_{m\dot{\alpha}})_{B(M_\infty=\bar{M}^*)} \end{aligned} \quad (66)$$



For  $M_\infty \geq \bar{M}^*$  the computation proceeds as follows:

$$(C_{mq} + C_{m\dot{\alpha}})_B = -16 \int_0^{L_N} C_{po} C_\gamma \frac{(x - x_{cg} + RR')^2 RR'}{(1 + R'^2)} dx \quad (67)$$

where  $R$  and  $R'$  are the body radius in calibers and  $x$  derivative, respectively,  $x$  is in calibers,  $\delta$  is the local surface angle associated with  $R'$  (see Figure 5), and  $C_{po}$  is the stagnation pressure behind a bow shock

$$C_{po} = \frac{\gamma + 3}{\gamma + 1} \left[ 1 + \frac{1.5}{\gamma + 3} \frac{1}{M_\infty^2} \right] \quad (68)$$

Equation 68 is approximate for large Mach numbers. Also

$$C_\gamma = \begin{cases} 1.01 + 1.31 [\log(10 M_\infty \sin \delta)]^{-7/3} & M_\infty \sin \delta \geq 0.4 \\ 1.625 & M_\infty \sin \delta < 0.4 \end{cases} \quad (69)$$

Note that flared bodies are not considered.

#### LMSC Wing-Body Pitch Damping

For  $M_\infty \leq 1$ , slender wing-body theory is used where

$$(C_{mq} + C_{m\dot{\alpha}})_w = (C_{mq} + C_{m\dot{\alpha}})_{wB} - (C_{mq} + C_{m\dot{\alpha}})_B \quad (70)$$

where the subscript  $B$  refers to the body,  $w$  to the wing, and  $wB$  to the wing-body combination. Finally

$$\begin{aligned} (C_{mq} + C_{m\dot{\alpha}})_{wB} = & -4 \left( \frac{D_w}{D} \right)^2 (1 - 0.23 \bar{\beta}^2) \left\{ \left[ x_w \sqrt{1 - 0.23 \bar{\beta}^2} - x_{cg} \right]^2 \right. \\ & \left. - \left[ \frac{x_w D + C_{rw}}{D} - x_{cg} - \bar{C}/D \left( 1 - \sqrt{K_{ma}} \right) \right]^2 \right\} \\ & - 4 \left( \frac{b_w}{D} \right)^2 K_{ma} \left[ \frac{\bar{x}_{te}}{D} - x_{cg} - \bar{C}/D \left( 1 - \sqrt{K_{ma}} \right) \right]^2 \end{aligned} \quad (71)$$

Here  $D$  is the reference diameter of the body,  $D_w$  is the mean diameter of the body near the wing,  $C_{rw}$  is the root chord, and  $x_w$  is the  $x$  distance in calibers from the nose to the beginning of the root chord. Other variables are

$$\bar{\beta} = \sqrt{|1 - M_\infty^2|} \quad (72)$$

$$A_w = \text{aspect ratio} = \frac{2b_w}{C_{rw}(1 + \lambda)} \quad (73)$$

$$\lambda = C_{tw}/C_{rw} = \text{taper ratio} \quad (74)$$

$$\bar{C}/D = C_{rw}/D \left\{ 1 - \left[ (1 - \lambda) - \frac{b_w}{2C_{rw}} \tan \mu \right] \bar{\eta} \right\} \quad (75)$$

$$\bar{\eta} = \frac{1 + 2\lambda}{3(1 + \lambda)} \quad (76)$$

$$\bar{x}_{te}/D = \frac{x_w D + C_{rw}}{D} - \frac{C_{rw}}{D} + \bar{C}/D \quad (77)$$

$$K_{ma} = 2 / \left[ 1 + (A\bar{\beta}/4) + \sqrt{1 + \left( \frac{A\bar{\beta}}{4} \right)^2} \right] \quad (78)$$

and

$$A = (A/A_w) A_w$$

The parameter,  $A$ , is the aspect ratio for the planform obtained by extending the leading and trailing edges to the body centerline, i.e.

$$(A/A_w) = \frac{1 + D_w/b_w}{1 + \frac{D_w}{b_w} \frac{1 - \lambda}{1 + \lambda}} \quad (80)$$

For supersonic flow,  $1 < M_\infty \leq \sqrt{1 + (A_w/4)^2}$  Equation 70 again applies

$$\begin{aligned} (C_{mq} + C_{m\dot{\alpha}})_{wB} = & -4(b_w/D)^2 K_{ma} \left[ \bar{x}_{te}/D - x_{cg} - \bar{C}/D \left( 1 - \sqrt{K_{ma}} \right) \right]^2 \\ & + \left[ 1 - \left( \frac{\frac{x_w D + C_{rw}}{D} - x_{cg}}{x_w - x_{cg}} \right)^2 \right] (C_{mq} + (C_{m\alpha})_B) \end{aligned} \quad (81)$$

For hypersonic flow,  $M_\infty > \sqrt{1 + (A_w/4)^2}$

$$\begin{aligned} (C_{mq} + C_{m\dot{\alpha}})_w = & -8/\pi \frac{C_{rw}}{D} \frac{b_w}{D} \frac{f^*}{\beta} \left\{ \frac{1 + \lambda}{6} + 4\xi^*(\xi^* - a^*) \right. \\ & \left. + \frac{4}{3} a^{*2} - (1 - \lambda)(2\xi^{*2} - 8/3\xi^* a^* + a^{*2}) \right\} \end{aligned} \quad (82)$$

$$\xi^* = \frac{x_w D + C_{rw}}{D} - x_{cg} - \frac{1}{2} \frac{C_{rw}}{D} \quad (83)$$

$$a^* = \frac{1}{2} \frac{C_{rw}}{D} \left( 1 - \lambda + \frac{b_w}{2C_{rw}} \tan \mu \right) \quad (84)$$

$f^*$  is the dynamic pressure ratio across the bow shock and is defined as

$$f^* = \begin{cases} 1.0 & K_N \leq 1.25 \\ 10^{-\frac{K_N - 1.25}{12.669724}} & 1.25 < K_N \leq 11 \\ .17 & K_N > 11 \end{cases} \quad (85)$$

$$K_N = M_\infty \sin \bar{\theta}_N \quad (86)$$

$$\bar{\theta}_N = \sin^{-1} \sqrt{C_{DN}/(C_\gamma C_{p0})} \quad (87)$$

$\bar{\theta}_N$  is an effective cone angle for the bow shock in which the wing is immersed and  $C_{DN}$  is the nose wave drag where

$$C_{DN} = 8 \int_0^{L_N} C_\gamma C_{p0} \sin^2 \delta R R' dx \quad (88)$$

### Supplemental Dynamic Derivative Prediction

The LMSC work was assumed to be able to replace the empirical prediction of Reference 17 for the body-alone pitch damping coefficient. Since the LMSC prediction neglects the effects of an afterbody and a boattail at supersonic Mach numbers, the method of Reference 17 often predicts better values for the pitch damping (as will be shown later). For this reason and because of the other limitations indicated in the last two sections, the pitch damping LMSC prediction for body-alone and body-tail is currently an option in the aeroprediction code. Even when the LMSC package is chosen, the various elements of the package will be bypassed when any of the code restrictions are not met.

At higher Mach numbers, where  $M_\infty > M_Q$ , the potential models for determining the lifting surface roll damping and pitch damping derivatives are assumed to be invalid and are supplemented by the strip theory methods.

For a wing, the strip loading for  $C_{lp}$  and  $C_{mq}$  is assumed to be proportional to the local chord such that

$$\begin{aligned} C_{lp} &= - \frac{N(C_{N\alpha})_w}{D^2 \left( \frac{b_w}{2} \right) \frac{C_{rw}}{2} (1 + \lambda)_w} \int_0^{b_w/2} \left( y + \frac{D_w}{2} \right)^2 C(y) dy \\ &= - \frac{N(C_{N\alpha})_w}{6D^2 b_w (1 + \lambda)} \left\{ (b_w + D_w)^3 \lambda - (D_w)^3 + \frac{1}{4} \frac{(1 - \lambda)}{b_w} [(b_w + D_w)^4 - D_w^4] \right\} \quad (89) \end{aligned}$$

For the wing-alone case,  $D$  is replaced by  $b_w$  for determining  $C_{lp}$ . Equation 89 predicts high values of  $C_{lp}$ . This expression was subsequently replaced by an expression that assumes the loading goes to zero at the tip as  $\sqrt{1 - (y/b_w/2)^2} \rightarrow 0$  such that

$$C_{lp} = - \frac{N(C_{N\alpha})_w \left(\frac{b_w}{C_{ref}}\right)^2}{4I_1} \left[ I_1 \left(\frac{D_w}{b_w}\right)^2 + 2I_2 \left(\frac{D_w}{b_w}\right) + I_3 \right] \quad (90)$$

where  $C_{ref}$  is the reference length and  $N$  is the number of fins.

$$I_1 = \frac{\pi}{4} - \frac{(1-\lambda)}{3}$$

$$I_2 = \frac{1}{3} - \frac{(1-\lambda)\pi}{16}$$

$$I_3 = \frac{\pi}{16} - \frac{2(1-\lambda)}{15}$$

Similarly, for zero roll angle and zero angle-of-attack position

$$\begin{aligned} C_{mq} &= - \frac{4(C_{N\alpha})_w}{D^2(b_w/2)C_{rw}(1+\lambda)} \int_0^{b_w/2} \int_0^{C(y)} (x_{cg} - x_w - y \tan \Lambda_1 - x)^2 dx dy \\ &= - \frac{1}{3} \frac{(C_{N\alpha})_w}{(b_w/2)C_{rw}(1+\lambda)D^2} \left\{ \frac{1}{\tan \Lambda_1} \left[ (x_{cg} - x_w)^4 \right. \right. \\ &\quad \left. \left. - \left( x_{cg} - x_w - \frac{b_w}{2} \tan \Lambda_1 \right)^4 \right] \right. \\ &\quad \left. - \frac{1}{\left[ \tan \Lambda_1 - \frac{C_{rw}(1-\lambda)}{b_w/2} \right]} \left[ (x_{cg} - x_w - C_{rw})^4 \right. \right. \\ &\quad \left. \left. - (x_{cg} - x_w - \lambda C_{rw} - b_w/2 \tan \Lambda_1)^4 \right] \right\} \quad (91) \end{aligned}$$

Here  $(C_{N\alpha})_w$  is the wing-alone  $C_{N\alpha}$  for two fins and  $\Lambda_1 = \Lambda_{LE}$  is the leading edge sweep angle. For the wing alone case,  $D$  is replaced by  $C_{ref} = 2/3 (C_{rw}^2 + C_{tw}^2 + C_{rw}C_{tw})/(C_{rw} + C_{tw})$ . Equations 90 and 91 are applied to both the canard and the tail and added together. Interference is neglected as was the case with the high Mach prediction of F. De Jarnette.

For the wing-alone potential problem for constant roll rate, the loading is zero at the root and the tip. However, for strip theory, the lift problem loading does not vanish at the wing tip.

The  $C_{\ell p}$  and  $C_{m q}$  models given in Equations 90 and 91 will be evaluated in more detail later.

## IMPROVED TRANSONIC NOSE WAVE DRAG PREDICTION

### Background

In Reference 1 the inviscid axial force was assumed to be contributed by a linear superposition of component parts of the body in the transonic flow regime. The nose wave drag was based on a fit to a small disturbance potential model solution for a family of pointed tangent ogive noses. The nose wave drag was fitted as a function of Mach number and nose length. The effect of nose bluntness was ignored.

A separate nose wave drag uncoupled from the boattail and wake effects is valid for supersonic Mach numbers. It is also valid for subsonic Mach numbers where a long cylindrical afterbody follows the nose section.

When the cylindrical afterbody is not long, the boattail wake and nose flow fields are strongly coupled.

Currently, the boattail wave drag is based upon a small disturbance potential solution that assumes a long cylindrical afterbody ahead of the boattail, and a supersonic Mach number close to 1.0. The boattail drag is assumed to decay linearly to zero at  $M_\infty = 0.95$  from the predicted value at  $M_\infty = 1.05$ .

The base drag prediction is empirical and is determined by the expression  $C_{AB} = -C_{pBA}(M_\infty) (R_B/R_{ref})^3$  where  $C_{pBA}(M_\infty)$  is the base pressure coefficient for a long afterbody with no boattail. This empirical relation is approximate and is valid for very small boattail angles and a long afterbody.

For a body with strongly coupled nose, boattail, and wake effects, it would probably be best to vary the sum of the wave drag and base drag for Mach numbers below  $M_\infty = 1.0$  in a manner similar to the variation of  $C_{pBA}(M_\infty)$ . However, this approach was not implemented due to a lack of data.

The remainder of the discussion deals with the case of a separable nose wave drag.

In Reference 41, it is shown that the variation of the nose wave drag is shape dependent. For noses with a finite angle at the shoulder, the pressure drag does not go to zero as the Mach number is decreased due to the effect of the flow separation at the shoulder on the pressure distribution on the nose.

In Reference 41, it is indicated that the nose shapes of interest are bounded approximately by families of cones and ogives. This is the approach taken here.

### Wave Drag Prediction for a Family of Blunted Tangent Ogives

This work was performed under contract by Nielsen Engineering and Research (NEAR). Initially the wave drag was to be based on interpolation between tabulated wave drag values for a family of blunted tangent ogives. The matrix of independent variables for this situation is

$$M_{\infty} = 0.7, 0.95, 1.05, 1.2$$

$$(\text{nose length}) L_N = 0.75, 1.0, 1.25, 1.5, 2.0, 3.0, 4.0, 5.0$$

$$(\text{nose radius}) R_N = 0, 0.05, 0.1, 0.15, 0.2, 0.25, 0.30, 0.35, 0.4, 0.45, 0.5$$

The wave drag is based on pressures generated by a time asymptotic solution of the Euler equations. Details are reported in Reference 42. Actual computations were made at  $R_N = 0.025, 0.05, 0.15, 0.25, 0.35$ , and  $0.5$ ; and  $L_N = 1.5, 3.0, 8.0$ . The computations at  $R_N = 0.5$  are of course independent of nose length. The full geometric matrix was determined by cross plotting and graphical extrapolation and interpolation. Computations for short noses with small bluntness did not agree with the full potential model of Reference 43 or data. Therefore, portions of the wave drag matrix were recomputed using the South-Jameson code.<sup>43</sup> The new matrix generated is previously unpublished data and is given in Table 1 for  $2R_N$  and  $2L_N$ .

First, for variable geometric parameters, the wave drags at a given Mach number are determined by a four-point Lagrange interpolation. Next, for variable nose bluntness, the wave drags at a given nose length are determined by a five-point Lagrange interpolation. Finally, for a given nose bluntness, the final wave drag is computed by a five-point Lagrange interpolation.

Two problems arise in implementing this wave drag algorithm. For blunter noses, the wave drag is still significant for Mach numbers below  $M_{\infty} = 0.8$ . In this case, a quadratic decay to zero wave drag at  $M_{\infty} = 0.5$  is assumed. For pointed ogives, the apex angle may lead to a detached shock at  $M_{\infty} = 1.2$  for  $L_N < 3$ . Small disturbance potential solutions, however, are possible between  $M_{\infty} = 1.2$  and the detachment Mach number provided  $L_N$  is limited to values greater than about 1.75. For  $L_N = 1.75$ , the initial angle is approximately equal to the Mach wave angle at detachment. This coincides with a Mach number of the order 1.5. Figure 13 shows the approximate variation with Mach number for a few pointed tangent ogives. For  $M_{\infty} < 1.2$ ,  $C_D$  is given by the NEAR tabulated data. For  $M_{\infty} > 1.5$  computations are established using a second-order shock-expansion computation program described in an earlier section. Note that the second-order shock-expansion method may not be applied below conic shock attachment Mach numbers with any accuracy. A potential solution of the type described in Reference 1 will fill the gap between  $M_{\infty} = 1.2$  and the attachment Mach number. For  $L_N < 1.75$ , however, the initial slope will be greater than the Mach wave angle, somewhere between  $M_{\infty} = 1.2$  and the shock attachment Mach number.

Table 1.  $C_D = f(R_N, L_N, M_\infty)$  for Blunted Tangent Ogives

$\frac{2R_N}{2L_N}$	0.0	0.1	0.2	0.3	0.4	0.5	0.6	0.7	0.8	0.9	1.0
$M_\infty = 0.8$											
1.5	0.040	0.038	0.037	0.035	0.032	0.028	0.023	0.018	0.015	0.030	0.092
2.0	0.025	0.022	0.016	0.010	0.005	0.002	0.000	0.000	0.000	0.012	0.092
2.5	0.010	0.006	0.004	0.002	0.001	0.000	0.000	0.000	0.002	0.015	0.092
3.0	0.000	0.000	0.000	0.000	0.000	0.000	0.000	0.001	0.005	0.019	0.092
4.0	0.000	0.000	0.000	0.000	0.000	0.000	0.002	0.007	0.012	0.028	0.092
6.0	0.000	0.000	0.000	0.000	0.000	0.000	0.002	0.008	0.023	0.045	0.092
8.0	0.000	0.000	0.000	0.002	0.005	0.010	0.015	0.022	0.037	0.055	0.092
10.0	0.000	0.000	0.000	0.002	0.005	0.010	0.010	0.024	0.042	0.062	0.092
$M_\infty = 0.95$											
1.5	0.160	0.197	0.203	0.203	0.198	0.189	0.180	0.167	0.154	0.150	0.279
2.0	0.080	0.137	0.145	0.138	0.130	0.118	0.103	0.085	0.070	0.122	0.279
2.5	0.040	0.080	0.090	0.089	0.075	0.070	0.063	0.047	0.038	0.110	0.279
3.0	0.015	0.052	0.062	0.062	0.050	0.042	0.034	0.028	0.033	0.116	0.279
4.0	0.000	0.15	0.027	0.027	0.020	0.015	0.012	0.008	0.050	0.132	0.279
6.0	0.000	0.000	0.005	0.002	0.002	0.003	0.010	0.027	0.075	0.152	0.279
8.0	0.000	0.000	0.002	0.002	0.004	0.015	0.018	0.055	0.088	0.160	0.279
10.0	0.000	0.000	0.000	0.002	0.009	0.015	0.025	0.055	0.090	0.164	0.279
$M_\infty = 1.05$											
1.5	0.280	0.333	0.335	0.333	0.329	0.322	0.313	0.300	0.285	0.270	0.405
2.0	0.200	0.268	0.272	0.268	0.262	0.252	0.238	0.221	0.207	0.249	0.405
2.5	0.155	0.220	0.225	0.222	0.213	0.201	0.185	0.170	0.162	0.248	0.405
3.0	0.135	0.165	0.175	0.175	0.167	0.152	0.135	0.130	0.157	0.249	0.405
4.0	0.110	0.130	0.133	0.130	0.122	0.111	0.100	0.102	0.161	0.252	0.405
6.0	0.078	0.080	0.076	0.070	0.064	0.062	0.070	0.105	0.170	0.257	0.405
8.0	0.055	0.050	0.045	0.043	0.047	0.055	0.070	0.105	0.177	0.262	0.405
10.0	0.036	0.032	0.025	0.027	0.037	0.050	0.070	0.105	0.182	0.267	0.405
$M_\infty = 1.2$											
1.5	0.419	0.457	0.468	0.470	0.468	0.460	0.448	0.458	0.418	0.414	0.550
2.0	0.331	0.383	0.397	0.393	0.379	0.364	0.348	0.335	0.328	0.388	0.550
2.5	0.283	0.338	0.332	0.318	0.300	0.286	0.275	0.275	0.290	0.387	0.550
3.0	0.247	0.280	0.273	0.260	0.245	0.231	0.223	0.232	0.285	0.387	0.550
4.0	0.194	0.205	0.190	0.175	0.160	0.155	0.165	0.204	0.280	0.387	0.550
6.0	0.108	0.102	0.092	0.087	0.086	0.102	0.135	0.190	0.278	0.387	0.550
8.0	0.065	0.060	0.050	0.048	0.063	0.095	0.130	0.185	0.275	0.387	0.550
10.0	0.038	0.038	0.038	0.045	0.059	0.090	0.130	0.185	0.273	0.387	0.550

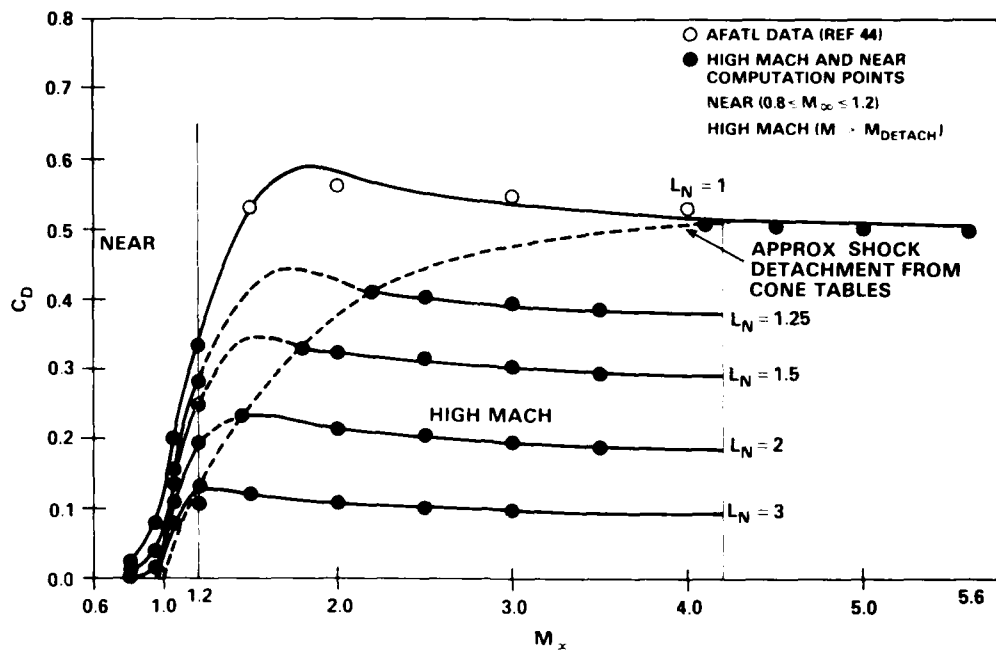


Figure 13. Pointed Tangent Ogive Wave Drag Coefficients ( $\alpha = 0$ )

#### Wave Drag Prediction for a Family of Blunted Cones

As indicated in the introduction and at the beginning of this section, the nose wave drag is shape dependent. The approach taken here is that the nose is either a blunted tangent ogive or a blunted cone. The only alternative would be to use a code such as that presented in Reference 43 to generate families of solutions for various nose shapes.

Figure 14 shows the pressure drag versus Mach number variation for various pointed cones. The pressure drags are established by integration of the pressure data from Reference 45. Note that the transonic flow regime or shock attachment does not start until  $M_\infty > 1.2$  for angles above  $15^\circ$ .

Data were available up to  $\delta = 40^\circ$ . However,  $\delta = 25^\circ$  is about the maximum practical angle for many applications. Note that the pressure drags are higher than those for tangent ogives of the same length. Noses such as secant ogives may be fitted by a cone with the effective cone angle approximately equal to the mean value.

The total forebody drag (pressure drag plus viscous drag) is relatively independent of blunting for Mach numbers below shock attachment.<sup>4,6</sup> Data in Reference 46 are for cones instead of cone-cylinders. The drags are different for the two cases; however, it is assumed that the effect of blunting is the same.

For Mach numbers below  $M_\infty = 0.9$ , separation effects at the cone-cylinder junction affect the pressure on the nose. As the Mach number is lowered, the pressure drag does not go to zero. The



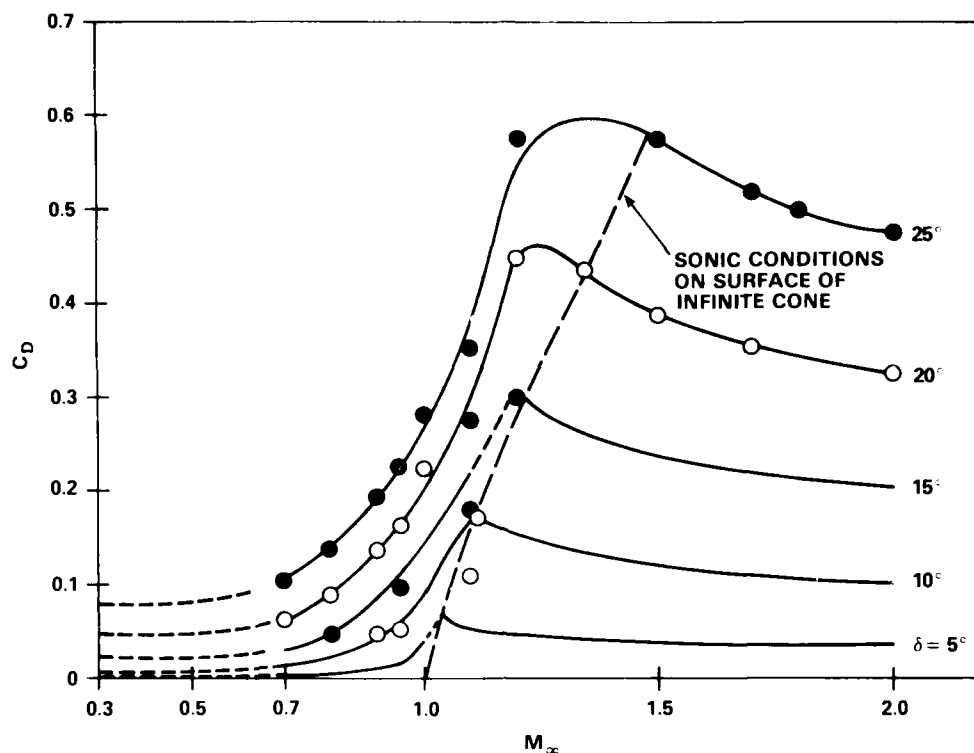


Figure 14. Transonic Pressure Drag for Pointed Cone-Cylinders

residual drag was termed viscous drag in Reference 1. However, the magnitude indicated in Reference 1, is incorrect, since the data used are based on cones rather than cone-cylinders.

The drag behavior below  $M_\infty = 0.7$  was established by the assumed asymptote

$$C_{Ap} = C_{Ap0} + C_{Ap1}e^{-A/M_\infty}$$

All of the undetermined coefficients may be determined from  $C_{Ap}$  data at  $M_\infty = 0.7, 0.8$ , and  $0.9$ . Table 2 gives the resulting fit parameters.

Figure 15 is a plot of  $C_{Ap0}$  against  $\delta$  compared with the asymptote from Reference 1, which is assumed to apply below  $M_\infty = 0.8$  only. The asymptotic behavior determined here is indicated in Figure 14 by dashed curves. For all practical purposes, the asymptote for  $C_{Ap}$  is reached by  $M_\infty = 0.5$ .

Table 2. Fit Parameters

$\delta$	$C_{Ap0}$	$C_{Ap1}$	A
5	0.00041	10.812	10.092
10	0.00780	13.506	5.381
15	0.02464	75.810	6.468
20	0.04871	46.728	5.665
25	0.08037	22.119	4.760

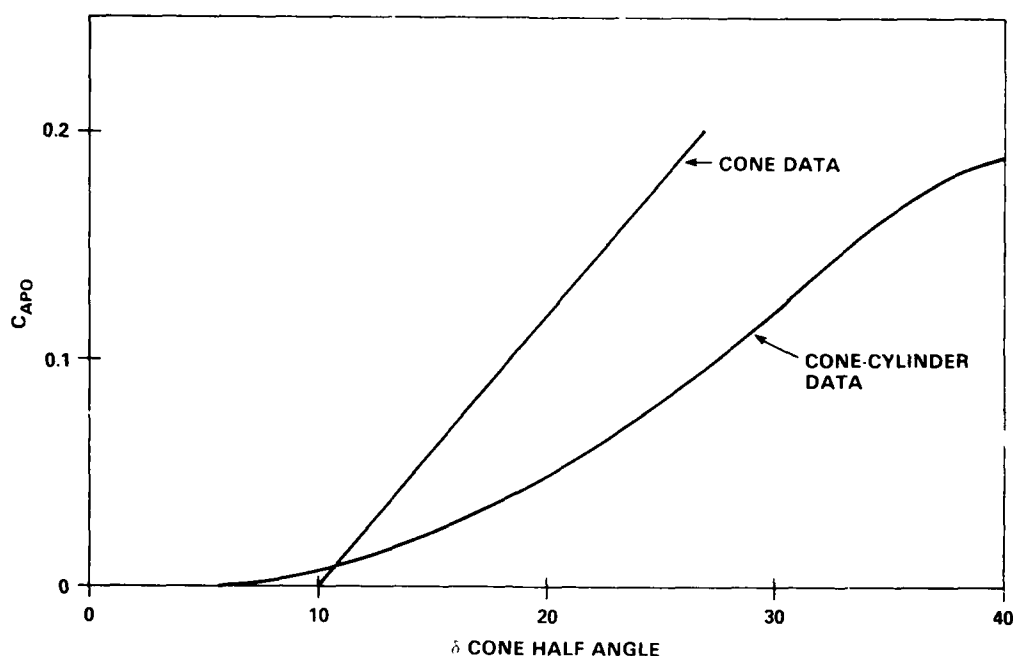


Figure 15. Separation Pressure Drag on a Cone-Cylinder

The pressure drag for cones may then be given by table lookup between the limits  $0.5 < M_{\infty} < 1.5$ . By limiting the angle to  $20^\circ$ , the Mach number range becomes  $0.5 < M_{\infty} < 1.2$ .

#### Method of Analysis for a General Nose Shape

At the beginning of this section, it was indicated that the wave drag is dependent on shape. It remains to estimate the wave drags for nose shapes that are neither blunted tangent ogives or blunted cones. Unfortunately, not enough numerical or test data are available to test any empiricism. It would be advantageous to consider a power law base as well if these data were available.

One possibility is a linear interpolation as given in the relation

$$C_{aw} = \frac{[(C_{aw})_{T.O.}(R'_1 - R'_s) + 2R'_s(C_{aw})_c(\delta_s)]}{R'_s + R'_1} \quad (92)$$

where  $(C_{aw})_{T.O.}$  is the tangent ogive value of wave drag,  $\delta_s$  is the shoulder angle, and  $\delta_1$  is the initial nose angle for a pointed or truncated nose. Here  $\delta_1$  is the initial angle at the end of the spherical cap for a spherically blunted nose and  $(C_{aw})_c(\delta_s)$  is the cone wave drag evaluated at  $\delta_s$ .  $R'_1$  and  $R'_s$  are slopes corresponding to  $\delta_1$  and  $\delta_s$ .

Thus, when the shoulder angle is zero, a tangent ogive value is computed. When the shoulder and initial angle are equal, the cone value is computed. For a truncated body, the radius  $R_N$  is assumed to be that of a pseudosphere that could be added.

Unfortunately, not enough experimental or numerical data are available to test the heuristic expression.

## IMPROVED TRANSONIC NORMAL FORCE PREDICTION

### Background

In Reference 1,  $C_{N\alpha}$  and  $C_{m\alpha}$  were assumed to be contributed by a linear superposition of component parts of the body in the transonic flow regime. Nose properties were assumed to be independent of other parts of the body.

Boattail properties were assumed to be independent of the nose and afterbody. The nose-alone  $C_{N\alpha}$  was based on the cone-alone normal force data and  $x_{cp}$  is given by slender body theory.

The afterbody normal force,  $C_{N\alpha}$ , is given as a function of afterbody length and Mach number independent of other parts of the body. Both  $C_{N\alpha}$  and  $x_{cp}$  are given by the transonic small disturbance theory of Reference 6. For low Mach numbers,  $C_{N\alpha}$  is predicted from data correlation.

For the boattail,  $C_{N\alpha}$  is based on data correlation;  $x_{cp}$  is given by slender body theory. A long afterbody is assumed.

This combination of methods used in Reference 1 was necessitated by the lack of a theoretical and experimental data base at the time Reference 1 was written.

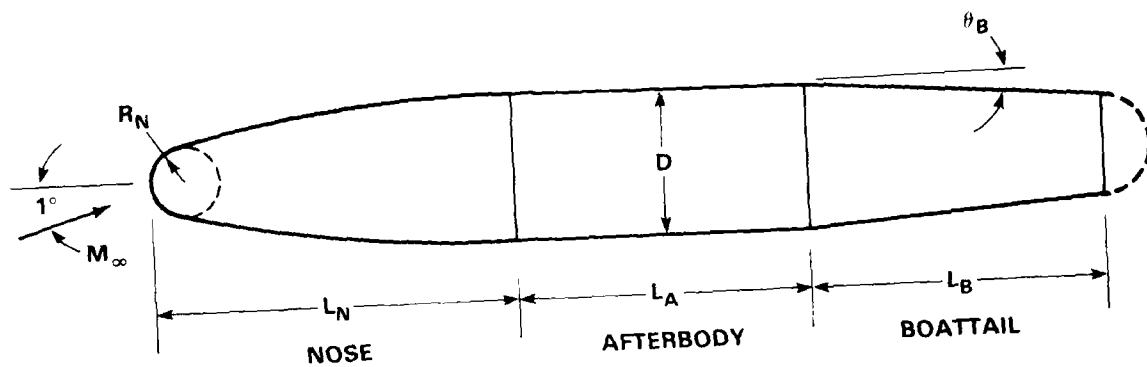
The method of Reference 47 was intended to replace that of Reference 1. The work was performed under contract by NEAR.

### Analysis Method

The method of Reference 47 solves the Euler equations by an implicit time asymptotic method at a  $1^\circ$  angle of attack. The resultant  $C_{N\alpha}$  and  $C_{m\alpha}$  were to be fitted as a function of body geometric parameters and Mach number. Geometric lengths were given in caliber dimensions. The parameter ranges to be considered are taken from Reference 47 and are shown in Figure 16 for bodies with blunted tangent ogive nose shapes.

A number of problems have arisen in implementing this method. For a fairly coarse grid of 48 (points along the body) by 12 (points normal to the body) by 19 (equally spaced circumferential planes), approximately 3900 CDC 7600 CPU seconds are required per configuration. A typical grid taken from Reference 47 is shown in Figure 17. Needless to say, the computational time is prohibitive. For each Mach number, 19 or 20 configurations were considered. In some cases, a completely converged solution was not obtained. In other cases, the grid was too coarse (for longer bodies).

The functional fit form is a truncated Taylor series with free coefficients fitted by least squares. The functional form is shown in Figure 18. The configurations actually computed are given in Tables 3 through 6. 0 in Figure 18 refers to reference conditions,  $\Delta \bar{R}_N = (R_N - .25)/.5$ ;  $\Delta \bar{L}_N = (L_N - 2.5)/5$ ;  $\Delta \bar{L}_A = (L_A - 2.0)/5$ ; and  $\Delta \bar{\theta}_B = (\theta_B - 5)/15$  are the quantities given in Figure 18.



PARAMETER RANGE:

$0.75 \leq M_\infty \leq 1.2$
$0.025 \leq R_N \leq 0.5$
$1.5 \leq L_N \leq 5.0$
$0 \leq L_A \leq 5.0$
$0 \leq L_B \leq 2.0$
$0^\circ \leq \theta_B \leq 10^\circ$

Figure 16. Typical Missile Configuration (Base Configuration)

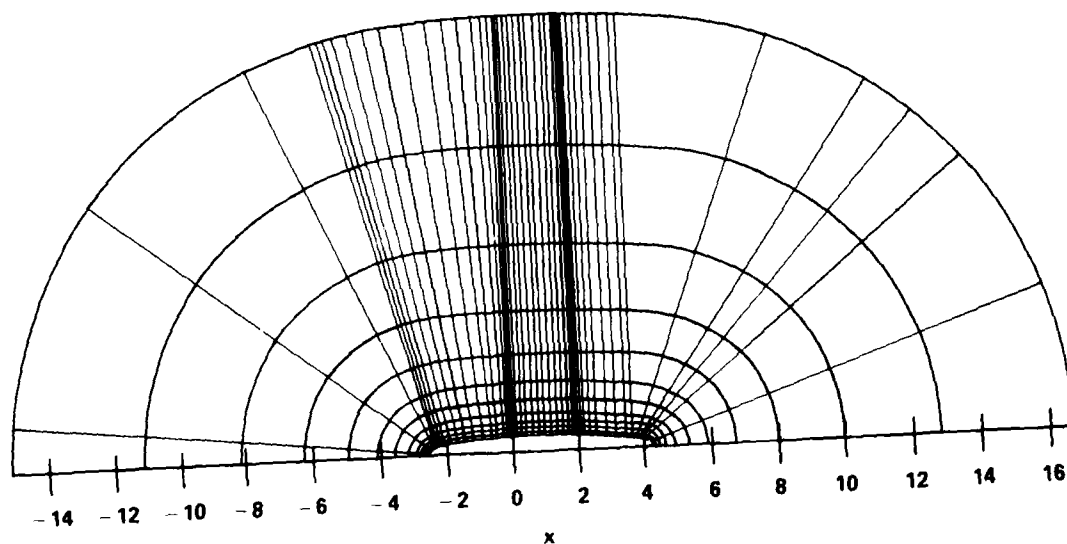


Figure 17. Computational Mesh Configuration for Subsonic Mach Numbers

$$\begin{aligned}
C_{N\alpha} = & (C_{N\alpha})_0 + \left( \frac{\partial C_{N\alpha}}{\partial \bar{R}_N} \right)_0 \Delta \bar{R}_N + \left( \frac{\partial C_{N\alpha}}{\partial \bar{L}_N} \right)_0 \Delta \bar{L}_N + \left( \frac{\partial C_{N\alpha}}{\partial \bar{L}_A} \right)_0 \Delta \bar{L}_A + \left( \frac{\partial C_{N\alpha}}{\partial \bar{\theta}_B} \right)_0 \Delta \bar{\theta}_B \\
& + \left( \frac{\partial^2 C_{N\alpha}}{\partial \bar{R}_N^2} \right)_0 (\Delta \bar{R}_N)^2 + \left( \frac{\partial^2 C_{N\alpha}}{\partial \bar{R}_N \partial \bar{L}_N} \right)_0 \Delta \bar{R}_N \Delta \bar{L}_N + \left( \frac{\partial^2 C_{N\alpha}}{\partial \bar{R}_N \partial \bar{L}_A} \right)_0 \Delta \bar{R}_N \Delta \bar{L}_A + \left( \frac{\partial^2 C_{N\alpha}}{\partial \bar{R}_N \partial \bar{\theta}_B} \right)_0 \Delta \bar{R}_N \Delta \bar{\theta}_B \\
& + \left( \frac{\partial^2 C_{N\alpha}}{\partial \bar{L}_N^2} \right)_0 (\Delta \bar{L}_N)^2 + \left( \frac{\partial^2 C_{N\alpha}}{\partial \bar{L}_N \partial \bar{L}_A} \right)_0 \Delta \bar{L}_N \Delta \bar{L}_A + \left( \frac{\partial^2 C_{N\alpha}}{\partial \bar{L}_N \partial \bar{\theta}_B} \right)_0 \Delta \bar{L}_N \Delta \bar{\theta}_B + \left( \frac{\partial^2 C_{N\alpha}}{\partial \bar{L}_A^2} \right)_0 (\Delta \bar{L}_A)^2 \\
& + \left( \frac{\partial^2 C_{N\alpha}}{\partial \bar{L}_A \partial \bar{\theta}_B} \right)_0 \Delta \bar{L}_A \Delta \bar{\theta}_B + \left( \frac{\partial^2 C_{N\alpha}}{\partial \bar{\theta}_B^2} \right)_0 (\Delta \bar{\theta}_B)^2
\end{aligned}$$

WHERE  $\bar{R}_N = R_N/(R_N)_{\max}$ ;  $\bar{L}_N = L_N/(L_N)_{\max}$ ;  $\bar{L}_A = L_A/(L_A)_{\max}$ ;  $\bar{\theta}_B = \theta_B/(\theta_B)_{\max}$  and  $M_\infty$ ,  
 $L_B$  ARE CONSTANTS

Figure 18. Quadratic Interpolation Formula for Normal-Force-Curve Slope

Table 3. Cases Calculated for  $M_\infty = 0.75$  and  $L_B = 1$ 

Case	Geometric Parameters					Euler Code Values		Least-Square Values	
	$R_N$	$L_N$	$L_A$	$\theta_B$ (Degrees)	$L_B$	$\frac{dC_N}{d\alpha}$	$x_{cp}$	$\frac{dC_N}{d\alpha}$	$x_{cp}$
1	0.25	2.5	2.0	5	1	1.542	-0.4714	1.5776	-0.3262
2	0.05	2.5	2.0	5	1	1.750	0.04893	1.7747	0.2146
3	0.50	2.5	2.0	5	1	1.195	-1.925	1.1821	-1.9698
4	0.25	1.5	0.25	5	1	1.403	0.07262	1.4097	-0.1311
5	0.25	5.0	5.0	5	1	1.478	-2.280	1.4771	-2.2896
6'	0.05	2.5	0.25	0	1	2.393	1.328	2.3513	1.2106
7	0.50	1.5	5.0	0	1	1.935	0.8494	1.9309	0.8773
8	0.50	5.0	0.25	0	1	2.085	1.154	2.0847	1.1991
9	0.25	2.5	2.0	0	1	2.202	1.147	2.2267	1.0143
10	0.05	5.0	5.0	0	1	2.295	2.491	2.2955	2.5022
11	0.50	1.5	5.0	10	1	0.6884	-9.249	0.7051	-8.9992
12	0.50	5.0	0.25	10	1	0.2472	-29.78	0.2479	-30.1348
13	0.25	2.5	2.0	10	1	0.9802	-3.503	0.9470	-3.5864
15	0.05	1.5	0.25	10	1	0.9875	-0.5368	0.9872	-0.6565
A3	0.25	1.5	2.0	5	1	1.548	-0.4303	1.5073	-0.5041
A5	0.25	2.5	5.0	5	1	1.622	-1.326	1.6094	-1.3903
A8	0.05	2.5	2.0	10	1	1.246	-1.464	1.2478	-1.5871
A10	0.25	2.5	0.25	10	1	0.8119	-2.269	0.8249	-1.8410
A11	0.10	1.5	0.25	0	1	2.124	0.0821	2.1458	0.2236

Table 4. Cases Calculated for  $M_\infty = 0.90$  and  $L_B = 1$ 

Case	Geometric Parameters					Euler Code Values		Least-Square Values	
	$R_N$	$L_N$	$L_A$	$\theta_B$ (Degrees)	$L_B$	$\frac{dC_N}{d\alpha}$	$x_{cp}$	$\frac{dC_N}{d\alpha}$	$x_{cp}$
1	0.25	2.5	2.0	5	1	1.498	-0.8088	1.4542	-1.0939
2	0.05	2.5	2.0	5	1	1.689	0.0848	1.6834	-0.0617
3	0.50	2.5	2.0	5	1	1.305	-1.973	1.3115	-1.8470
4	0.25	1.5	0.25	5	1	1.479	-0.03936	1.4685	-0.3115
5	0.25	5.0	5.0	5	1	1.437	-2.764	1.4424	-2.7339
6	0.05	2.5	0.25	5	1	1.494	0.3263	1.6030	0.6461
7	0.50	1.5	5.0	0	1	2.124	1.178	2.1156	1.1613
8	0.50	5.0	0.25	0	1	2.008	0.7239	2.0057	0.7358
9	0.25	2.5	2.0	0	1	2.240	1.113	2.2653	1.0701
10	0.05	5.0	5.0	0	1	2.302	2.433	2.2981	2.4400
11	0.50	1.5	5.0	10	1	0.6003	-12.23	0.6023	-12.3097
12	0.50	5.0	0.25	10	1	0.4092	-18.29	0.4096	-18.4090
13	0.25	2.5	2.0	10	1	0.9875	-3.926	0.9687	-4.0208
15	0.05	1.5	0.25	10	1	1.032	-0.8020	1.0293	-0.8941
A3	0.25	1.5	2.0	5	1	1.388	-1.751	1.4182	-1.3427
A5	0.25	2.5	5.0	5	1	1.562	-1.808	1.5659	-1.7509
A8	0.05	2.5	2.0	10	1	1.369	-1.125	1.3755	-1.0947
A10	0.25	2.5	0.25	10	1	0.8812	-2.247	0.8938	-1.9900
A11	0.10	1.5	0.25	0	1	2.366	0.8041	2.3546	0.3441

Table 5. Cases Calculated for  $M_\infty = 0.95$  and  $L_B = 1$ 

Case	Geometric Parameters					Euler Code Values		Least-Square Values	
	$R_N$	$L_N$	$L_A$	$\theta_B$ (Degrees)	$L_B$	$\frac{dC_N}{d\alpha}$	$x_{cp}$	$\frac{dC_N}{d\alpha}$	$x_{cp}$
1	0.25	2.5	2.0	5	1	1.641	-0.5432	1.5336	-0.9262
2	0.05	2.5	2.0	5	1	1.833	0.2568	1.8396	0.1436
3	0.50	2.5	2.0	5	1	1.361	-2.192	1.3652	-2.1112
4	0.25	1.5	0.25	5	1	1.352	-0.7351	1.3685	-0.8539
5	0.25	5.0	5.0	5	1	1.543	-1.964	1.5733	-1.8363
6	0.05	2.5	0.25	5	1	1.652	0.3024	1.6443	0.3821
7	0.50	1.5	5.0	0	1	2.225	1.048	2.1860	0.9678
8	0.50	5.0	0.25	0	1	2.118	0.6828	2.0962	0.6421
9	0.25	2.5	2.0	0	1	2.193	1.021	2.3506	1.2406
10	0.05	5.0	5.0	0	1	2.330	2.506	2.3057	2.4914
11	0.50	1.5	5.0	10	1	0.5024	-20.17	0.5382	-18.5729
12	0.50	5.0	0.25	10	1	0.7661	-8.846	0.7820	-8.5952
13	0.25	2.5	2.0	10	1	1.252	-2.260	1.0861	-3.4230
15	0.05	1.5	0.25	10	1	1.323	-0.4737	1.3319	-0.4645
A3	0.25	1.5	2.0	5	1	1.442	-1.717	1.4924	-1.3205
A5	0.25	2.5	5.0	5	1	1.632	-1.639	1.6299	-1.6229
A8	0.05	2.5	2.0	10	1	1.456	-0.8952	1.5107	-0.6385
A10	0.25	2.5	0.25	10	1	0.8763	-2.764	0.9269	-2.2428
A11	0.10	1.5	0.25	0	1	2.471	0.8912	2.3989	0.8074

Table 6. Cases Calculated for  $M_\infty = 1.2$  and  $L_B = 1$ 

Case	Geometric Parameters					Euler Code Values		Least-Square Values	
	$R_N$	$L_N$	$L_A$	$\theta_B$ (Degrees)	$L_B$	$\frac{dC_N}{d\alpha}$	$x_{cp}$	$\frac{dC_N}{d\alpha}$	$x_{cp}$
1	0.25	2.5	2.0	5	1	2.136	0.1233	2.1773	0.6058
2	0.05	2.5	2.0	5	1	1.989	0.7118	1.9209	0.3301
3	0.50	2.5	2.0	5	1	2.167	0.0200	2.1823	0.0313
4	0.25	1.5	0.25	5	1	2.740	0.6582	2.7247	0.7038
5	0.25	5.0	0.50	5	1	2.334	1.403	2.3160	1.2874
6'	0.05	2.5	0.25	0	1	2.500	1.494	2.5538	1.5969
7	0.50	1.5	5.0	0	1	2.584	0.8771	2.6007	0.9326
8	0.50	5.0	0.25	0	1	2.592	0.7101	2.6184	0.7563
9	0.25	2.5	2.0	0	1	2.562	0.8747	2.4646	0.5613
10	0.10	5.0	5.0	0	1	2.180	-1.888	2.1965	-1.7688
11	0.50	1.5	5.0	10	1	1.983	-1.035	1.9505	-1.1661
12	0.50	5.0	0.25	10	1	1.894	-0.9524	1.8917	-0.9216
13	0.25	2.5	2.0	10	1	1.833	-0.6771	1.9130	-0.2967
15	0.05	1.5	0.25	10	1	2.176	0.7843	2.1743	0.8177
A3	0.25	1.5	2.0	5	1	2.247	-0.0886	2.2748	-0.1955
A5	0.25	2.5	5.0	5	1	2.265	-0.0367	2.2831	0.0177
A8	0.05	2.5	2.0	10	1	1.751	0.0354	1.7516	0.1103
A10	0.25	2.5	0.25	10	1	2.323	0.7546	2.2464	0.4127
A11	0.10	1.5	0.25	0	1	2.846	1.153	2.8508	1.1936

The Taylor series is used for the nose-alone; afterbody-alone; and 0.5-, 1.0-, and 1.5-caliber boattails. In the actual computations, only a 2-caliber boattail is considered. The loading on 0.5-, 1.0-, and 1.5-caliber boattails is obtained by integrating over the truncated portion of the full 2-caliber boattail.

The interpolation procedure proceeds as follows: At  $M_\infty = 0.6$ , the nose-alone, afterbody-alone, and boattail-alone  $C_{N\alpha}$  and  $C_{m\alpha}$  values are obtained by the method of Reference 1. Next, at  $M_\infty = 0.75, 0.9, 0.95$ , and  $1.2$ , the nose-alone; afterbody-alone; and 0.5-, 1.0-, and 1.5-boattail-length contributions to  $C_{N\alpha}$  and  $C_{m\alpha}$  are determined from the Taylor series. At each Mach number, the boattail-alone contribution is determined by a four-point Lagrange interpolation for the boattail length of interest. For a zero length boattail,  $C_{N\alpha}$  and  $C_{m\alpha}$  contributed by the boattail are zero. Finally, the nose-alone, afterbody-alone, and boattail-alone contributions are determined at the Mach number of interest by a five-point Lagrange interpolation in the values at  $M_\infty = 0.6, 0.75, 0.9, 0.95$ , and  $1.2$ . Since two different methods are used, a smooth merge would not be expected at  $M_\infty = 0.6$ . At  $M_\infty \geq 1.20$  the code as currently written would transfer to a potential code for the low supersonic range. Again, a smooth merge would not be expected for the current new coding or the older coding at  $M_\infty = 1.20$ .

At subsonic Mach numbers, the hemispherical end configuration leads to poor pressure distribution prediction on the aft end of the body, especially for  $\theta_B = 0^\circ$ . Some guidance from flow visualization is needed in choosing a free streamline wake boundary which may be approximated by a solid surface. The next best thing is an extended smoothly varying stinglike wake free streamline. The alternative is to couple a boundary layer and transonic computation such as used in Reference 48. The model of Reference 48 would have to be extended to include a recirculation model near the base or a knowledge of the free streamline shape.

Examination of  $dC_N/dx$  in Reference 47 (see Figure 19) indicates that this model predicts a boattail loading at  $\theta_B = 0$ . This is questionable, particularly for  $M_\infty = 1.2$ , for the example shown in Figure 19. Unfortunately, the  $\theta_B = 0$  numerical data are included in the Taylor series fit. The truncated portions of a 2-caliber boattail are not the same as those of 0.5-, 1.0-, and 1.5-caliber boattails. However, the prohibitive computational cost led to the current approach.

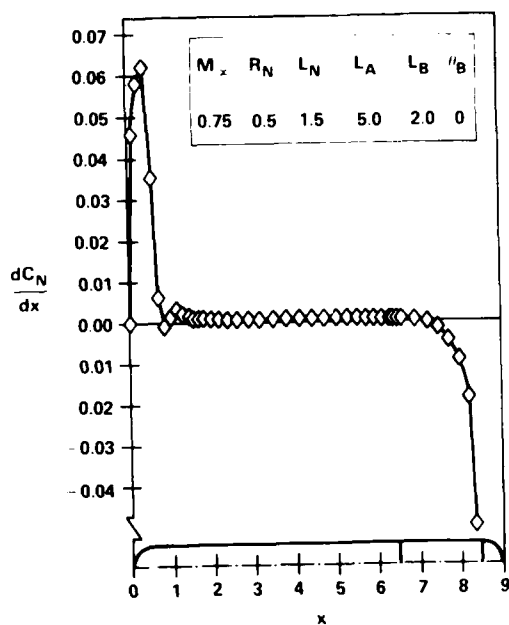
A proper evaluation of the current method would ideally require extensive  $dC_N/dx$  distribution data or  $C_p$  data that could be used to determine  $dC_N/dx$ . The majority of the data available are total load data for complete configurations. However, the basic input data to the fits need to be examined and evaluated as well.

#### Evaluation of Current and Old $C_{N\alpha}$ and $C_{m\alpha}$ Predictions

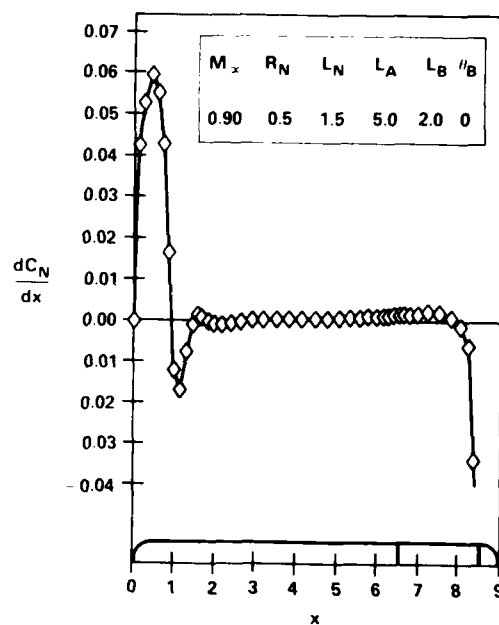
One limit that one could examine is the case of a long constant radius afterbody. In principle, the nose and boattail should be isolated in this case. Indeed, this was the assumption of Reference 1.

Nose-Alone Contribution. Nose geometry considered could be listed as (see Tables 3-6) in Table 7.

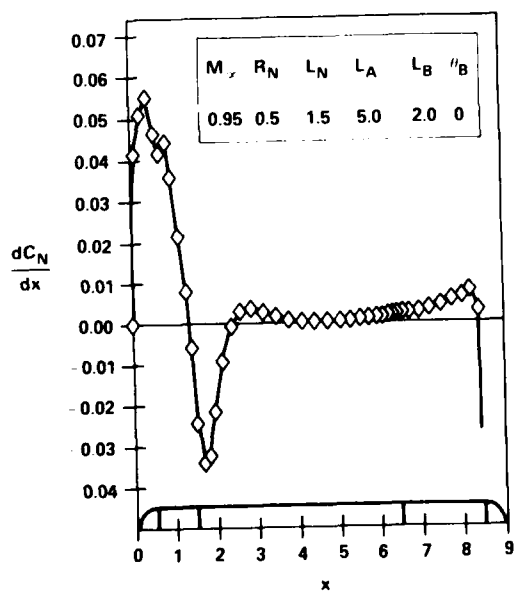




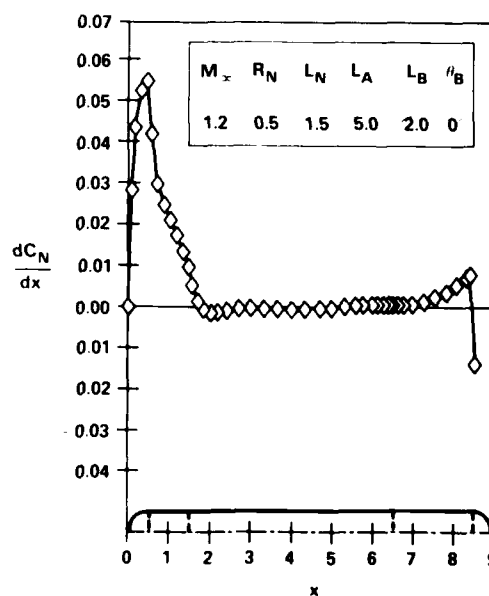
(a)  $M_\infty = 0.75$



(b)  $M_\infty = 0.90$



(c)  $M_\infty = 0.95$



(d)  $M_\infty = 1.20$

Figure 19. Load Distribution for Case 7

Table 7. Nose Geometries

$R_N$	$L_N$	Case(s)
0.05	1.5	15
0.05	2.5	2, 6', A8
0.05	5.0	10 (not for $M_\infty = 1.2$ )
0.1	1.5	All
0.1	5.0	10 (only for $M_\infty = 1.2$ )
0.25	1.5	4, A3
0.25	2.5	1, 9, 13, A5, A10
0.25	5.0	5
0.5	1.5, 2.5, 5	(7, 11), (3), (8, 12)

The hemispherical cases shown in Table 7 are used in the fits. In actual usage, a hemispherical cap is given by  $R_N = 0.5$ ,  $L_N = 0.5$ .

Values of  $C_{N\alpha}$  and  $C_{m\alpha}$  for the nose alone were taken from unpublished data obtained from G. Klopfer. Computational data for cases 2, 6', and A8 are tabulated in Table 8. Cases 2, 6', and A8 have different values of  $L_A$  and  $\theta_B$ . However, the data seem to indicate that the assumption of nose contribution independent of afterbody and boattail is not too bad.

Cases 1, 9, 13, A5, and A10 also have a common nose. The nose-alone contribution is tabulated in Table 9.

Again, the trend toward nose-alone values independent of the aft portion of the body is apparent. An exception is for cases 4 and A3. For a nose as blunt as in cases 4 and A3, the afterbody and boattail apparently influence the nose. Case 4 has a very short  $L_A = 0.25$ , as opposed to  $L_A = 2$  for case A3.

However, the numerical data base available to take advantage of this result is far too small. The values at  $M_\infty = 1.2$  are suspect since for case 10 a value of  $C_{N\alpha} = 3.03$ , which is much too high, is obtained for the nose. Including dependence of  $C_{N\alpha}$  and  $C_{m\alpha}$  on  $L_A$  and  $\theta_B$  in the curve fit for the nose, distorts the contribution of these elements.

Table 8.  $C_{N\alpha}$  and  $C_{m\alpha}$  Values for Nose-Alone Cases 2, 6', and A8

$M_\infty$ /Nose-Alone	$C_{N\alpha}$			$C_{m\alpha}$		
	Case 2	Case 6'	Case A8	Case 2	Case 6'	Case A8
0.75	2.31	2.28	2.14	-2.86	-2.79	-2.76
0.9	2.24	2.17	2.33	-2.87	-2.75	-3.15
0.95	2.45	2.46	2.44	-3.37	-3.39	-3.35
1.2	2.28	2.28	2.25	-2.97	-3.14	-2.95

Table 9.  $C_{N\alpha}$  and  $C_{m\alpha}$  Values for Nose-Alone Cases 1, 9, 13, A5, and A10

$M_\infty$ /Nose-Alone	$C_{N\alpha}$	$C_{m\alpha}$
	Cases 1, 9, 13, A5, A10	Cases 1, 9, 13, A5, A10
0.75	2.07, 2.07, 2.08, 2.06, 2.07	-2.04, -2.04, -2.05, -2.01, -2.01
0.90	2.12, 2.15, 2.16, 2.13, 2.23	-2.01, -2.03, -2.11, -2.00, -2.25
0.95	2.38, 2.30, 2.38, 2.41, 2.40	-2.58, -2.29, -2.58, -2.57, -2.52
1.2	2.73, 2.78, 2.72, 2.64, 2.80	-3.21, -3.46, -3.24, -3.30, -3.54

Table 10.  $C_{N\alpha}$  and  $C_{m\alpha}$  Values for Nose-Alone Cases 4 and A3

M	$C_{N\alpha}$		$C_{m\alpha}$	
	Case 4	Case A3	Case 4	Case A3
0.75	2.01	2.05	-1.43	-1.48
0.9	2.45	2.72	-1.95	-2.11
0.95	2.47	2.74	-2.01	-2.15
1.2	2.94	2.74	-2.52	-2.28

A better approach would have been to use a potential model such as developed in Reference 49 for noses plus very long afterbodies. A possible fit would be

$$(C_{N\alpha})_N = F(R_N, L_N) + \frac{G(L_A, \theta_B)}{L_A + K_1} \quad (93)$$

The last term would provide correction terms for short  $L_A$  bodies. For supersonic Mach numbers the second term in Equation 93 would not be needed.

Another question that arises is to what extent the nose loading is dependent on the shape of the nose. Reference 1 bases the nose loading on the cone-alone data from Reference 46 where

$$(C_{N\alpha})_N = C_1(M_\infty) \tan \delta^* + C_2(M_\infty) \quad (94)$$

where  $\delta^*$  is the angle at the shoulder. Thus, for the family of blunted tangent ogives, the prediction is  $(C_{N\alpha})_N = C_2(M_\infty)$  or independent of the nose parameter. For  $\tan \delta^* \rightarrow 0$ ,  $(C_{N\alpha})_N \rightarrow 2.0$  is the trend of the data for cones. However,  $C_2(M_\infty)$  is above 2.0 for higher Mach numbers; this is just a property of the force fit.

Computations from Reference 47 and data from Reference 49 indicate that  $(C_{N\alpha})_N$  for blunted tangent ogives is above 2.0. Data from References 45 and 46 indicate that  $(C_{N\alpha})_N$  is less than 2. Reference 46 indicates that bluntness does not greatly affect  $(C_{N\alpha})_N$  in the transonic flow regime for cones for Mach numbers below the shock attachment Mach number for a pointed cone.

Figure 20 is a comparison between the integrated data of Reference 45 for cone-cylinders and the values obtained in Reference 1 for cones alone. The fit from Reference 1 is low for  $C_{N\alpha}$  for the three cone angles plotted. However,  $x_{cp}/L_N$  predicted by slender-body theory is too high compared with data, except below  $\delta = 10^\circ$  cone angle. Percentagewise the deviation is not too great for  $x_{cp}/L_N$ . The integrated data from Reference 45 has some scatter but follows a general trend with the slender-body limit clearly being approached as  $\delta \rightarrow 0$ .

**Afterbody-Alone Contribution.** Here the data trends and computational trends are even less clear. Reference 1 assumes that the carry over from the nose or boattail is negligible and  $(C_{N\alpha})_A$  and  $(x_{cp})_A/L_A$  are a function of afterbody length and Mach number alone. The data of Reference 1 also indicate that  $(C_{N\alpha})_A$  is monotonic, increasing to an asymptote as  $L_A$  grows. The  $(C_{N\alpha})_A$  from Reference 1 appears to be representative of the  $C_{N\alpha}$  buildup on the afterbody for a long afterbody with a slender nose and a very small angle at the shoulder.

For cone-cylinders,  $C_{N\alpha}$  buildup is available from Reference 45. For ogive-cylinders, only  $C_{N\alpha}$  as a function of afterbody length (Reference 50) is available. Unfortunately, nose-alone data are not available in References 50 or 51, which also considers power-law nose shapes. In References 50 and 51, the minimum afterbody length is 4. Data from References 45 and 50 indicate that  $C_{N\alpha}$  continues to increase with afterbody length in an almost linear manner rather than going to an asymptote. The magnitude of the linear slope cannot be accounted for by a viscous crossflow correction, which is also linear with  $L_A$ , since it would require angles of attack of the order of  $10^\circ$  or more. The magnitude  $(C_{N\alpha})_A$  for a  $10^\circ$  cone-cylinder is also larger in Reference 45 than in Reference 1. The  $(C_{N\alpha})_A$  contribution for a  $10^\circ$  cone at  $M = 1.1$  increases with  $L_A$  to a maximum at about 1.5 caliber, then down to a minimum at about 3 calibers, and then increases in a steady linear manner with increasing  $L_A$ . The data for Reference 50 are only for  $L_A$  of 4 calibers or greater.

Whereas, the available data and Reference 1 predict an incremental  $(C_{N\alpha})_A$ , which is positive, the computations of Reference 47 predict both positive and negative values. The computations of Reference 47 predict positive increments on the afterbody only for a  $0^\circ$  boattail angle.

No comment will be made on the  $x_{cp}$  prediction since the  $C_{N\alpha}$  prediction accuracy is uncertain.

**Boattail-Alone Contribution.** Here the data available are almost nonexistent. Reference 1 uses a extremely limited data base from essentially one source<sup>5,2</sup> to establish an empirical prediction. Reference 1 indicates that the correlation is supplemented with data for the 5"/54 improved and 175 mm projectiles. This would bias the correlation for these projectiles since it is assumed that the nose and afterbody predictions are correct. Again,  $x_{cp}$  is given by a slender-body estimate. The expression given in Reference 1 is not correct and should be

$$(x_{cp})_B = C \frac{[I_B S_{ref} + (Vol)_B]}{S_{ref} + S_B} \quad (95)$$

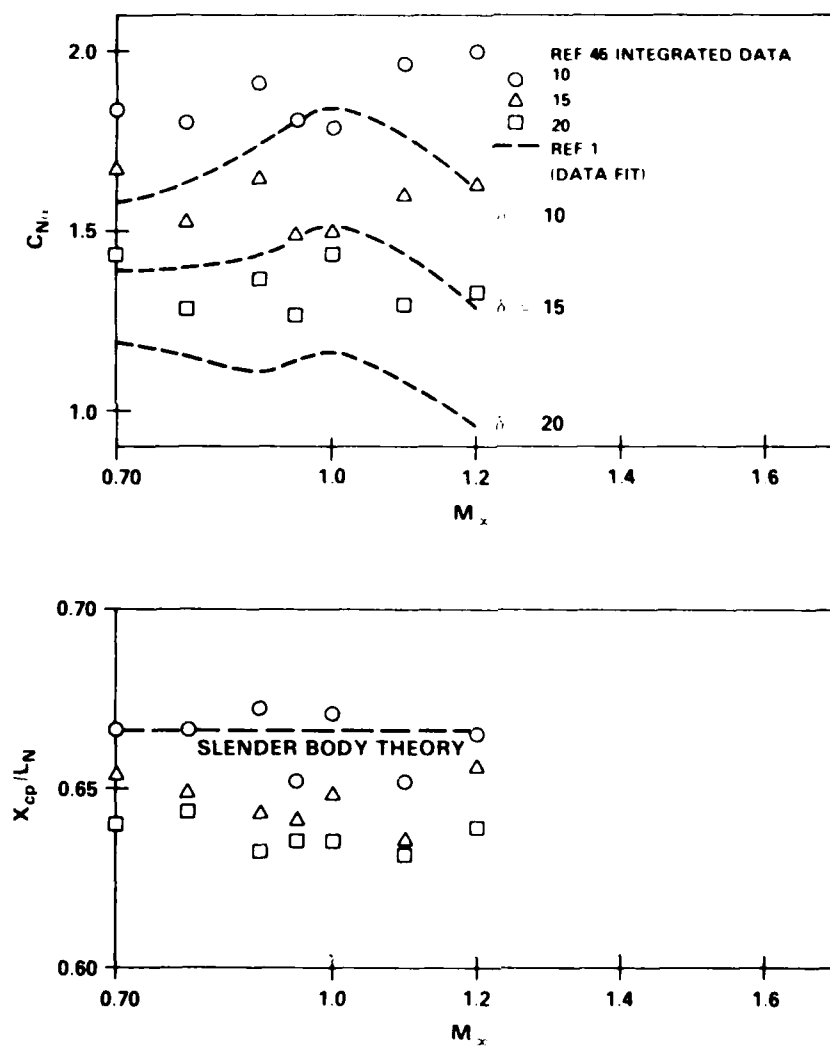


Figure 20. Comparison of Cone-Cylinder and Cone-Alone Data for a Pointed Conical Nose

where  $(x_{cp})_B$  is the center of pressure in calibers,  $\ell$  is the body length in calibers,  $L_B$  is the boattail length in calibers,  $(Vol)_B$  is the boattail volume,  $S_{ref} = \pi/4$ ,  $S_B = \pi R_B^2$ , and  $R_B$  is the cylindrical radius at the end of the body in calibers.

For a finite angle boattail, the computations of Reference 1 predict a downloading. The computations of Reference 47 predict positive and negative loading for a  $0^\circ$  boattail, which is really a continued afterbody.

#### Modified Functional Form Fit

A preliminary analysis of the previous paragraphs indicates that both the original and the more recent prediction methods have some shortcomings. The NEAR functional form is invalid outside the fit range, namely 5-caliber afterbody lengths. The older computation is at least bounded for longer afterbodies. Currently, the user has a choice as to which method to use for prediction purposes. For afterbodies longer than 5 calibers, the older method is used.

The NEAR code was deemed to be inaccurate for supersonic Mach numbers because of the  $M_\infty = 1.2$  estimate for the individual body components. The  $M_\infty = 1.2$  values that are used in the final interpolation are currently determined from functional form fits to computations generated by an improved Van Dyke hybrid potential model (Reference 53). The new functional form fits were generated from a much larger data base than the original form fits. The total computational cost was about one hour of CDC 6700 execution time. The  $C_{N\alpha}$  and  $x_{cp}$  predictions at  $M_\infty = 1.2$  compare well with those of the original potential computation.

### SUMMARY OF NEW ANALYSES METHODS

The body-alone analysis methods are summarized in Figure 21. The Mach region division points are normally at  $M_\infty = 0.8$ , 1.2, and somewhere in the region  $2 \leq M_\infty \leq 3$  as determined by the user.

New methods for computing the wing-alone and interference aerodynamics are listed in Figure 22.

Finally, the new methods used to compute the dynamic derivatives are summarized in Figure 23. The input option refers to use of LMSC or other prediction methods of  $C_{mq} + C_{m\dot{\alpha}}$  for body-alone or body-tail configurations.

At high angles of attack, the body-alone or body-tail computations are based on the empiricism of Reference 35. Only static derivatives are determined.

### INDIVIDUAL METHODS EVALUATION

In this section the individual new analysis methods will be evaluated by comparison with other analytical methods, numerical methods, and experimented data where available. No comparison for the older methods will be considered except where applicable.

COMPONENT \ MACH NUMBER REGION	SUBSONIC	TRANSONIC	LOW SUPERSONIC	HIGH SUPERSONIC
NOSE WAVE DRAG	—	EULER PLUS EMPIRICAL	SECOND-ORDER VAN DYKE PLUS MODIFIED NEWTONIAN	SECOND-ORDER SHOCK EXPANSION PLUS MODIFIED NEWTONIAN
BOATTAIL WAVE DRAG	—	WU AND AOYOMA	SECOND-ORDER VAN DYKE	SECOND-ORDER SHOCK EXPANSION
SKIN FRICTION DRAG	VAN DRIEST II			
BASE DRAG	EMPIRICAL			
INVISCID LIFT AND PITCHING MOMENT	EMPIRICAL	EULER OR WU AND AOYOMA PLUS EMPIRICAL	TSIEN FIRST-ORDER CROSSFLOW	SECOND-ORDER SHOCK EXPANSION
VISCOUS LIFT AND PITCHING MOMENT	ALLEN AND PERKINS CROSSFLOW			

Figure 21. New Methods for Computing Static Body-Alone Aerodynamics

COMPONENT \ MACH NUMBER REGION	SUBSONIC	TRANSONIC	LOW SUPERSONIC	HIGH SUPERSONIC
INVISCID LIFT AND PITCHING MOMENT	LIFTING SURFACE THEORY	EMPIRICAL	LINEAR THEORY	SHOCK EXPANSION STRIP THEORY
WING BODY INTERFERENCE	SLENDER BODY THEORY AND EMPIRICAL		LINEAR THEORY, SLENDER BODY THEORY AND EMPIRICAL	—
WING TAIL INTERFERENCE	LINE VORTEX THEORY			—
WAVE DRAG		EMPIRICAL	LINEAR THEORY + MODIFIED NEWTONIAN	SHOCK EXPANSION + MODIFIED NEWTONIAN STRIP THEORY
SKIN FRICTION DRAG	VAN DRIEST			
TRAILING EDGE SEPARATION DRAG	EMPIRICAL			
BODY BASE PRESSURE DRAG CAUSED BY TAIL FINS	EMPIRICAL			

Figure 22. New Methods for Computing Wing-Alone and Interference Aerodynamics

COMPONENT	MACH NUMBER REGION	SUBSONIC	TRANSONIC	LOW SUPERSONIC	HIGH SUPERSONIC
BODY-ALONE PITCH DAMPING MOMENT		EMPIRICAL			
		(OR) MODIFIED SLENDER- BODY THEORY	(OR) LINEAR INTERPOLATION	(OR) EMBEDDED NEWTONIAN THEORY	
WING AND INTERFERENCE ROLL DAMPING		LIFTING SURFACE THEORY	EMPIRICAL	LINEAR THIN-WING THEORY	STRIP THEORY
BODY-ALONE MAGNUS MOMENT		EMPIRICAL			
WING AND INTERFERENCE MAGNUS MOMENT		ASSUMED ZERO			
BODY-ALONE ROLL DAMPING MOMENT		EMPIRICAL			
WING AND INTERFERENCE PITCH DAMPING MOMENT		SLENDER-WING THEORY	(OR) SUPERSONIC SLENDER-WING THEORY	(OR) EMBEDDED NEWTONIAN STRIP THEORY	
		(OR) LIFTING SURFACE THEORY	(OR) EMPIRICAL	(OR) LINEAR THIN- WING THEORY	STRIP THEORY

\* INPUT OPTION, MACH DIVISION POINTS ARE AT  $M_\infty = 1$  AND  $M_\infty = \bar{M}^*$ .

$\bar{M}^*$  IS VARIABLE, BUT  $\bar{M}^* \geq 1.5$ .

\*\* INPUT OPTION, MACH DIVISIONS AT  $M_\infty = 1$  AND A MACH NUMBER DEPENDENT ON ASPECT RATIO,  $M_\infty = \sqrt{1 + (A_w/4)^{-2}}$ .

Figure 23. New Methods for Computing Dynamic Derivatives



## HIGH MACH NUMBER STATIC AERODYNAMICS

One consideration is the determination of the Mach number  $M = M_q$ , below which potential theory will be used and above which the second-order shock-expansion and strip theories will be used.

### Body-Alone Inviscid Aerodynamics

The High Mach body-alone routine was evaluated and compared with the potential codes from References 1 and 53 and with experimental data. Space limitations permit only a small portion of this evaluation to be presented here. Originally it was hoped that the High Mach body-alone code could be extended down to  $M_\infty \approx 1.2$ , i.e., to be used throughout the supersonic flow regime. This did not prove to be feasible.

Although purely inviscid data (integrated pressure data) are not readily available, data for two configurations, a blunt-nosed, flared body and a  $11.5^\circ$  blunted conical nose, for which integrated pressure data are available were taken from Reference 28. Comparisons made between these data, the results from the High Mach code, and the two potential codes of References 1 and 53 are given in Figures 24 and 25. As can be seen, the High Mach code does a creditable job for all functions for these particular configurations and Mach number range shown. In general, the drag,  $C_A$ , prediction was found to show better agreement than that achieved for the  $C_{N\alpha}$  and  $x_{cp}$  predictions.

From Reference 44, the forebody drag,  $C_{AF}$ , was available for blunted tangent ogive-cylinder bodies with afterbody lengths of 6 cylinders. Comparisons of  $C_{AF}$  for four noses are given in Figure 26. Note that the High Mach prediction accuracy for  $C_{AF}$  is quite poor, below  $M_\infty \approx 1.5$  and improves with Mach number. For the low supersonic Mach range, the method of Reference 1 is best for blunted tangent-ogive noses. The normal force derivative,  $C_{N\alpha}$ , comparisons for the same four bodies are presented in Figure 27, while  $x_{cp}$  downstream from the nose-afterbody junction is given in Figure 28. These comparisons indicate that the  $C_{N\alpha}$  prediction using the High Mach methodology degrades sharply with bluntness; none of the methods appear to compare well with the data in predicting  $x_{cp}$ . Also, the trend for  $x_{cp}$  as predicted by the High Mach code is incorrect for the blunter configurations. The poorest prediction is for highly curved bodies and bodies with negative slopes.

One clear conclusion is that the High Mach body-alone prediction should not be used below  $M_\infty = 2$ . However, no other rapid computational choice currently is available for predicting  $C_{N\alpha}$  and  $x_{cp}$  at high Mach numbers. In the code the dividing point between high Mach number and low supersonic Mach number is an input choice where a range of  $2 \leq M_q \leq 3$  is recommended.

### Wing-Alone Inviscid Aerodynamics

For the range of applicability, the strip method predicts almost constant  $\beta C_A$  and  $\beta C_{N\alpha}$  for a given  $t_{rw}/C_{rw}$  or thickness-to-chord ratio. To properly evaluate the method, more exact solutions or experimental data would be required. Unfortunately, neither was available. Instead, comparisons with the potential solution of Reference 2 were made for  $M_\infty \geq 2$  as shown in Figure 29 for  $\beta C_{N\alpha}$ . The comparisons are shown to improve with increasing aspect ratio and Mach number, as would be expected. Figure 30 compares  $C_{Dw}$  for a symmetrical diamond (double wedge) airfoil where  $t_{rw}/C_{rw}$  was 0.05 for all cases shown. Again, as one would expect, better agreement occurs for the larger aspect ratios. Although the  $C_{N\alpha}$  prediction is high, interference effects are not considered and hence in many cases the prediction of  $C_{N\alpha}$  at high Mach numbers is quite adequate.

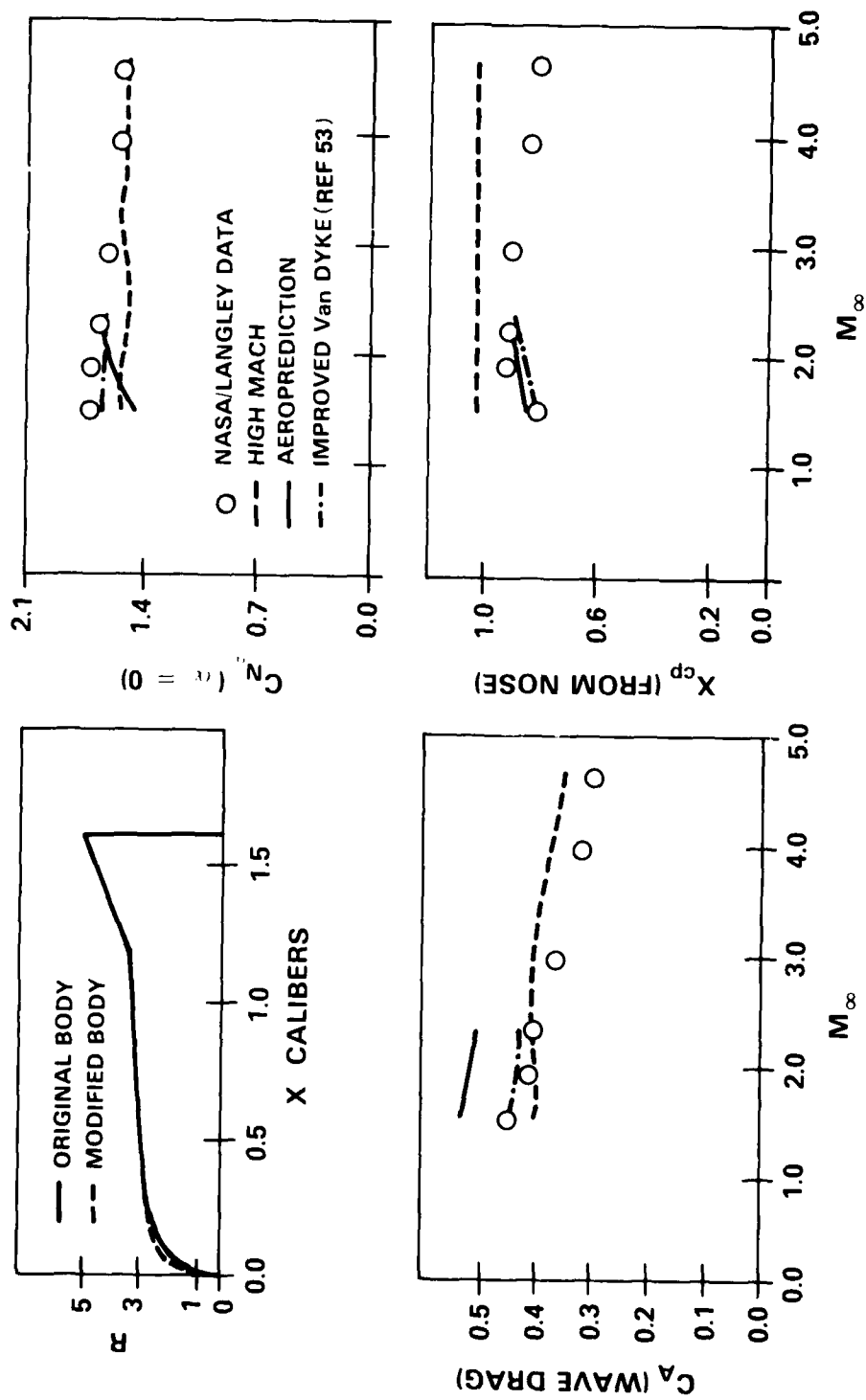


Figure 24. NASA Flared-Body Data Comparison

11.5° BLUNTED CONE NOSE,  $R_N = 0.175$

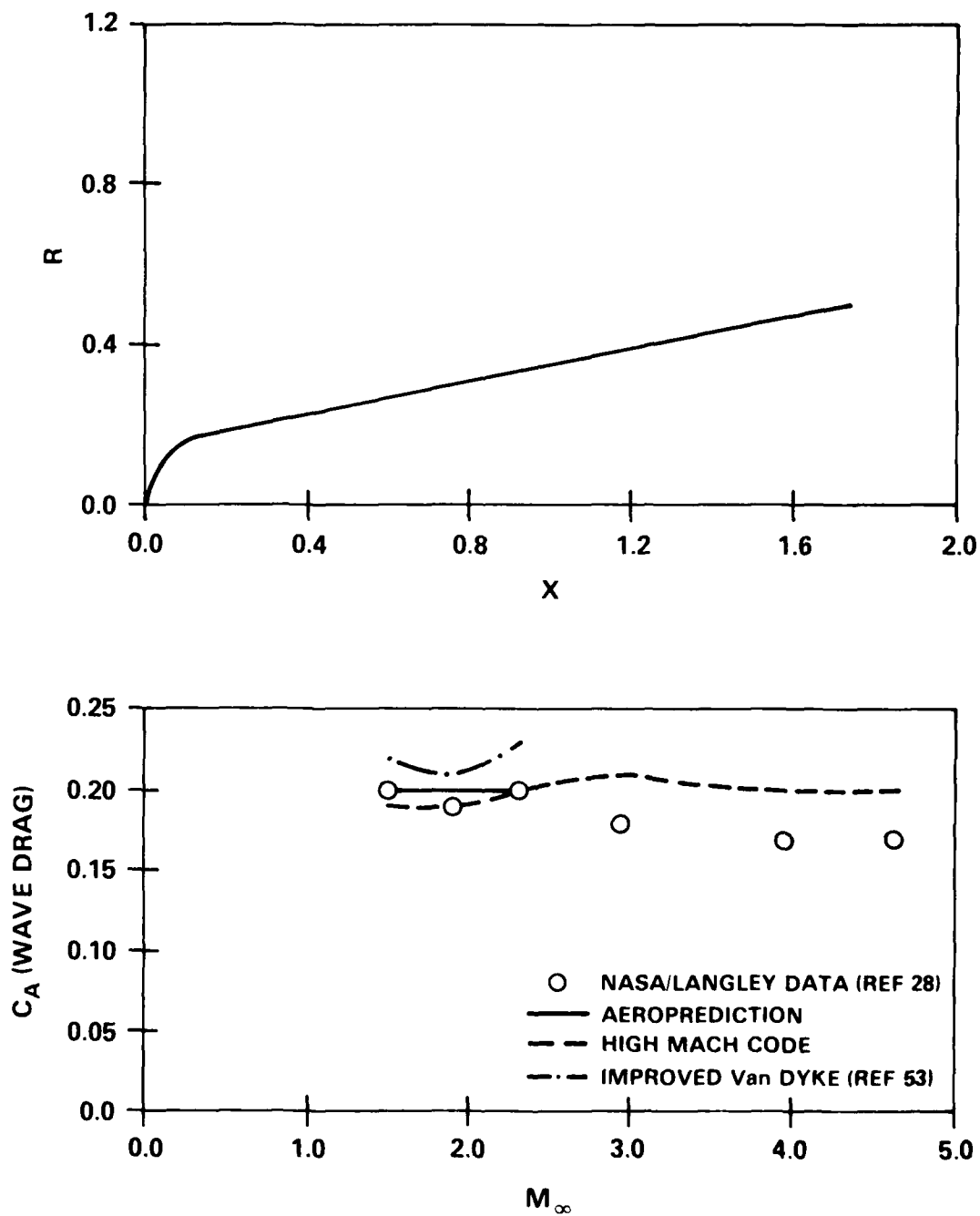


Figure 25. Blunted Cone Aerodynamics

# 11.5° BLUNTED CONE NOSE

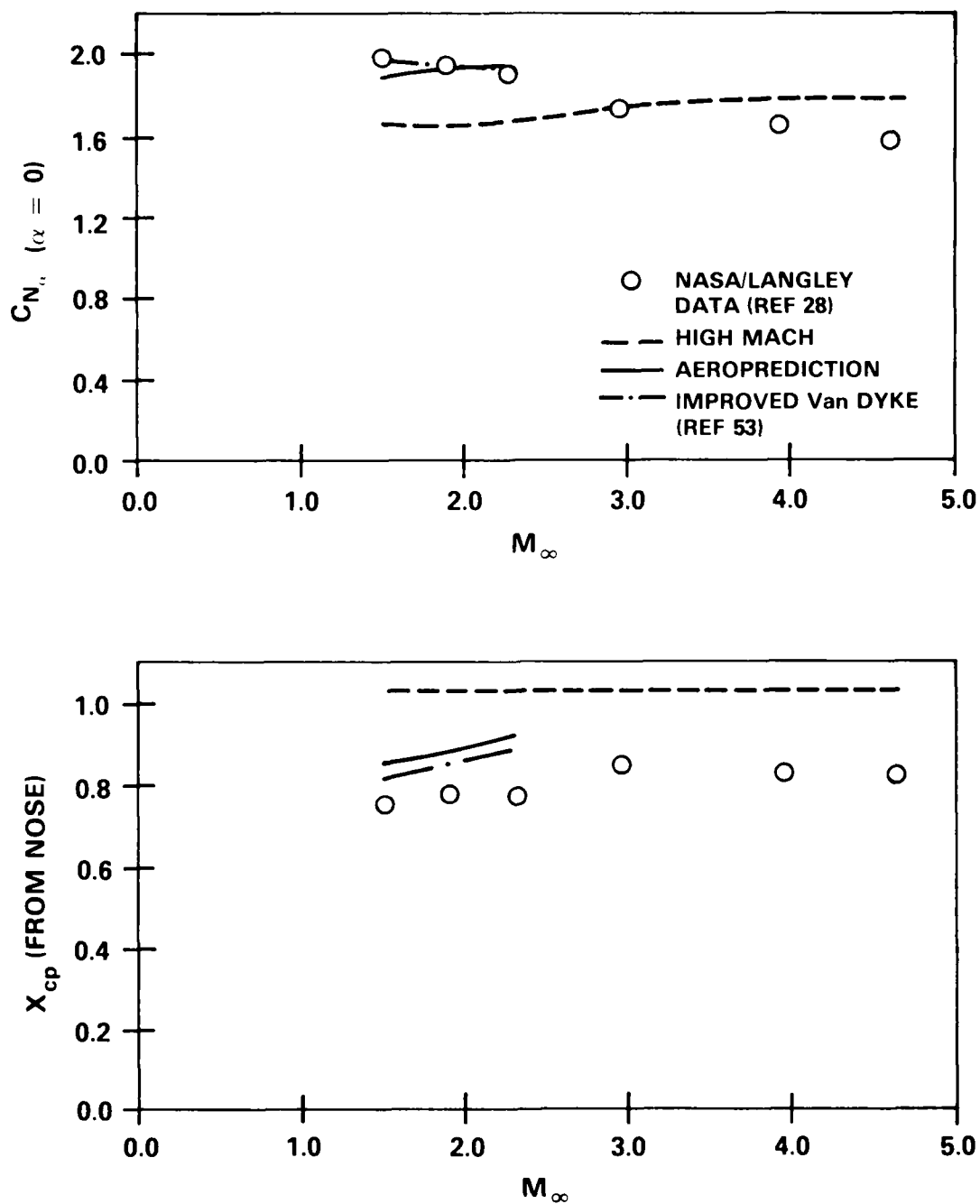
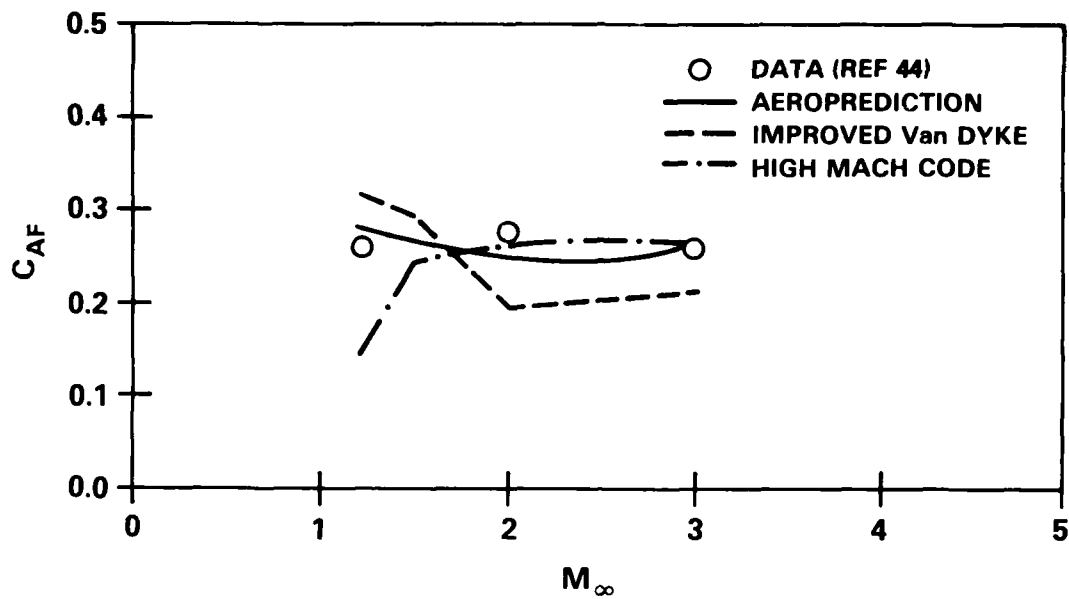
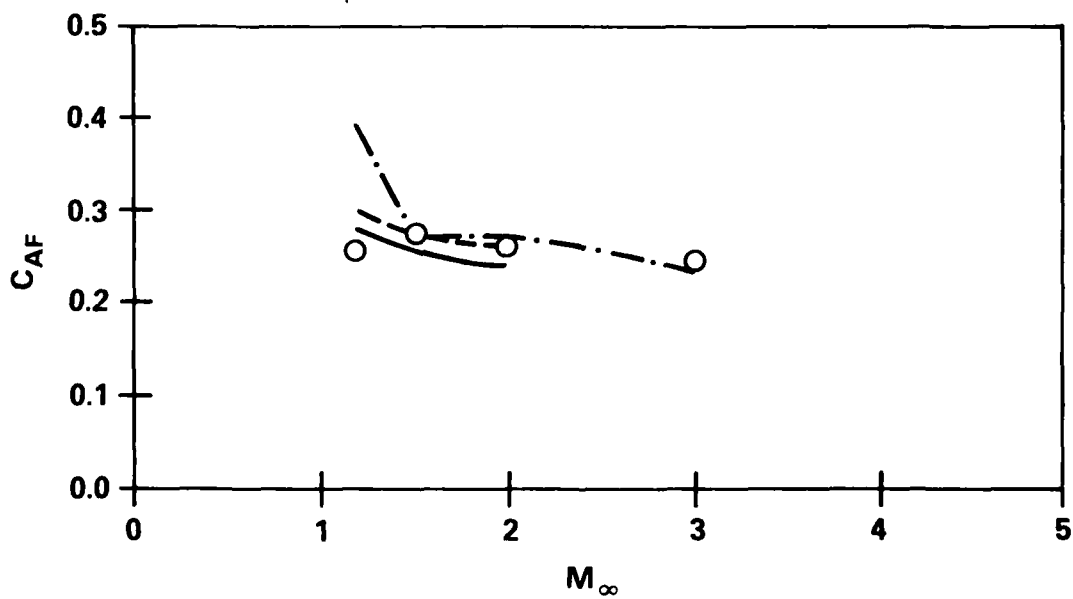


Figure 25. Blunted Cone Aerodynamics (Continued)

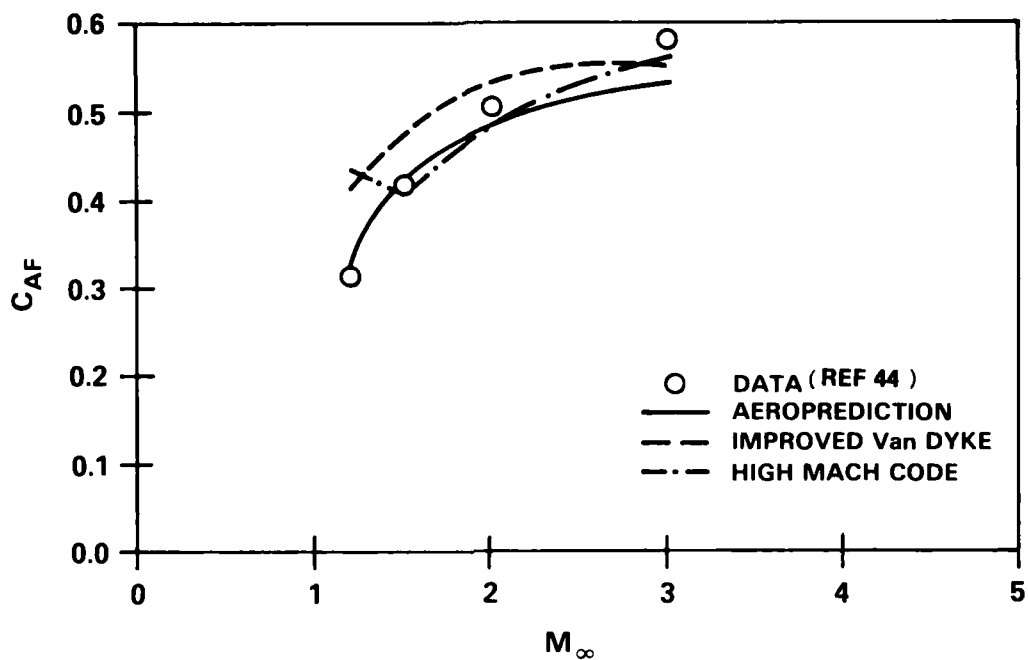


(a)  $L_N = 1.843$ ,  $R_N = 0.125$ ,  $\alpha = 0$

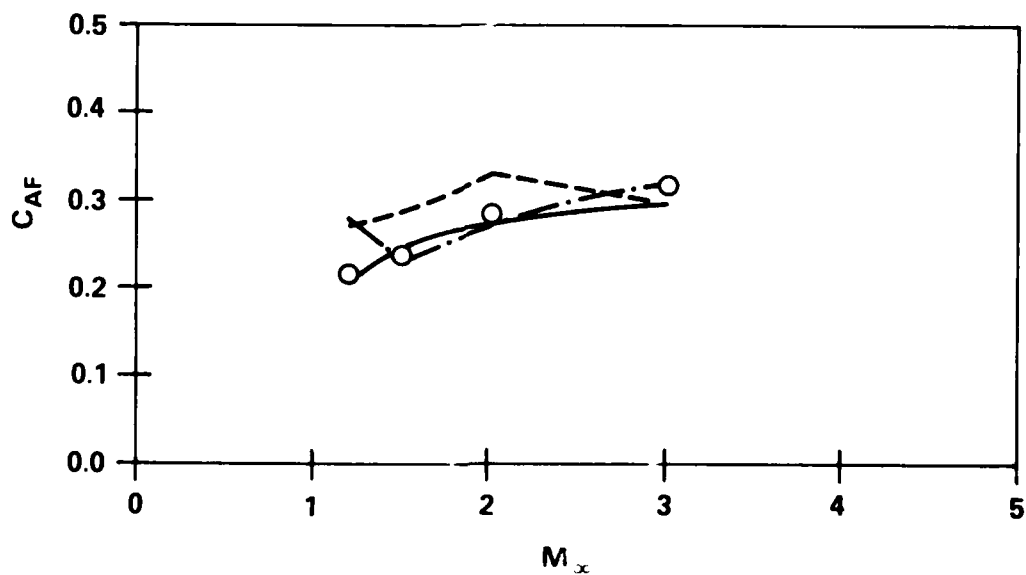


(b)  $L_N = 2$ ,  $R_N = 0$ ,  $\alpha = 0$

Figure 26. Blunted Tangent Ogive-Forebody Axial Force

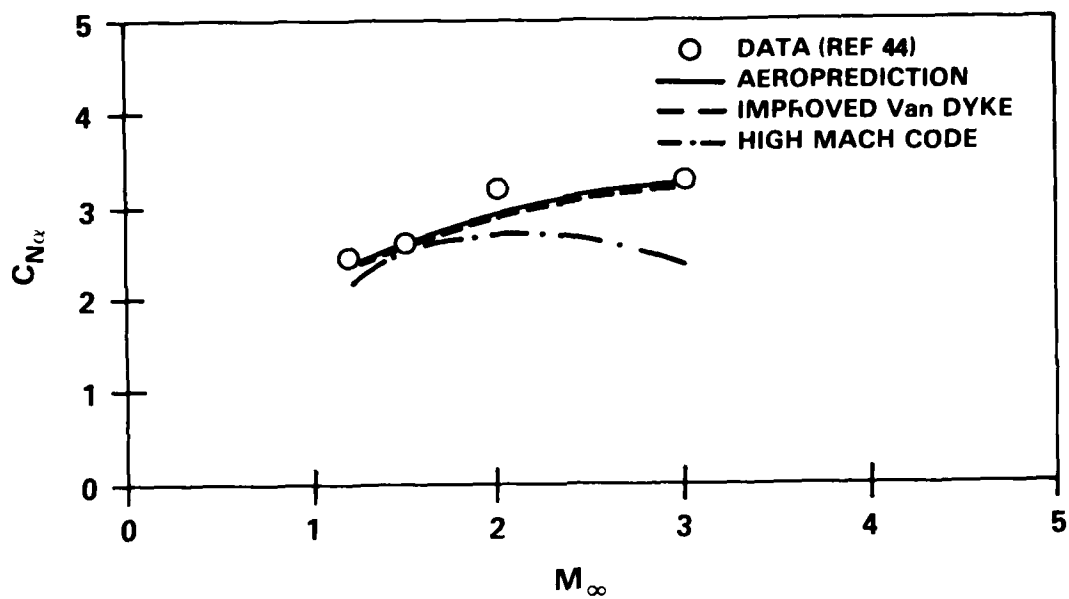


(c)  $L_N = 1.859, R_N = 0.375, \alpha = 0$

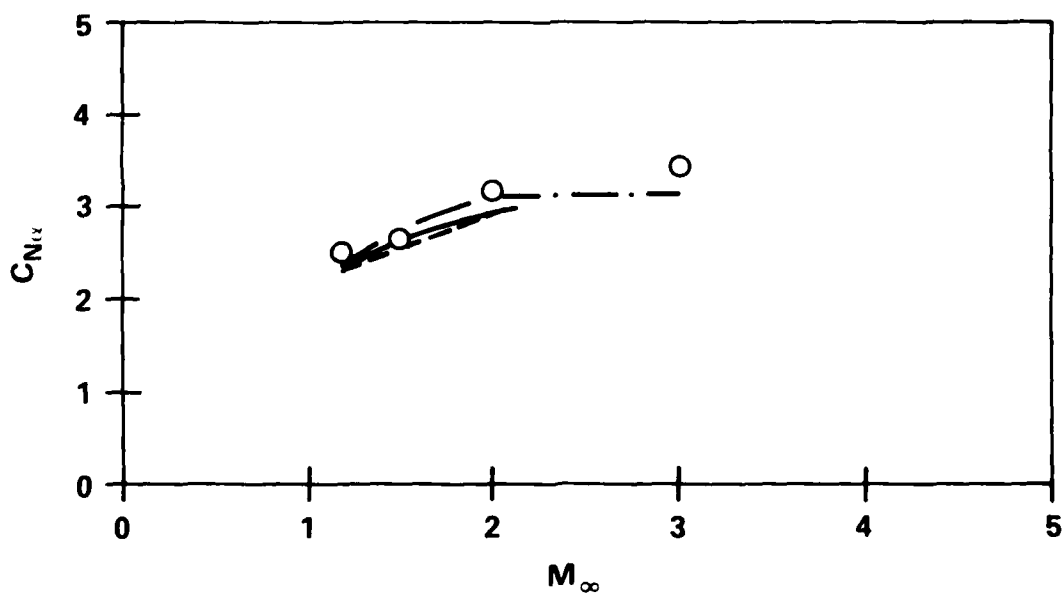


(d)  $L_N = 2.357, R_N = 0.250, \alpha = 0$

Figure 26. Blunted Tangent Ogive-Forebody Axial Force (Continued)

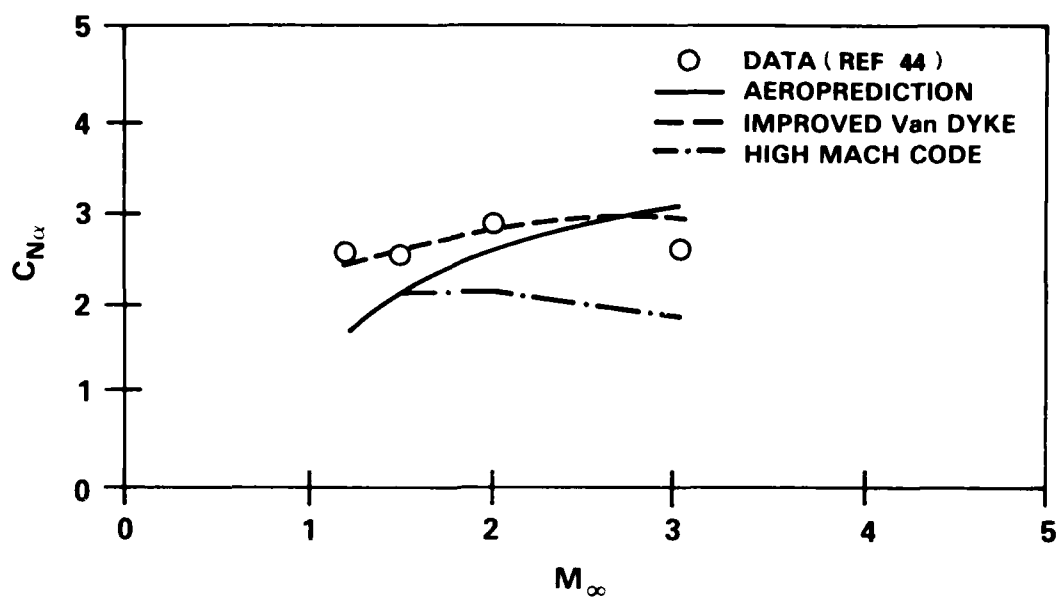


(a)  $L_N = 1.843$ ,  $R_N = 0.125$ ,  $\alpha = 0$

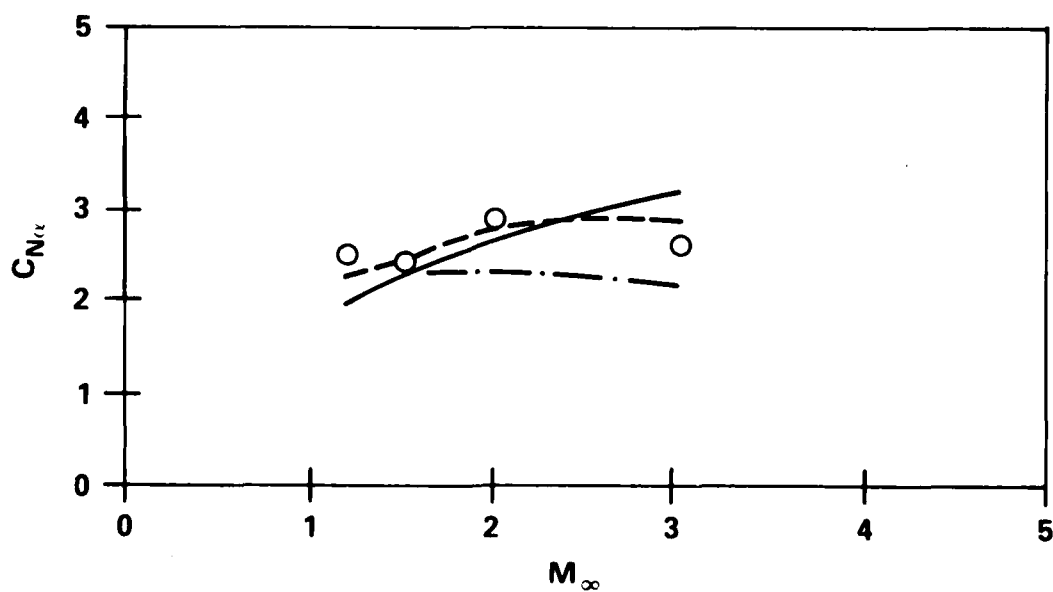


(b)  $L_N = 2$ ,  $R_N = 0$ ,  $\alpha = 0$

Figure 27. Blunted Tangent Ogive-Cylinder,  $C_{N\alpha}$



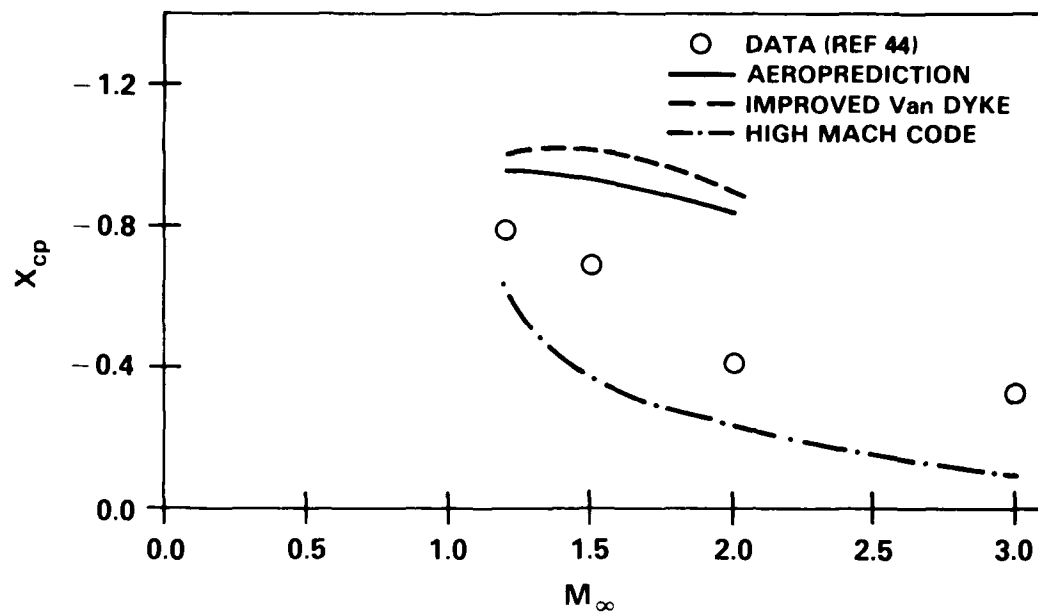
(c)  $L_N = 1.859$ ,  $R_N = 0.375$ ,  $\alpha = 0$



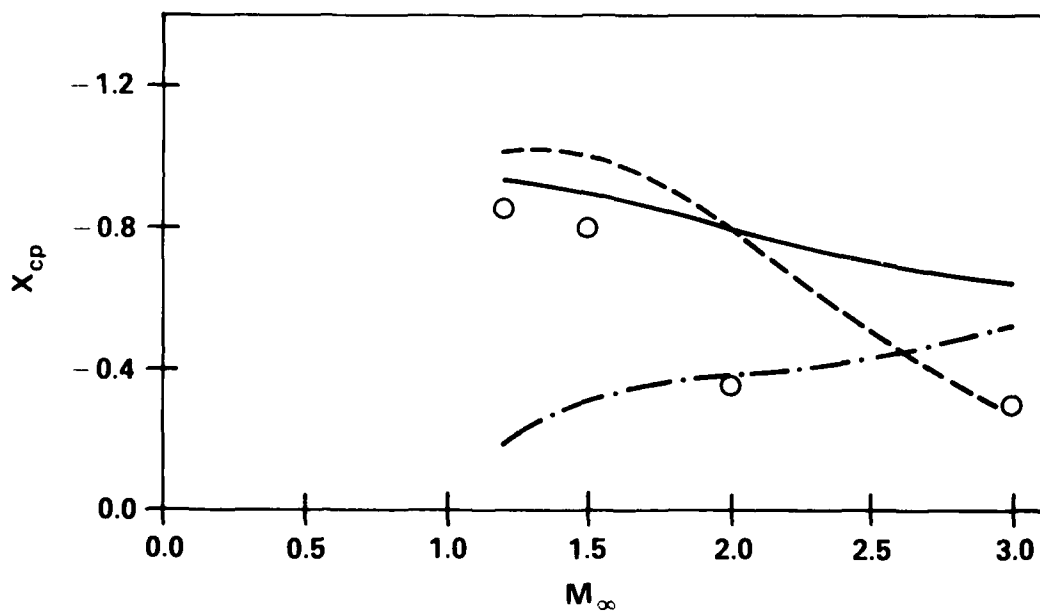
(d)  $L_N = 2.357$ ,  $R_N = 0.250$ ,  $\alpha = 0$

Figure 27. Blunted Tangent Ogive-Cylinder,  $C_{N\alpha}$  (Continued)



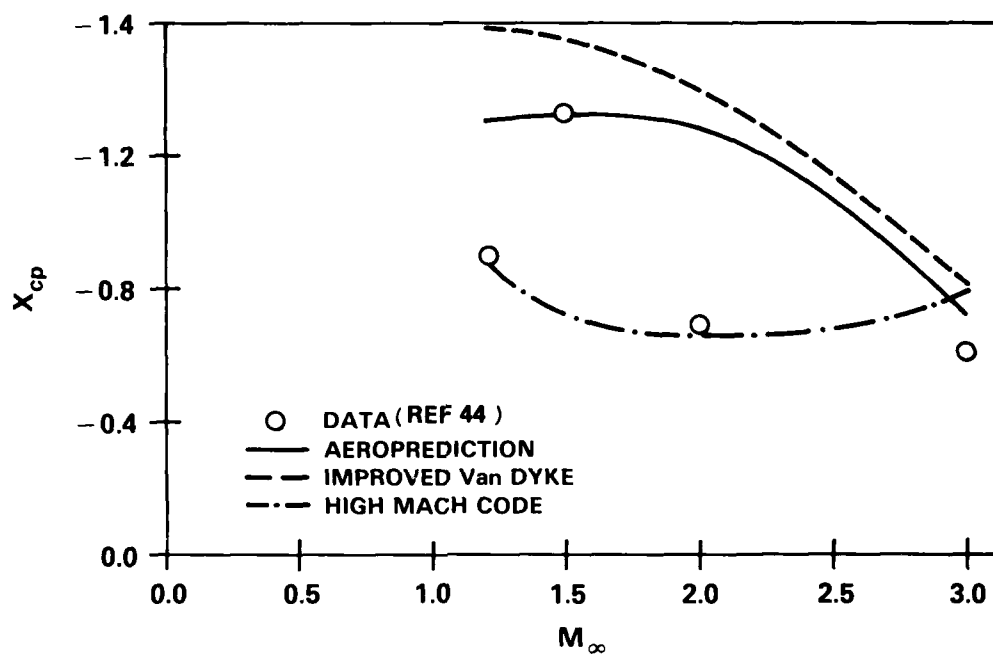


(a)  $L_N = 2$ ,  $R_N = 0$ ,  $\alpha = 0$

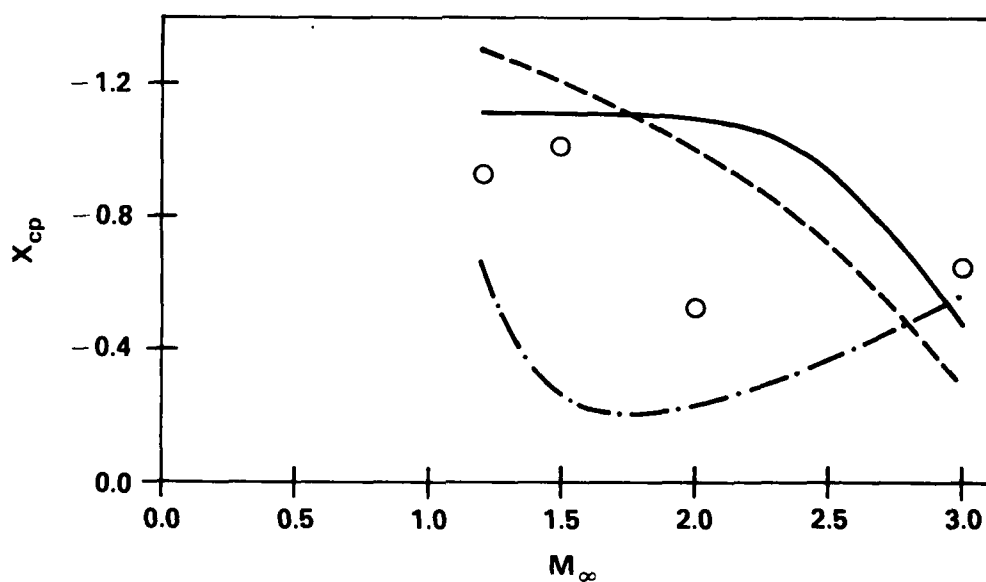


(b)  $L_N = 1.843$ ,  $R_N = 0.125$ ,  $\alpha = 0$

Figure 28. Blunted Tangent Ogive-Cylinder,  $x_{cp}$  (From Body-Nose Junction)

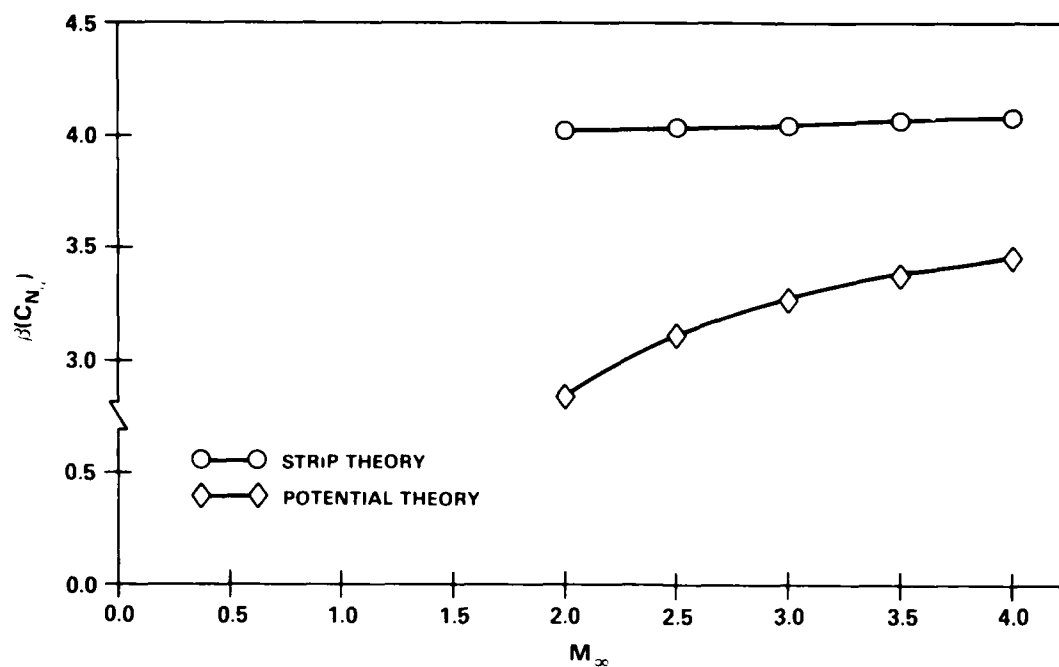


(c)  $L_N = 2.357$ ,  $R_N = 0.250$ ,  $\alpha = 0$

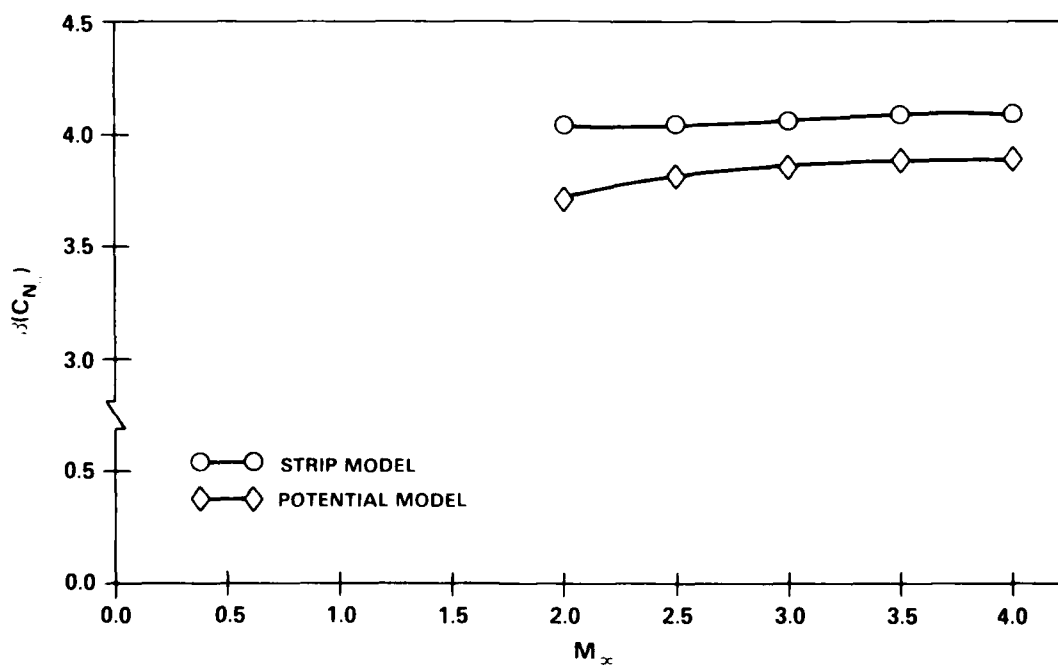


(d)  $L_N = 1.859$ ,  $R_N = 0.375$ ,  $\alpha = 0$

Figure 28. Blunted Tangent Ogive-Cylinder,  $x_{cp}$  (From Body-Nose Junction) (Continued)

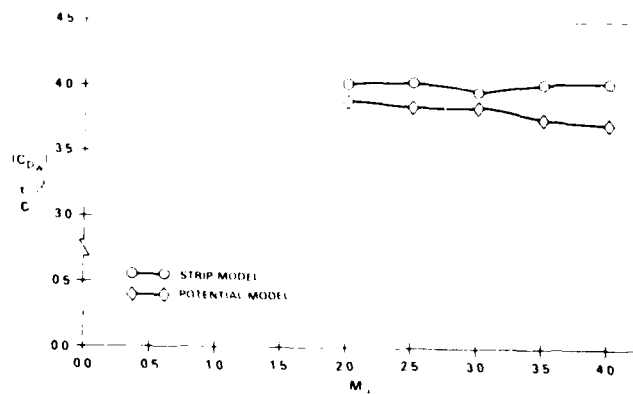


(a)  $\lambda_w = 0.99, A_w = 1, \Lambda_I = 1^\circ$

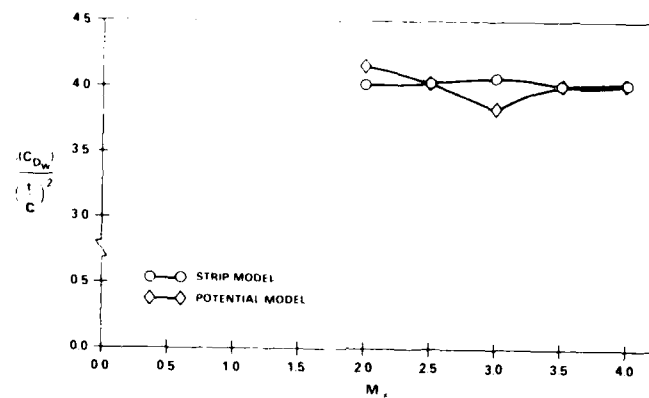


(b)  $\lambda_w = 1/3, A_w = 2, \Lambda_I = 45^\circ$

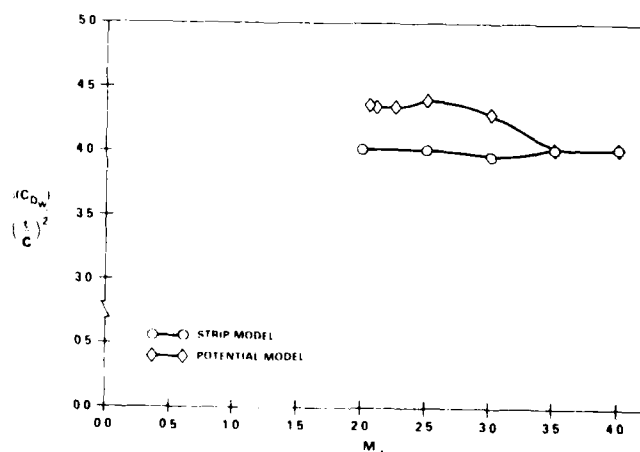
Figure 29.  $C_{N_\alpha}$  Comparison for a Wing



(a)  $\lambda_w = 0.99, A_w = 1, \Lambda_1 = 1^\circ$



(b)  $\lambda_w = 1/3, A_w = 2, \Lambda_1 = 45^\circ$



(c)  $\lambda_w = 0.40, A_w = 1, \Lambda_1 = 60^\circ$

Figure 30.  $C_{Dw}$  Comparison for a Wing

## Complete Configuration Aerodynamics

Figure 31 compares data<sup>54</sup> and the High Mach computation for a typical body-tail-canard configuration. The configuration shown in Reference 54 has body strakes not accounted for by the present combined theory, which partially accounts for the higher experimental values of  $C_{N\alpha}$ .

Data were also available at  $M_\infty = 4.65$  for the configuration shown in Figure 32. The body has a spherical cap with a 0.1-caliber radius, followed by a conical frustum 3.11 calibers long and  $5.74^\circ$  inclination, followed by a conical frustum 2.13 calibers long of inclination  $2.36^\circ$ , followed by a constant radius afterbody of 2.67 calibers, and ending with a 2-caliber,  $10^\circ$  inclined flare. The wing cross section is a rectangular slab 0.062 calibers thick with a leading edge sweep of  $70^\circ$  and a trailing edge sweep of  $0^\circ$ . The root chord and the tip chord are 2.46 calibers and 0.44 calibers, respectively. The nominal reference diameter is 0.25 ft. Reference 54 indicates that the end of the body is a skirt rather than a flare. This could account for the difference in drag values.

## HIGH ANGLE-OF-ATTACK AERODYNAMICS

The approach is purely empirical as earlier indicated. One configuration that lies in the geometric and Mach number angle-of-attack envelope is the Air Slew demonstrator configuration. Comparisons with experimental data are given in Figures 33 through 35. The normal force coefficient,  $C_N$ , is predicted adequately and  $x_{cp}$  is predicted best at higher angles of attack. However, the  $C_x$  prediction is of the right order of magnitude only.

Another comparison is made for a modified basic finner configuration (Figure 36). The comparison is slightly better for  $x_{cp}$  in this case even though this vehicle differs from the first only slightly in nose length. Note that the aerodynamics for complete configurations are predicted to  $\alpha = 45^\circ$  only. The method of Reference 56 gives predictions to  $\alpha = 180^\circ$  but no roll orientation dependent aerodynamics are computed. The current method gives only the individual component aerodynamics for angles of attack greater than  $45^\circ$ . The one exception is for the axial force coefficient prediction. The current method assumes that the body contributes the majority of the axial force or drag.

## DYNAMIC DERIVATIVE PREDICTION

The LMSC pitch damping prediction algorithm was compared very extensively with data and a purely empirical General Electric prediction program (under contract to General Electric for the evaluation). Comparisons given in Reference 57 are too numerous to be included here. The conclusion of R. Whyte of G.E.<sup>57</sup> was that the LMSC algorithm was adequate for most applications.

For body-alone cases,  $C_{mq}$  prediction was modified as earlier indicated. When the value of  $C_{mq}$  predicted is less negative than that predicted by the G.E. SPINNER program and not within 75 percent of the SPINNER value, the SPINNER value is chosen.

Comparisons for the Army-Navy Spinner test vehicle are made in Figure 37. The original LMSC prediction is shown to depart considerably from the data and the SPINNER prediction.

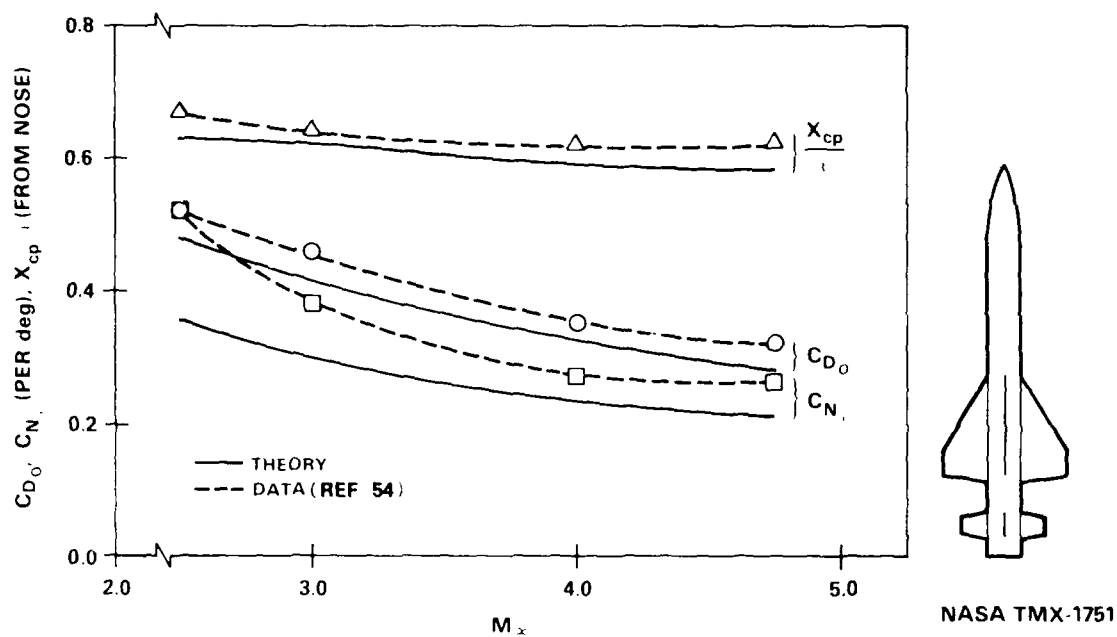
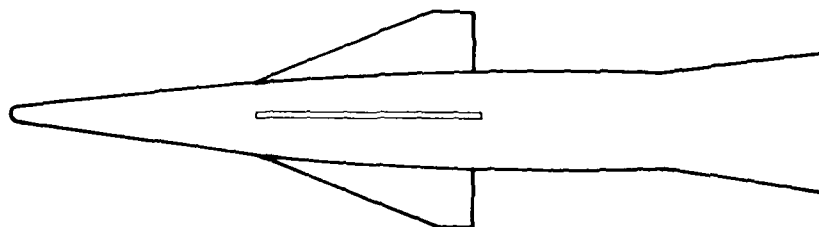


Figure 31. Comparison of Static Aerodynamics for Finned Body at High Mach Numbers ( $\alpha = 0^\circ$ )



	$C_{D0}$	$C_{N,1}$ (PER rad)	$X_{cp}/l$ (FROM NOSE)
THEORY	0.48	9.4	0.60
DATA (REF 54)	0.36	10.0	0.59

Figure 32. Aerodynamics for TMX-187  
( $M_\infty = 4.65$ ,  $\alpha = 0^\circ$ )

DIMENSIONS IN INCHES

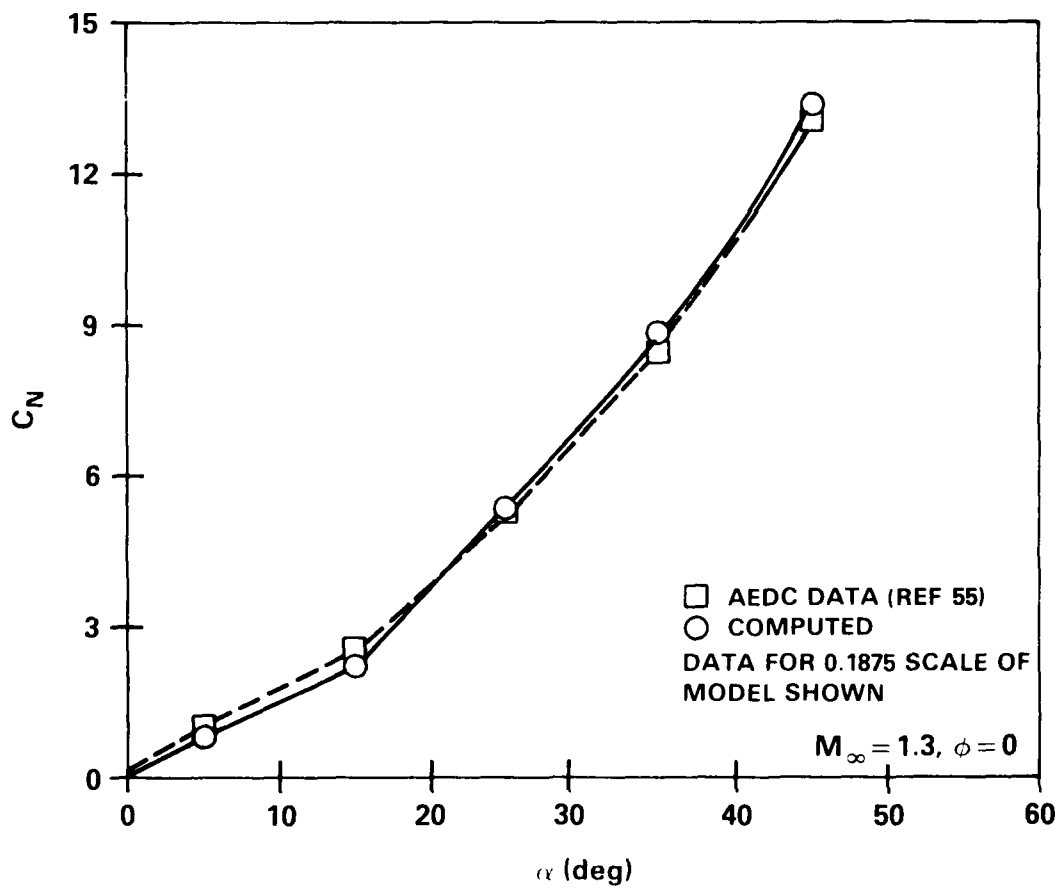
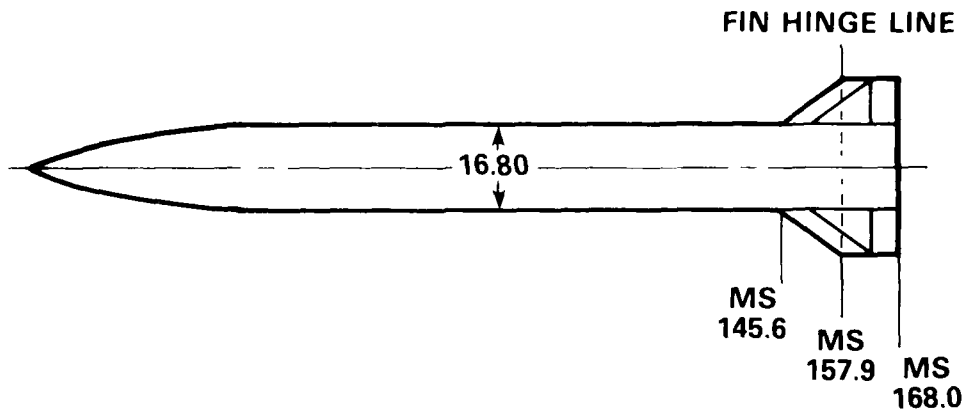


Figure 33.  $C_N$  Comparison for Air Slew Demonstrator

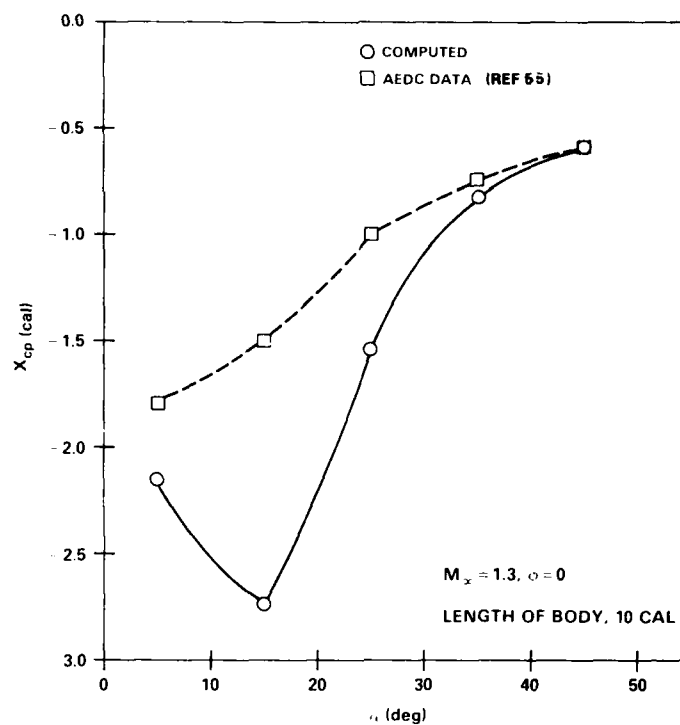


Figure 34.  $x_{cp}$  Comparison for Air Slew Demonstrator Forward of Body Midpoint

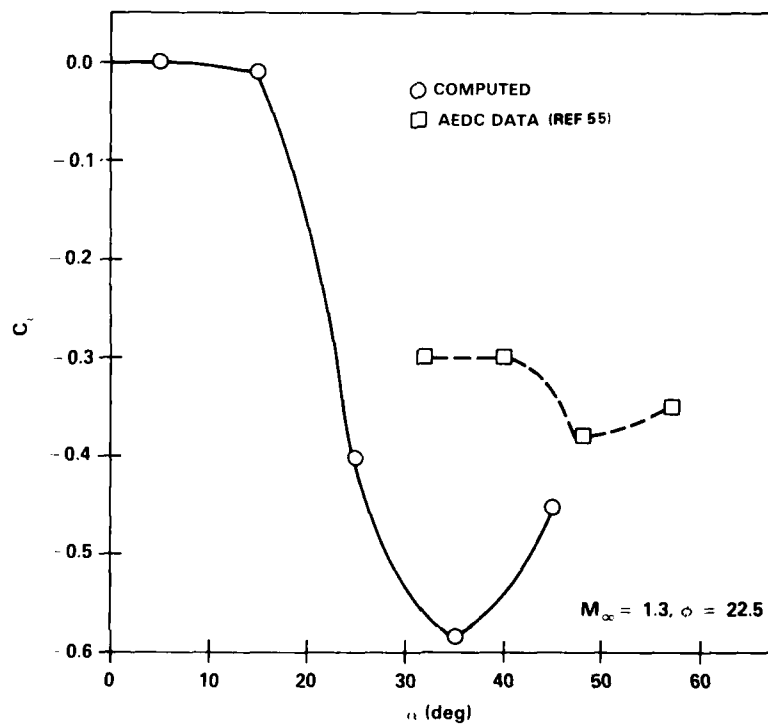


Figure 35.  $C_p$  Comparison for Air Slew Demonstrator



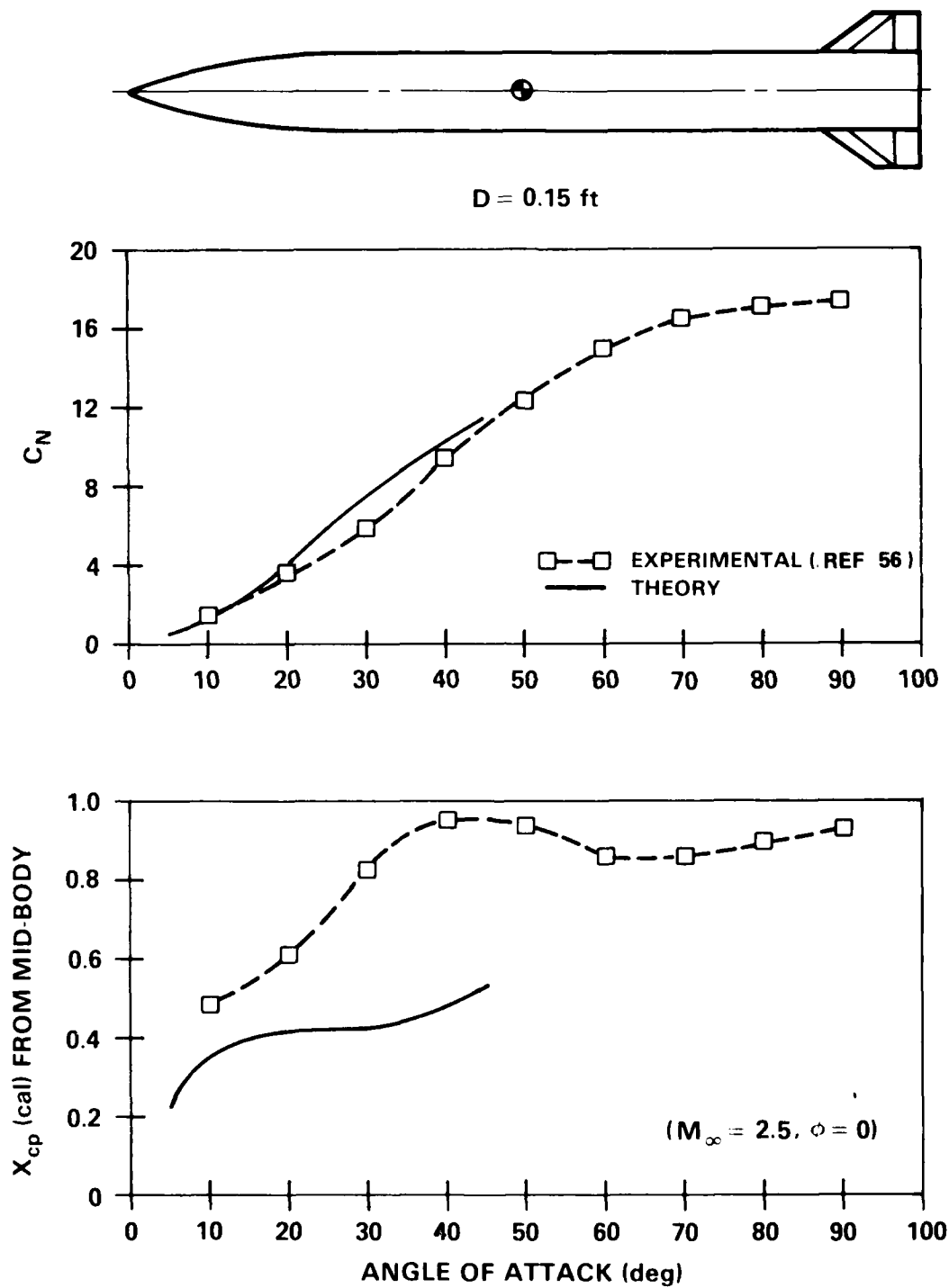


Figure 36. Modified Basic Finner Aerodynamic Comparison

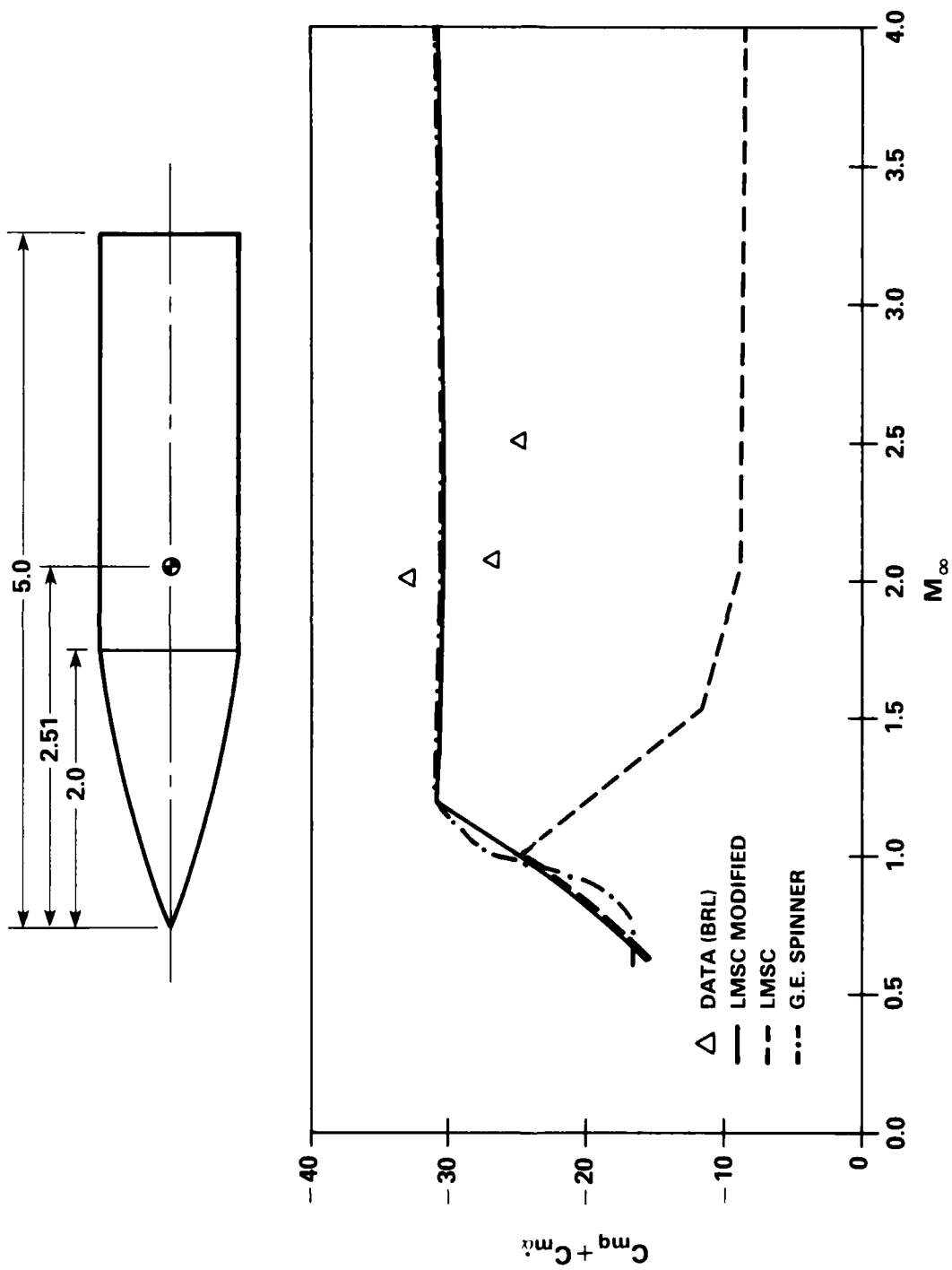


Figure 37. Army-Navy Spinner Pitch Damping Comparison

The revised LMSC prediction improves the prediction. Comparisons with data when the center of rotation is shifted downstream are better.

In Figure 38, the LMSC model is shown to predict the increased damping at  $M_\infty = 1.0$  for the basic finner and follow the data fairly well at the higher Mach numbers. The strip theory prediction for lifting surface contribution to the pitch damping is seen to be adequate. As was the case for the wing  $C_{N\alpha}$  prediction, the strip theory prediction obtained is improved for higher aspect ratios and Mach numbers. Unfortunately, data for bodies with two sets of lifting surfaces were not available.

Figure 39 shows that the strip theory estimate is adequate for  $C_{kp}$  predictions at high Mach numbers. The comparison with data and the merging with the potential model at lower supersonic Mach numbers is shown to be adequate. Again no data are available for vehicles with two sets of lifting surfaces. As was the case for the wing-alone static coefficient comparisons, the accuracy obtained with potential theory is better for higher aspect ratio and Mach number.

#### TRANSONIC NOSE WAVE DRAG

Inviscid pressure data are very scarce, particularly for the transonic case. Figure 40 shows the comparison between limited data, the old theory, and the current theory for a M-117 bomb nose. The numerical integration of pressure data was somewhat sensitive since there were not quite enough pressure tap locations. However, the theoretical prediction, which is based on a full potential solution, is much better than the original prediction based on the solution of the full Euler equations. The original Euler computation did not have enough grid resolution to accurately describe the pressure variation on the noses of blunt pointed bodies. The current prediction is seen to be an improvement over the prediction of Reference 1.

Figure 41 compares the older prediction method, the current method, and data from Reference 44. Again,  $C_{AF}$  is the forebody axial force coefficient. The values at  $M_\infty = 1.2$  labeled potential theory are determined from supersonic small disturbance theory for the pressure drag plus Van Driest's estimate of friction drag. Deviations of the supersonic small disturbance values from the curves at  $M_\infty = 1.2$  provide a measure of the discontinuity in the two methods at  $M_\infty = 1.2$ . For the blunter configurations, a definite improvement is obtained by using the new table lookup procedure. The older method neglected the effect of bluntness.

#### TRANSONIC NORMAL FORCE PREDICTION

As indicated earlier, the NEAR envelope of body parameters is limited. The afterbody length,  $L_A$ , has a maximum of 5 calibers.

Figure 42 shows a comparison between the older computation, the NEAR computation, and an improved NEAR computation with data. The set of bodies from Reference 44 with 6-caliber afterbodies is just beyond the NEAR envelope maximum of 5. In general, the  $C_{N\alpha}$  prediction for this set of data is poor for the NEAR computation and improved by the revised fits at the  $M_\infty = 1.2$  interpolation point. The NEAR  $x_{cp}$  prediction, on the other hand, is better than the older method and considerably improved by the revised curve fit at supersonic Mach numbers. As earlier indicated, the modified NEAR functionalization is an input option for  $L_A$  less than 5 calibers.

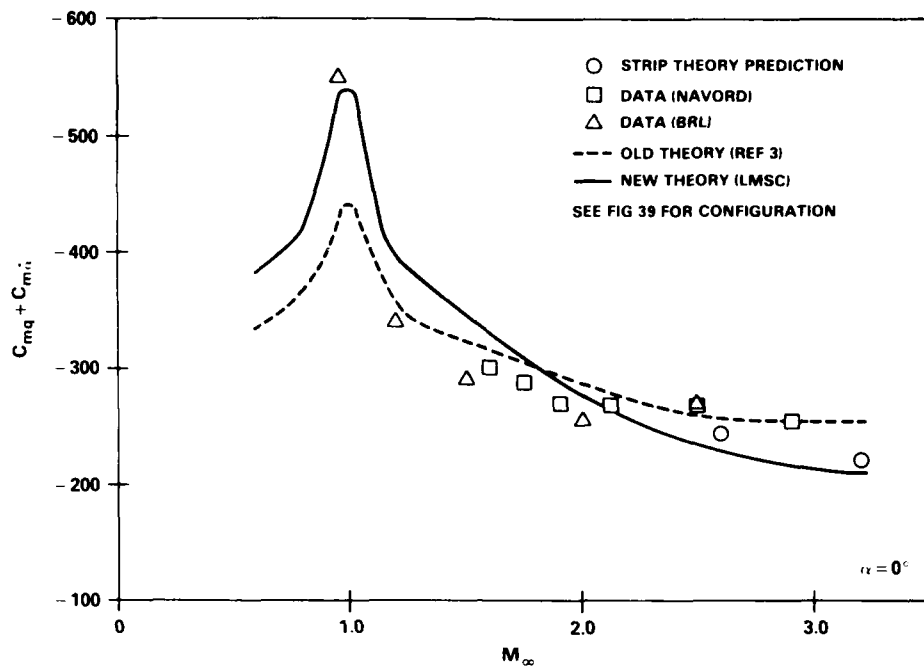


Figure 38. Basic Finner Pitch Damping Comparison

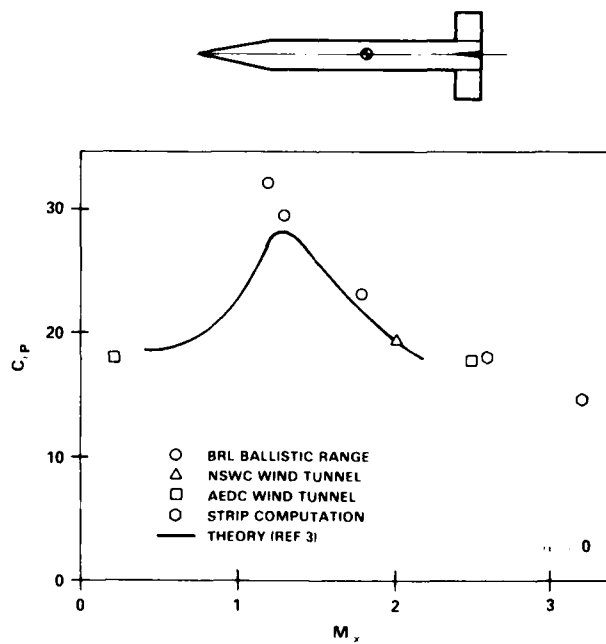


Figure 39.  $C_{l_p}$  Comparison for Army-Navy Basic Finner

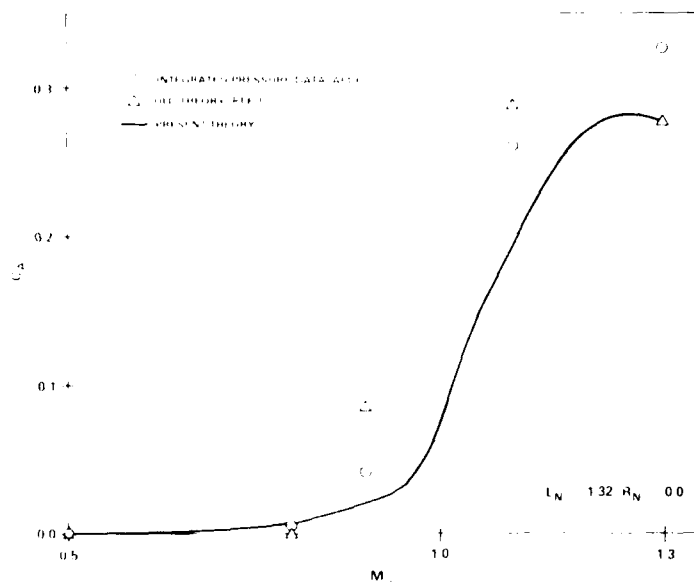


Figure 40. M-117 Bomb Nose Wave Drag Comparison

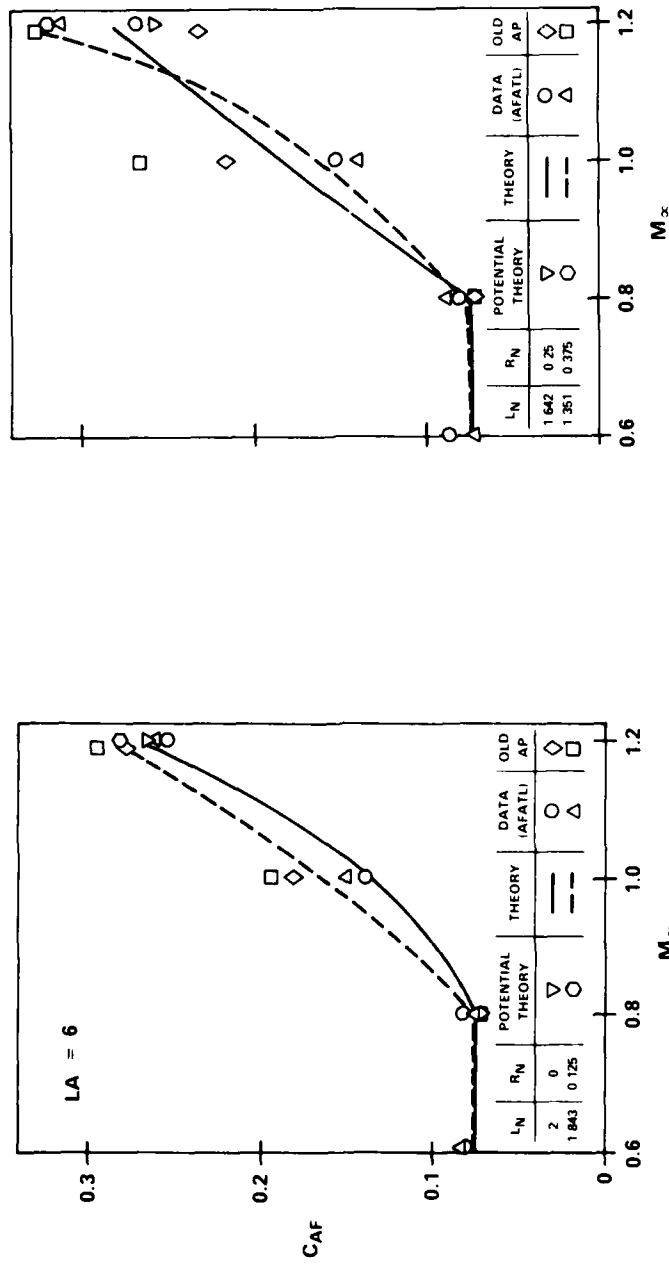
Additional comparisons for projectile shapes are given in Figures 43 through 45. All three cases have data with considerable scatter. There seems to be no sufficient justification for recommending any of the methods over the other. Currently the choice of algorithm is a program input option. For afterbodies longer than 5 calibers the older method is automatically used.

#### CONCLUDING REMARKS

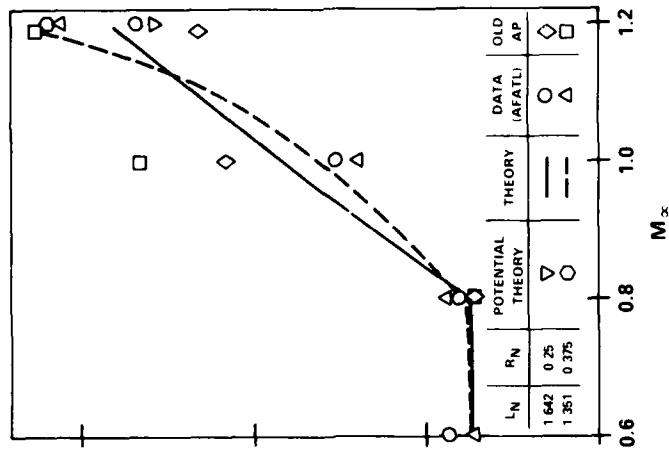
The capabilities of an earlier aerodynamic prediction methodology have been extended to higher Mach numbers and angles of attack. At small angles of attack, the inviscid static aerodynamic prediction has been extended to higher Mach numbers (approximately  $M_\infty = 6$ ) and the pitch damping coefficient is computed by a new routine for Mach numbers from 0 to approximately 6 for body-alone or body-tail configurations. Use of this routine is a program option. Also for small angles of attack, the roll damping and pitch damping contributions of lifting surfaces are estimated by a strip theory at higher Mach numbers (to approximately  $M_\infty = 6$ ). This extends the capability for the roll damping computation. The capability for prediction of the pitch damping is extended to higher Mach numbers for configurations with body-canard-tail configurations and for body-tail configurations when the new pitch damping option is not chosen.

The transonic nose wave drag routine has been replaced. Significant improvement is obtained for blunted tangent ogive and blunted cone noses. Also the transonic normal force prediction routine has been changed. Use of this routine is a program option.

An empirical high angle of attack routine has been adapted for body-tail configurations. This routine is also an input option. The prediction technique is applicable for a limited envelope and  $0.8 < M_\infty < 3$ . Body-tail static aerodynamics are predicted to  $45^\circ$  angle of attack with

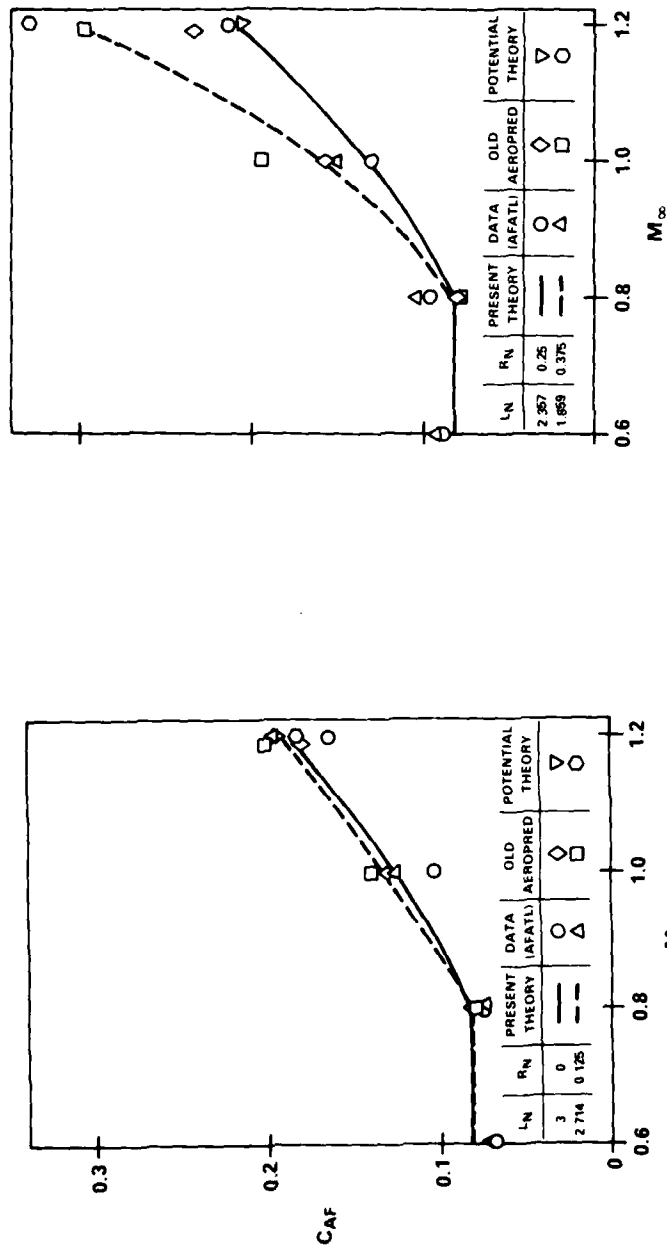


(a)

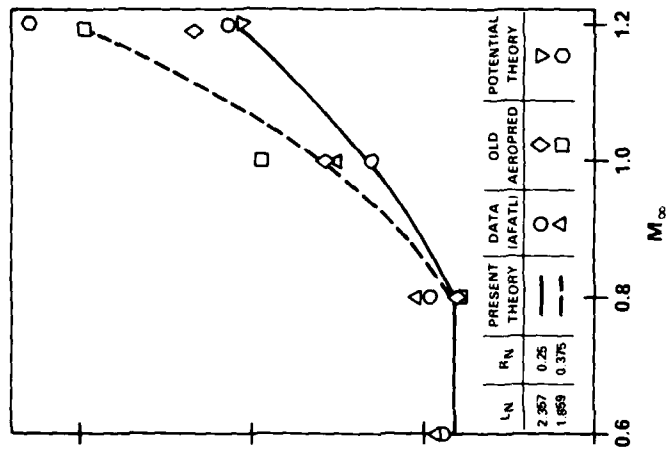


(b)

Figure 41.  $C_{AF}$  Comparison for Blunted Tangent Ogive-Cylinders



(c)



(d)

Figure 41.  $C_{AF}$  Comparison for Blunted Tangent Ogive-Cylinders (Continued)

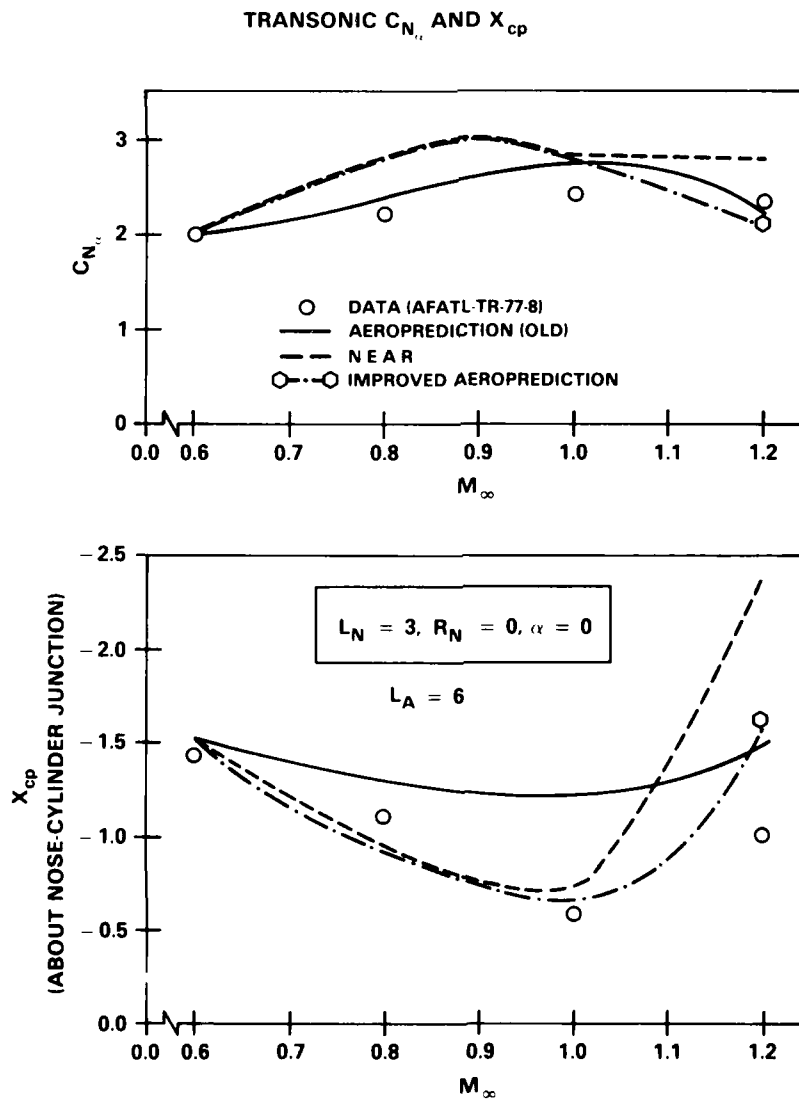


Figure 42.  $C_{N\alpha}$  and  $x_{cp}$  Comparison for Blunted Tangent Ogive-Cylinders



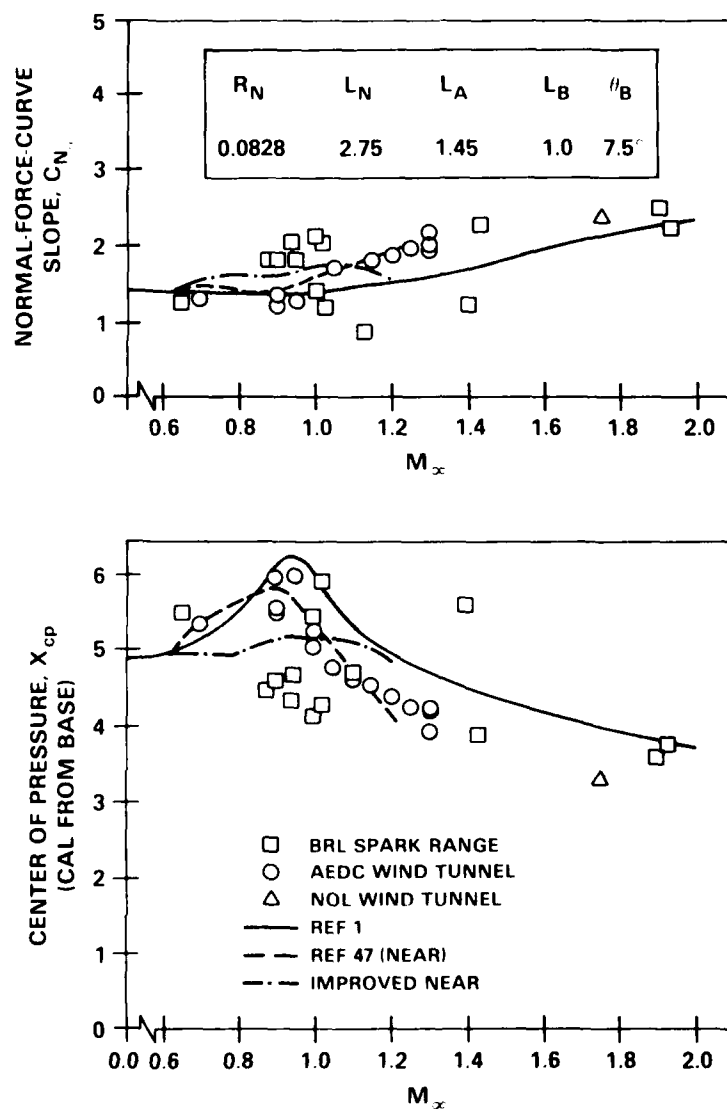


Figure 43. Comparison of Theory and Test Data for Improved 5"/54 Projectile

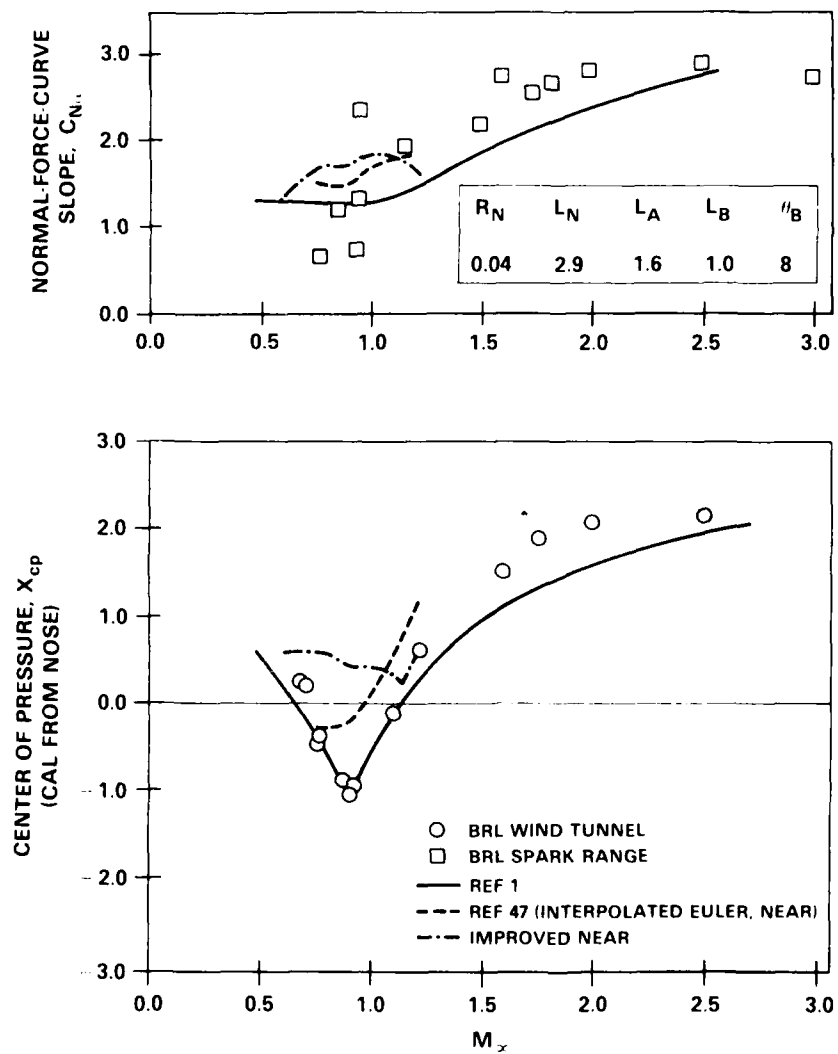


Figure 44. Comparison of Theory and Test Data for 175 mm XM437 Projectile

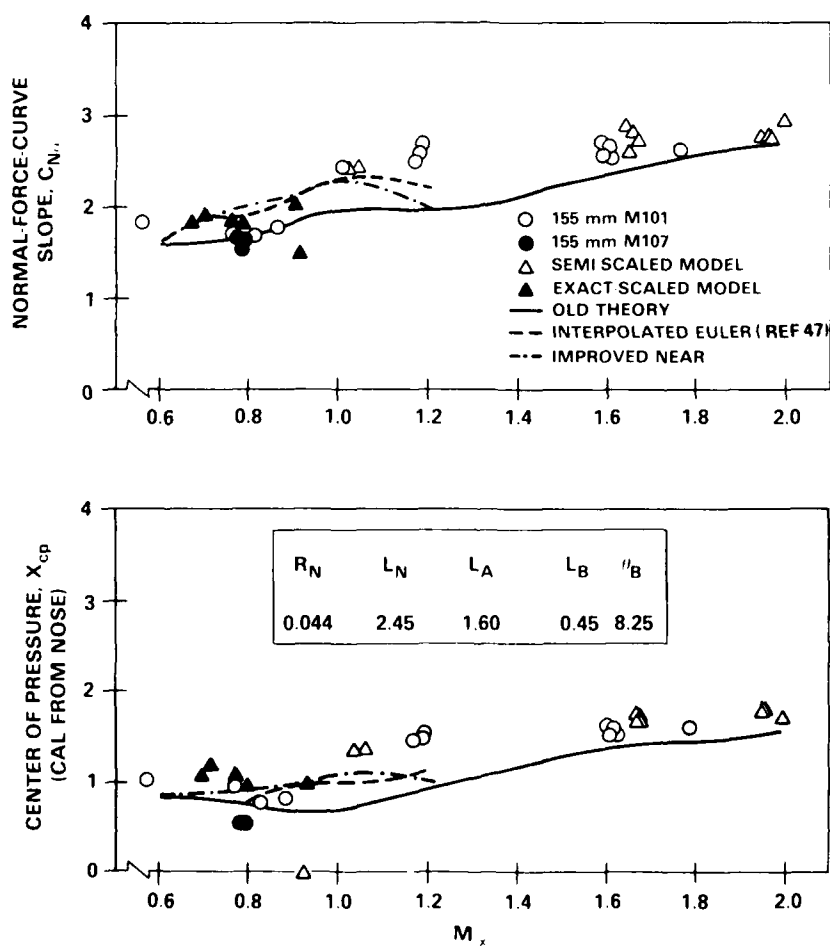


Figure 45. Comparison of Theory and Test Data for 155 mm Projectile

arbitrary roll orientation. Individual components (including the body-alone case) aerodynamics are predicted to  $180^\circ$  for the plus position roll orientation.

All of the now routines have been incorporated into the existing code. Input logic and options have been improved. A detailed description of the computer program and a listing will be given in a later publication. Computation times depend on configuration, code option, and Mach number. A computation time can range from under a second to between 30 seconds and a minute per Mach number on the CDC 6700.

## REFERENCES

1. F. G. Moore, *Body-Alone Aerodynamics of Guided and Unguided Projectiles at Subsonic, Transonic, and Supersonic Mach Numbers*, NWL TR-2796 (Dahlgren, Va., November 1972).
2. F. G. Moore, *Aerodynamics of Guided and Unguided Weapons: Part I - Theory and Application*, NWL TR-3018 (Dahlgren, Va., December 1973).
3. F. G. Moore and R. C. Swanson, Jr., *Aerodynamics of Tactical Weapons to Mach Number 3 and Angle of Attack  $15^\circ$ : Part I - Theory and Application*, NSWC/DL TR-3584 (Dahlgren, Va., February 1977).
4. M. D. Van Dyke, "First- and Second-Order Theory of Supersonic Flow Past Bodies of Revolution," JAS, Vol. 18, No. 3 (March 1951), pp. 161-179.
5. H. S. Tsien, "Supersonic Flow Over an Inclined Body of Revolution," JAS, Vol. 5, No. 12 (October 1938), pp. 480-483.
6. J. M. Wu and K. Aoyama, *Transonic Flow-Field Calculation Around Ogive Cylinders by Nonlinear-Linear Stretching Method*, U.S. Army Missile Command, Technical Report RD-TR-70-12 (Redstone Arsenal, Ala., April 1970). Also AIAA 8th Aerospace Sciences Meeting, AIAA Paper 70-189 (January 1970).
7. E. R. Van Driest, "Turbulent Boundary Layer in Compressible Fluids," JAS, Vol. 18, No. 3, pp. 145-160, 216.
8. J. H. Allen and E. W. Perkins, *Characteristics of Flow Over Inclined Bodies of Revolution*, National Advisory Committee for Aeronautics (NACA) Rm A50L07 (Moffett Field, Calif., 1965).
9. E. S. Love, *Base Pressure at Supersonic Speeds on Two-Dimensional Airfoils and on Bodies of Revolution With and Without Turbulent Boundary Layers*, NACA TN-3819 (Hampton, Va., 1957).
10. H. Ashley and M. Landahl, *Aerodynamics of Wings and Bodies*, Addison-Wesley Publishing Co. (Reading, Mass., 1965).
11. W. R. Chadwick, "The Application of Non-Planar Surface Theory to the Calculation of External Store Loads," *AIAA Journal*, Vol. 11 (March 1974), pp. 181-188.
12. R. T. Jones and C. Cohen, *High Speed Wing Theory*, Princeton Aeronautical Paperbacks, Number 6 (1960).

13. D. R. Chapman, W. R. Wimbrow, and R. H. Kester, *Experimental Investigation of Base Pressure on Blunt-Trailing-Edge Wings at Supersonic Velocities*, NACA Rep. 1109 (Moffett Field, Calif., 1952).
14. W. C. Pitts, J. N. Nielsen, and G. E. Kaattari, *Lift and Center of Pressure of Wing-Body-Tail Combinations at Subsonic, Transonic, and Supersonic Speeds*, NACA TR-1307 (Moffett Field, Calif., 1957).
15. J. C. Martin and I. Jeffreys, *Span Load Distribution Resulting From Angle of Attack, Rolling, and Pitching for Tapered Sweptback Wings With Streamwise Tips*, NACA TN-2643 (Hampton, Va., 1952).
16. F. S. Malvestuto, K. Margolis, and H. Ribner, *Theoretical Lift and Damping in Roll at Supersonic Speeds of Thin Sweptback Tapered Wings With Streamwise Tips, Subsonic Leading Edges, and Supersonic Leading Edges*, NACA TR-970 (Hampton, Va., 1952).
17. R. H. Whyte, SPIN-73, *An Updated Version of the Spinner Computer Program*, Picatinny Arsenal TR-4588 (Dover, N.J., November 1973).
18. V. E. Lockwood, *Effects of Sweep on the Damping-in-Roll Characteristics of Three Sweptback Wings Having an Aspect Ratio of 4 at Transonic Speeds*, NACA Rm L50119 (Hampton, Va., December 1950).
19. G. J. Adams and D. W. Dugan, *Theoretical Damping in Roll and Rolling Moment Due to Differential Wing Incidence for Slender Cruciform Wings and Wing-Body Combinations*, NACA TR-1088 (Moffett Field, Calif., 1952).
20. J. N. Nielsen, *Missile Aerodynamics*, McGraw-Hill Book Co., Inc. (New York, 1960).
21. I. J. Cole and K. Margolis, *Lift and Pitching Moment at Supersonic Speeds Due to Constant Vertical Acceleration for Thin Sweptback Tapered Wings With Streamwise Tips, Supersonic Leading, and Trailing Edges*, NACA TN-3196 (Hampton, Va., July 1954).
22. J. C. Martin, K. Margolis, and I. Jeffreys, *Calculation of Lift and Pitching Moments Due to Angle of Attack and Steady Pitching Velocity at Supersonic Speeds for the Sweptback Tapered Wings With Streamwise Tips and Supersonic Leading and Trailing Edges*, NACA TN-2699 (Hampton, Va., June 1952).
23. J. C. Evvard, *Use of Source Distributions for Evaluating Theoretical Aerodynamics of Thin Finite Wings at Supersonic Speeds*, NACA Report 951 (Cleveland, Ohio, 1950).
24. I. J. Cole and K. Margolis, *Lift and Pitching Moment at Supersonic Speeds Due to Constant Vertical Acceleration for Thin Sweptback Tapered Wings With Streamwise Tips, Supersonic Leading, and Trailing Edges*, NACA TN-3196 (Hampton, Va., July 1954).
25. F. S. Malvestuto and L. M. Hoover, *Lift and Pitching Derivatives of Thin Sweptback Tapered Wings With Streamwise Tips and Subsonic Leading Edges at Supersonic Speeds*, NACA TN-2294 (Hampton, Va., February 1951).
26. Douglas Aircraft Co., Inc., USAF Stability and Control DATCOM, Revisions by Wright-Patterson Air Force Base (Dayton, Ohio, July 1963), 2 Vols.

27. C. A. Syvertson and D. H. Dennis, *A Second-Order Shock-Expansion Method Applicable to Bodies of Revolution Near Zero Lift*, NACA TN-3527 (Moffett Field, Calif., January 1956).
28. C. M. Jackson, W. C. Sawyer, and R. S. Smith, *A Method for Determining Surface Pressure on Blunt Bodies of Revolution at Small Angles of Attack in Supersonic Flow*, NASA TND-4865 (Hampton, Va., 1968).
29. R. T. Stancil, "Improved Wave Drag Predictions Using Modified Linear Theory," *J. Aircraft*, Vol. 16, No. 1 (January 1979), pp. 41-46.
30. F. R. De Jarnette, C. P. Ford, and D. E. Young, "Calculation of Pressures on Bodies at Low Angles of Attack in Supersonic Flow," *Journal of Spacecraft and Rockets*, Vol. 17, No. 6, pp. 529-536.
31. M. L. Rasmusson, "On Hypersonic Flow Past an Unyawed Cone," *AIAA Journal*, Vol. 5, No. 8 (August 1967), pp. 1495-1497.
32. W. F. Hilton, *High Speed Aerodynamics*, Ch. 12, Longmans, Green and Co. (New York, 1951).
33. W. P. Helms, R. L. Carmichael, and C. R. Catellano, *An Experimental and Theoretical Investigation of a Symmetrical and a Cambered Delta Wing Configuration at Mach Numbers from 2.0 to 10.7*, National Aeronautics and Space Administration (NASA) TND-5272 (Moffett Field, Calif., March 1969).
34. A. G. Hammit and K. R. A. Murthy, "Approximate Solutions for Supersonic Flow Over Wedges and Cones," *JAS*, Vol. 27, No. 1 (January 1960), pp. 71-73.
35. G. F. Aiello, *Aerodynamic Methodology (Bodies with Tails at Arbitrary Roll Angles, Transonic and Supersonic)*, Martin-Marietta Corp. OR 14, 145 (Orlando, Fla., April 1976).
36. C. A. Smith and J. N. Nielsen, *Prediction of Aerodynamic Characteristics of Cruciform Missiles to High Angles of Attack Utilizing a Distributed Vortex Wake*, Nielsen Engineering and Research (NEAR) TR-208 (Mountain View, Calif., January 1980).
37. G. C. Winn, *User's Manual for the Martin-Marietta High Angle-of-Attack Aerodynamic Methodology for Body-Tail Missiles*, Redstone Arsenal Technical Report T-78-63 (Redstone, Ala., June 1978).
38. L. E. Ericsson, *Modification of Aerodynamic Prediction of the Longitudinal Dynamics of Tactical Weapons*, Lockheed Missile and Space Company LMSC-0646354 (Sunnyvale, Calif., June 1979).
39. Addendum to LMSC-0646354, LMSC-0646354A (Sunnyvale, Calif., August 1979).
40. L. E. Ericsson and S. R. DeLu, *User's Manual for LMSC Generalized Wing-Body Subroutine*, LMSC-0646354A (Sunnyvale, Calif., August 1979).
41. *Engineering Design Handbook Design of Aerodynamically Stabilized Free Rockets*, U.S. Army Materiel Command AMCP 706-280 (Washington, D.C., July 1968).
42. D. Chaussee, *Improved Transonic Nose Drag Estimates for the NSWC Missile Computer Program*, NSWC/DL TR-3030 (Dahlgren, Va., April 1978).

43. J. D. Keller and J. C. South, *RAYBOD: A FORTRAN Program for Inviscid Transonic Flow Over Axisymmetric Bodies*, NASA TMY-72331 (Hampton, Va., February 1976).
44. *Aerodynamic Characteristics of 2-, 3-, and 4-Caliber Tangent-Ogive Cylinders with Nose Buffness Ratios of 0.00, 0.25, 0.50, and 0.75 at Mach Numbers from 0.6 to 4.0*, AFATL-TR-77-8 (Eglin AFB, Fla., January 1977).
45. R. L. Hamner and A. D. Leff, *Linear Aerodynamic Loads on Cone-Cylinders at Mach Numbers from 0.7 to 2.0*, NASA CR-413 (Washington, D.C., March 1966).
46. R. V. Owens, *Aerodynamic Characteristics of Spherically Blunted Cones at Mach Numbers from 0.5 to 5.0*, NASA TN-D-3088 (Huntsville, Ala., December 1965).
47. G. Klopfer and D. Chaussee, *Numerical Solution of Three-Dimensional Transonic Flows Around Axisymmetric Bodies at Angle of Attack*, NEAR TR-176 (Mountain View, Calif., February 1979).
48. G. D. Kuhn and J. N. Nielsen, "Prediction of Turbulent Separated Boundary Layers," AIAA Paper 73-663, Presented at the AIAA 6th Fluid and Plasma Dynamics Conference, Palm Springs, Calif. (July 1973).
49. T. Hsieh, "Perturbation Solutions of Unsteady Transonic Flow Over Bodies of Revolution," *AIAA Journal*, Vol. 16, No. 12 (December 1978), pp. 1271-1278.
50. H. Gwin and D. J. Spring, *Stability Characteristics of a Family of Tangent Ogive-Cylinder Bodies at Mach Numbers from 0.2 to 1.5*, U.S. Army Missile Command RG-TR-61-1 (Redstone, Ala., 1961).
51. D. J. Spring, *The Effect of Nose Shape and Afterbody Length on the Normal Force and Neutral Point Location of Axisymmetric Bodies at Mach Numbers from 0.8 to 4.5*, U.S. Army Missile Command RF-TR-64-13 (Redstone Arsenal, Ala., July 1964).
52. W. D. Washington and W. Pettis, Jr., *Boattail Effects on Static Stability at Small Angles of Attack*, U.S. Army Missile Command RD-TM-68-5 (Redstone Arsenal, Ala., July 1968).
53. L. Devan, "An Improved Second-Order Theory of Inviscid Supersonic Flow Past Bodies of Revolution," Paper 80-0030, Presented at the AIAA 18th Aerospace Sciences Meeting, Pasadena, Calif. (January 1980).
54. J. O. Nichols, *Analysis and Compilation of Missile Aerodynamic Data*, NASA CR-2835 (Washington, D.C., November 1975).
55. J. M. Whoric and E. S. Washington, *Aerodynamic Characteristics of the Air Slew Demonstrator Models at Mach Number from 0.6 to  $M = 1.3$* , AEDC-TR-76-92 (Tullahoma, Tenn., August 1976).

56. W. B. Baker, Jr., *An Aerodynamic Coefficient Prediction Technique for Slender Bodies with Low Aspect Ratio Fins at Mach Numbers from 0.6 to 3.0 and Angles of Attack from 0 to 180 Degrees*, AEDC-TR-97 (Tullahoma, Tenn., March 1978).
57. R. Whyte, J. Burnett, and W. Hathaway, *Evaluation of the Computation of Pitch Damping by Subroutine LMSC*, General Electric Co., Armament Systems Dept. (Burlington, Vt., November 1979).



## LIST OF SYMBOLS

$A$	Lifting surface aspect ratio
$b$	Span of two fins (excluding body)
$C_1$	Distance along characteristic of the first family
$C_A$	Axial force coefficient
$C_{AF}$	Forebody axial force coefficient
$C_{Ap}$	Pressure axial force coefficient
$C_{D0}$	Zero angle-of-attack drag coefficient
$C_{DW}$	Wave drag
$C_\ell$	Roll moment coefficient
$C_{\ell p}$	Roll damping coefficient
$C_m$	Pitching moment coefficient
$C_{mq} + C_{m\dot{\alpha}}$	Pitch damping coefficient
$C_N$	Normal force coefficient
$C_{NB}$	Body-alone normal force coefficient
$C_{NTi}$	Isolated ith fin (in presence of the body) normal force coefficient (cruciform configuration)
$(C_N)_{TOT}$	Body-tail total normal force coefficient
$C_p$	Pressure coefficient
$C_r$	Fin root chord
$C_t$	Fin tip chord
$D$	Body reference diameter
$D_c, D_w$	Mean body diameter near a canard and tail, respectively
$I_{BT}$	Body-tail normal force coefficient interference
$K$	Hypersonic similarity parameter
$\ell$	Body length (cals.)
$L_A, L_N, L_B$	Lengths of afterbody, nose, and boattail respectively (cals.)
$M$	Mach number (local)
$M_\infty$	Freestream Mach number
$p$	Static pressure
$r$	Cylindrical coordinate (cals.)
$R$	Body cylindrical radius (cals.)

$R_N$	Body, nose spherical radius
$s$	Arc distance along body
$x$	Body coordinate (parallel to body axis)
$x_{cg}$	Distance from nose to moment reference
$x_c, x_w$	Distances to fin apex for canard and tail, respectively, fin nose
$x_{cp}$	Distance from moment reference to center of pressure
$x_{cpB}$	Body-alone $x_{cp}$ from nose
$(x_{cp})_{Ti}$	Isolated $i^{th}$ fin (cruciform configuration) $x_{cp}$ from nose
$(x_{cp})_{TOT}$	Total body-tail $x_{cp}$ from nose
$x_{cpl}$	Interference $x_{cp}$ from nose
$y$	Distance out from a wing root
$\alpha$	Angle of attack
$\beta = \sqrt{M_\infty^2 - 1}$	
$\gamma$	Calorically perfect gas heat capacity ratio
$\delta$	Local body angle
$\theta_B$	Boattail angle
$\lambda = C_t/C_r$	
$\Lambda_l = \Lambda_{le}$	Leading edge sweep of lifting surface
$\mu = \sin^{-1} \frac{1}{M}$	
$\phi$	Roll angle

### Superscripts

Differentiation with respect to  $x$

### Subscripts

$a$	Asymptotic value
$w$	Wing or tail value
$o$	Stagnation value
$1, 2$	Values upstream and downstream from a body corner respectively
$\alpha$	Partial differential with respect to $\alpha (\alpha \rightarrow 0)$

Reference area based on D. Moment reference length based on D. Dynamic derivative moment coefficients based on  $\frac{(\text{radian rate}) D}{2V_\infty}$ .

## DISTRIBUTION

Commander  
Naval Sea Systems Command  
Washington, DC 20360  
Attn: SEA-62R41, Mr. L. Pasiuk  
Technical Library

Commander  
Naval Materiel Command  
Washington, DC 20360  
Attn: Mr. S. Jacobson (MAT-032)  
Dr. John Huth  
Technical Library

Commander  
Naval Air Systems Command  
Washington, DC 20360  
Attn: AIR-320, Mr. W. Volz  
AIR-320, Dr. H. Mueller  
AIR-330D, Dr. W. H. Clark  
AIR-530, S. Loezos  
Technical Library

Commander  
Naval Weapons Center  
China Lake, CA 93555  
Attn: Mr. R. Van Aken  
Mr. R. Meeker  
Mr. Lloyd Smith  
Mr. R. E. Smith  
Mr. H. Schafer  
Technical Library

Commander  
Pacific Missile Test Center  
Point Mugu, CA 93041  
Attn: Mr. J. Rom  
Mr. G. Cooper  
Technical Library

Commander  
Naval Ship Research and Development Center  
Washington, DC 2007  
Attn: Dr. T. C. Tai  
Mr. M. J. Malia  
Technical Library

Office of Naval Research  
800 N. Quincy Street  
Arlington, VA 22217  
Attn: Mr. D. Siegel  
Dr. R. Whitehead  
Technical Library

Commanding Officer  
Naval Air Development Center  
Warminster, PA 18974  
Attn: Mr. S. Greenhalgh  
Mr. C. Reitz  
Technical Library

Superintendent  
U.S. Naval Academy  
Annapolis, MD 21402  
Attn: Head, Weapons Dept.  
Head, Science Dept.  
Dr. A. Maddox  
Technical Library

Superintendent  
U.S. Naval Postgraduate School  
Monterey, CA 95076  
Attn: Technical Library

Officer in Charge  
Naval Intelligence Support Center  
4301 Suitland Road  
Washington, DC 20390  
Attn: J. B. Chalk  
Technical Library

Commanding Officer  
Naval Ordnance Station  
Indian Head, MD 20640  
Attn: Technical Library

Director, Development Center  
Marine Corps Development and Education  
Command  
Quantico, VA 22134

NASA Langley Research Center  
Langley Station  
Hampton, VA 23365

Attn: Mr. J. South  
Mr. L. Spearman  
Mr. C. M. Jackson, Jr.  
Mr. W. C. Sawyer  
Dr. R. C. Swanson, Jr.  
Miss E. J. Landrum  
Technical Library

Virginia Polytechnic Institute and State  
University

Department of Aerospace Engineering  
Blacksburg, VA 24060

Attn: Dr. J. A. Schetz  
Dr. C. H. Lewis  
Technical Library

North Carolina State University  
Department of Mechanical and Aerospace  
Engineering

Box 5246  
Rayleigh, NC 27607

Attn: Dr. F. R. De Jarnette  
Technical Library

The University of Tennessee Space Institute  
Tullahoma, TN 37388

Attn: Dr. J. M. Wu  
Mr. C. Balasubramayan  
Technical Library

University of Notre Dame  
Department of Aerospace and Mechanical  
Engineering

Box 537  
Notre Dame, IN 46556

Attn: Dr. R. Nelson  
Technical Library

Applied Physics Laboratory  
The Johns Hopkins University  
Johns Hopkins Road  
Laurel, MD 20810

Attn: Dr. L. L. Cronvich  
Mr. E. T. Marley  
Mr. J. C. Hagan

Mr. E. Lucero  
Mr. L. Tisserand  
Mr. G. J. Pietrangeli  
Technical Library

Raytheon Company  
Missile Systems Division  
Hartwell Road  
Bedford, MS 01730

Attn: Mr. D. P. Forsmo  
Technical Library

McDonnell-Douglas Astronautics Co. (West)  
5301 Bolsa Avenue  
Huntington Beach, CA 92647

Attn: Dr. J. Xerikos  
Technical Library

McDonnell-Douglas Astronautics Co. (East)  
Box 516  
St. Louis, MO 63166

Attn: Mr. J. Williams  
Techn Mr. S. Vukelich  
Technical Library

Lockheed Missiles and Space Co., Inc.  
P.O. Box 1103  
Huntsville, AL 35807

Attn: Mr. D. Andrews  
Technical Library

Lockheed Missiles and Space Co., Inc.  
P.O. Box 504  
Sunnyvale, CA 94086

Attn: Dr. Lars E. Ericsson  
Mr. P. Reding  
Mr. H. S. Shen  
Technical Library

Nielsen Engineering and Research, Inc.  
510 Clyde Avenue  
Mountain View, CA 95043

General Electric Co.  
Armament Systems Department  
Burlington, VT 05401  
Attn: Mr. R. Whyte

CAL SPAN Advanced Technology Center  
P.O. Box 400  
Buffalo, NY 14225

Attn: Mr. B. Omilian

Northrop Services, Inc.  
Huntsville, AL 35810

Attn: Mr. W. Boyle

Science Applications Inc.  
680 E. Swedesford Rd.  
Wayne, PA 19087

Attn: Mr. P. Murad

Vought Corporation  
P.O. Box 5907  
Dallas, Texas 75222

Attn: Mr. F. Prillman  
Dr. W. B. Brooks  
Mr. R. Stancil

Hughes Aircraft Corp.  
Canoga Park, CA 91304

Attn: Dr. J. Sun  
Technical Library

Sandia Laboratories  
Albuquerque, NM 87115

Attn: Mr. R. La Farge  
Mr. R. Eisler  
Technical Library

Martin Marietta Aerospace  
P.O. Box 5837  
Orlando, FL 32805

Attn: Mr. G. F. Aiello  
Technical Library

Business and Technology Systems, Inc.  
Suite 400 Aerospace Building  
10210 Greenbelt Rd.  
Seabrook, MD 20801

Attn: Dr. J. B. Eades, Jr.

Lawrence Livermore Laboratory  
Earth Sciences Division  
University of California  
Livermore, CA 94550

Attn: Mr. D. G. Miller  
Technical Library

Honeywell Inc.  
600 Second Street  
Minneapolis, MN 55343

Attn: Mr. S. Sopczak  
Technical Library

Pacifica Technology  
P.O. Box 148  
Del Mar, CA 92014  
Attn: Dr. H. T. Ponsford

Rockwell International  
Missile Systems Division  
4300 E. Fifth Avenue  
P.O. Box 1259  
Columbus, OH 43216  
Attn: Mr. J. E. Rachner  
Technical Library

Boeing Computer Services, Inc.  
P.O. Box 24346  
Seattle, WA 98124  
Attn: Mr. R. Wyrick

Motorola Inc.  
Missile Systems Operations  
8201 East McDowell Rd.  
P.O. Box 1417  
Scottsdale, AZ 85252  
Attn: Mr. G. H. Rapp

Weapons Systems Research Laboratory  
G.P.O. Box 2151, Adelaide, S.A., 5001  
Salisbury, S.A., Australia

Attn: Mr. L. M. Sheppard  
Mr. K. D. Thomson  
Technical Library

Messerschmidt-Bölkow-Blohm GMBH  
Unternehmensbereich Apparate  
München 80-Postfach 801149  
Bayern, Federal Republic of Germany (DFR)  
Attn: Dr. H. G. Knoche  
Dr. Gregoriou

Chief of S and R Division  
Development Center  
Marine Corps Development and Education  
Command  
Quantico, VA 22134

Commanding General  
Ballistic Research Laboratory  
Aberdeen Proving Ground, MD 21005  
Attn: Dr. C. H. Murphy  
Mr. L. McAllister  
Mr. A. Platou  
Mr. R. McCoy  
Dr. R. Sedney  
Dr. W. Sturek  
Mr. C. Nietubicz  
Technical Library

Commanding General  
ARRADCOM  
Picatinny Arsenal  
Dover, NJ 07801  
Attn: Mr. A. Loeb  
Mr. H. Hudgins  
Mr. G. Friedman  
Technical Library

Commanding General  
U.S. Army Missile R and D Command  
DROMI-TDK  
Redstone Arsenal  
Huntsville, AL 35809  
Attn: Mr. R. Deep  
Dr. D. J. Spring  
Technical Library

Commanding General  
Frankford Arsenal  
Philadelphia, PA 19104  
Attn: Mr. W. Gadomski  
Technical Library

Commanding Officer  
Harry Diamond Laboratories  
Washington, DC 20013  
Attn: Technical Library

Arnold Engineering Development Center  
USAF  
Tullahoma, TN 37389  
Attn: Mr. J. Usselson  
Mr. W. B. Baker, Jr.  
Technical Library

Commanding Officer  
Air Force Armament Laboratory  
Eglin Air Force Base, FL 32542  
Attn: Dr. D. Daniel  
Mr. C. Butler  
Mr. K. Cobb  
Mr. C. Mathews  
Mr. E. Sears  
Mr. F. Stevens  
Dr. L. E. Lijewski

USAF Academy  
Colorado Springs, CO 80912  
Attn: Technical Library

Commanding Officer  
Air Force Wright Aeronautical Laboratories  
(AFSC)  
Wright-Patterson Air Force Base, OH 45433  
Attn: Dr. G. Kurylowich  
Mr. D. Shereda  
Mr. J. Jenkins  
Mr. D. Hoak  
Mr. G. Fleeman  
Mr. M. Pinney

Advance Research Projects Agency  
Department of Defense  
Washington, DC 20305  
Attn: Technical Library

NASA  
Washington, DC 20546  
Attn: Technical Library

NASA Ames Research Center  
Moffett Field, CA 94035  
Attn: Dr. G. Chapman  
Mr. V. L. Peterson  
Technical Library

Raytheon Company		G20	
Spencer Laboratory		G30	
Box SL7162		G40	
Burlington, MS 01803		K	
Attn: Mr. S. Pearlsing		K10	(2)
Mr. P. Giragosian		K20	
		K21	
		K21 (Devan)	(40)
Defense Technical Information Center		K22	(2)
Cameron Station		K23	(2)
Alexandria, VA 22314	(2)	K24	
		R	
Library of Congress		R44	(5)
Washington, DC 20390		U20	
Attn: Gift and Exchange Division	(4)	U23	
		X210	(6)
GIDEP Operations Office			
Corona, CA 91720			
Defense Printing Service			
Washington Navy Yard			
Washington, DC 20374			
Local:			
E41			
G			

FILMED

6-8